The Development of an *In-Situ* X-Ray Diffraction Cell for Fischer-Tropsch Catalyst Characterisation

by

Brett Clapham

BSc. Chemical Engineering (Honours), University of Cape Town, South Africa

Thesis presented to the University of Cape Town
in fulfilment of the requirements
for the degree of

Master of Science in Engineering

Centre for Catalysis Research
Department of Chemical Engineering
University of Cape Town
South Africa

February 2012

Synopsis

In the current study, the successful development of a novel *in-situ* X-ray diffraction cell is described. This cell allows the direct observation of crystallite changes to be made under reaction conditions and in real time. The cell permits operation up to 500°C and 25 bar to be realised, with more severe conditions being achievable upon changing the reactor component. The design is such that it can be mounted to any commercial, laboratory-scale X-ray diffractometer or synchrotron facility.

Commissioning of the cell was conducted by performing cobalt-catalysed Fischer-Tropsch synthesis (FTS), focusing on the catalyst changes during the experiments. Two catalysts were studied, synthesised by a reverse micelle technique, which resulted in model catalysts of narrow crystallite size distributions. The first had a volume-weighted Co_3O_4 crystallite size of 10.3±1.9 nm and the second, 6.1±1.4 nm (Transmission Electron Microscopy). The catalysts were supported on γ-alumina and reduced via temperature-programmed reduction in the *in-situ* XRD cell. The changes through which the catalysts went during the reduction process were monitored and identified in real time.

Upon reduction, the metallic cobalt in both catalysts was found to be essentially the face-centred cubic phase only, and the average cobalt crystallite sizes were calculated to be 18.9 nm and 4.1 nm (Rietveld refinement, XRD). FTS was performed after reduction. The synthesis gas (syngas) mixture of 60% hydrogen, 30% carbon monoxide and 10% argon was fed to the cell with its partial pressure maintained at 1 bar throughout the experiments. The *in-situ* cell facilitates the co-feeding of water at various partial pressures by a specially-designed saturator system. Water was co-fed with the syngas at partial pressures between 0-3 bar, simulating syngas conversion conditions up to 91%, as water is the predominant FTS product.

In accordance with thermodynamics, the cobalt in the catalyst with the larger cobalt crystallites (18.9 nm) remained metallic throughout the FTS experiments at all studied water partial pressures. The cobalt in the catalyst with the smaller crystallites (4.1 nm) was found to be partially oxidised at a water partial pressure of 0.5 bar (63% simulated conversion) and to be completely oxidised to CoO at a water partial pressure of 1 bar (77% simulated conversion), in accordance with thermodynamics. These observations mark the first time that oxidation has been observed directly and in real time.

Activity and selectivity analyses were performed using online and offline Gas Chromatography. Higher water partial pressures were found to have a positive effect with both catalysts (until oxidation occurred with the smaller crystallites), with catalytic activity and chain-growth probability increasing. Methane selectivity decreased and C_{5+} selectivity increased. The olefin fraction for product fractions with carbon numbers 2-7 increased, and secondary olefin formation by isomerisation decreased.

Branching was also found to decrease with increasing water partial pressure, considered to be a co-result of suppressed isomerisation of primary olefins.

Acknowledgements

Firstly, thanks to Prof. Michael Claeys for his outstanding supervision. His guidance, experience, training and motivation are greatly appreciated and will be valuable in any future endeavour. His professionalism and availability are highly valued. He is truly a world-class researcher and engineer. The discussions with him also extended into the areas of cycling, mountain biking and triathlon. Thanks to Dr Nico Fischer for his design work and instruction and help in catalyst preparation and experimental methods. He was highly instrumental in the early stages and his input into this project is also greatly appreciated. Thanks to Dr Theresa Feltes who provided invaluable help in the experiments, X-ray diffraction and gas chromatography systems. Her work in this project was essential and also greatly appreciated.

Thanks to Marc Wüst for his design work on the cell and in practical help. Jo Macke's work in manufacturing various parts for the cell and the discussions with him are also appreciated. Christiaan de Vries provided useful help and advice and was always willing to discuss the work. Dr Esna du Plessis provided help and guidance with Rietveld refinement.

Dirk Reyskens and Waldo Koorts helped with various details in the laboratory and experimental work. Helen Divey and Suzanna Vasic provided help with AAS measurements. Debbie de Jager is acknowledged for help with ordering equipment and her persistence with international orders. Mohammed Jaffer and Franscious Cummings helped with Transmission Electron Microscopy.

Acknowledgment is also made to the Centre for Catalyst Research and the Department of Chemical Engineering at the University of Cape Town for research facilities, and to c*change (DST-NRF Centre of Excellence in Catalysis) for financial support.

Finally, and most importantly, thanks to my Lord and Saviour, Jesus Christ, who made this project possible and helped me through it. A novel *in-situ* XRD cell is a small thing for the one who made the universe.

Contents

Glossary

AAS	atomic absorption spectroscopy
Adatom	an atom that is adsorbed onto a crystal surface
Al_2O_3	alumina
Ar	argon
B	boron
BET	Brunauer Emmett Teller
CH_4	methane
CH_x	CH_2 or CH_3
Cl	chlorine
CNT	carbon nanotubes
Co	cobalt
$CoAl_2O_4$	cobalt aluminate
$Co(NO_3)_2$	cobalt nitrate
CO	carbon monoxide
CO_2	carbon dioxide
Co_3O_4	cobalt oxide
Cu	copper
CTL	coal-to-liquids
EDX	energy-dispersive X-ray [spectroscopy]
EXAFS	extended X-ray absorption fine structure
FID-MS	flame ionisation detector (with mass spectrometer)
FTIR	Fourier-transformed infrared [spectroscopy]
FTS	Fischer-Tropsch synthesis
GC	gas chromatograph / chromatography / chromatogram
GTL	gas-to-liquids
H_2O	water
HAADF	high-angle annular dark field
HCl	hydrochloric acid
$HClO_4$	perchloric acid
HF	hydrofluoric acid
HNO_3	nitric acid
HRTEM	high-resolution transmission electron microscopy
HTFT	high temperature Fischer-Tropsch
ITQ	Instituto de Tecnología Química
LTFT	low temperature Fischer-Tropsch
MFC	mass-flow controller
N_2	nitrogen

Na	sodium
NEXAFS	near-edge X-ray absorption fine structure
NTP	normal temperature and pressure, i.e. 1 atm and 293 K
O_2	oxygen
PONKCS	partially or no known crystal structures
PRV	pressure-relief valve
Pt	platinum
PTFE	Polytetrafluoroethylene
RPM	revolutions per minute
RSA	Republic of South Africa
Ru	ruthenium
SiO_2	silica
SSITKA	steady-state isotopic transient kinetic analysis
STM	scanning tunnelling microscopy
TCD	thermal conductivity detector
TEM	transmission electron microscopy
TiO_2	titania
TOF	turnover frequency; defined as the number of CO molecules converted per number of surface cobalt atoms per unit of time
TPD	temperature-programmed desorption
TPR	temperature-programmed reduction
XANES	X-ray absorption near-edge spectroscopy
XPS	X-ray photoelectron spectroscopy
XRD	X-ray diffraction
Y_2O_3	yttrium oxide
ZrO_2	zirconia

Nomenclature

α	chain-growth probability (when on its own); alpha (when followed by a hyphen)
α-olefin	straight-chain olefin with double between the first two carbon atoms
β-olefin	straight-chain olefin with double between two internal carbon atoms (not the first two carbon atoms)
bar(a)	absolute pressure in units of bar
bar(g)	gauge pressure (1.0 bar below absolute pressure) in units of bar
b_i	fraction of branched compounds in a product fraction with carbon number *i*
C %	carbon percentage
C_{5+}	hydrocarbons with carbon number of 5 and higher
C_i	hydrocarbon product fraction with carbon number *i*
cm^3	cubic centimetre / millilitre
d	diameter (usually crystallite size)
fcc	face-centred cubic
g	gram
γ	gamma
hcp	hexagonal closed-packed
$K\alpha_{average}$	average between $K\alpha_1$ and $K\alpha_2$ wavelengths
$K\alpha_i$	radiation emitted when an electron drops down to a K-orbital from a higher-energy orbital; *i* indicates the orbital previously occupied by the electron
kV	kilovolts
L	metal loading
M	molar mass
mA	milliamps
m_{cat}	catalyst mass
µg	microgram
min	minute
mol %	molar percentage
ml	millilitres
µV	microvolt
n	number of atoms or crystallites (context-dependent)
N_A	Avogadro's number ($6.022141 \cdot 10^{23}$ mol^{-1})
n_c	carbon number
$\dot{n}_i$	molar flow-rate of component *i*
$o_{\alpha,i}$	linear, α-olefin fraction in the portion of linear olefins in product fraction *i*
$o_{\beta,i}$	linear, β-olefin fraction (i.e. linear olefins with internal double bonds) in the portion of linear olefins in product fraction *i*

o_i	linear olefin fraction in linear product fraction with carbon number *i*
ppm	parts per million
r_i	formation rate of product *i*
S_i	selectivity of component *i*
θ	theta
V	volume, unless otherwise stated
wt	weight
wt %	mass percentage
Y_i	yield of component *i*
X	conversion
$X_{sim.}$	simulated conversion
x_i	mole fraction of component *i*

List of Figures

List of Tables

1 Introduction

1.1 Fischer-Tropsch Synthesis

In recent decades more attention has been given to synthetic fuel production from natural gas and coal via Fischer-Tropsch synthesis (FTS) as it has shown increasing economic feasibility (Dry, 2002). More recently, interest has also been given to the production of fuels from biomass via FTS, as a more sustainable method by which fuels can be produced and used without changes being made to current processes (Damartzis and Zabaniotou, 2011; Demirbas, 2011; Boerrigter & van der Drift, 2004). While synthetic fuels have not always been cost-effective as crude oil prices fluctuated, their increased production has been motivated by problems related to the utilisation of stranded natural gas and environmental considerations (Khodakov, 2009), the general increase in crude oil prices, and increased understanding and improvement of Fischer-Tropsch technology, especially with regard to catalysis research (Dry, 2002).

Gasified coal (or biomass) or reformed natural gas is converted to the gaseous feedstock to the FTS process. This feedstock of synthesis gas (syngas) consists of carbon monoxide and hydrogen and is converted to a large variety of hydrocarbon compounds with different functionalities (Iglesia, 1997). In addition to fuel constituents and precursors, these compounds include products of higher economic values (Steynberg, 2004). As product demands have increased and crude oil-associated natural gas sources are being more efficiently utilized (Dry, 2002), more resources and attention have been given to the FTS process in both research and industry (Bezemer *et al.*, 2006).

Iron, cobalt, nickel and ruthenium are active catalysts for the hydrogenation of carbon monoxide under FTS conditions (Dry, 2004). Due to ruthenium's high cost and insufficient availability, and nickel's high selectivity to methane under FTS conditions, these metals are not used on a commercial scale (Dry, 2002). Iron catalysts are used in both the high temperature (HT) and low temperature (LT) FT processes, with the carbide form being the active phase in FTS (Schulz, 1999). Under HTFT conditions (330-350°C), iron catalysts have a greater selectivity towards oxygenates and branched hydrocarbons (Iglesia, 1997). Under LTFT conditions (200-240°C), they have a greater selectivity towards middle distillate products and waxes (Khodakov, 2009). In both cases, the water-gas shift reaction also occurs, increasing the H_2/CO ratio (Dry, 2004). Cobalt catalysts are not used under HTFT conditions as excess methane is produced (Dry, 2002). Under LTFT conditions, cobalt catalysts catalyse the formation of long-chain paraffins, constituents and precursors of diesel fuel, and also have a low activity for the competing water-gas shift reaction (Dry, 2002; Yates & Satterfield, 1991).

1.2 Cobalt Catalysts for Fischer-Tropsch Synthesis

Alumina-supported cobalt catalysts have been noted as industrially-relevant FTS catalysts (van de Loosdrecht *et al.*, 2007) and thus a more thorough understanding of their activity would be industrially and economically advantageous. In recent years, metallic cobalt has generally been between one and three orders of magnitude more expensive than scrap, reusable iron (Dry, 2002), and it is therefore necessary to increase the number of active sites available for a given mass of cobalt. It is also important that the lifetime of the catalyst is maximised to increase the economic feasibility of cobalt-based FTS. Overall activity has been found to increase with decreasing crystallite size, down to a size of about 9 nm (Iglesia, 1997). This is because, while the turnover frequency, or the number of carbon monoxide molecules converted per number of surface cobalt atoms per unit time, remains constant, the number of surface cobalt atoms available increases with decreasing crystallite size. Therefore, in order to maximise the amount of cobalt present, smaller crystallites must be employed. However, for crystallite sizes smaller than about 6-8 nm, turnover frequency has been found to decrease rapidly with decreasing crystallite size (Fischer, 2011; Bezemer *et al*., 2006). Theories exists as to why this may be the case, one of which is the ensemble theory (Ponec & van Barneveld, 1979). Ponec & van Barneveld noted that, for the complex, polymerisation-type, surface reaction of FTS to occur, there must exist a minimum number of adjacent, active catalytic sites of the appropriate geometries. The aforementioned deactivation effect with decreasing crystallite size is purely a size effect and does not take into account other important factors such as atmosphere.

The loss of activity of cobalt catalysts has also been found to occur via extrinsic factors. It has been established that cobalt catalysts are deactivated during FTS via various mechanisms that include carbon deposition, the sintering of smaller crystallites into larger ones, support migration, surface reconstruction, the formation of inactive cobalt-support compounds and oxidation (Saib *et al*., 2010; van de Loosdrecht *et al*., 2007; Bartholomew, 2001). There are also different views concerning the effect of water, the main FT product, on cobalt activity under FTS conditions. Elevated water concentrations (present at higher FT conversion conditions as water is the main FT product) has different effects on cobalt catalysts, depending on the support. In the cases of alumina, silica and titania supports, water addition has resulted in either enhanced activity or deactivation (Lögdberg *et al*., 2011; Storsæter *et al*., 2005; Bertole *et al*., 2002; Krishnamoorthy *et al*., 2002; van Berge *et al*., 2000).

It has been postulated that water is responsible for deactivating cobalt catalysts by oxidation (van de Loosdrecht *et al*., 2007; van Berge *et al*., 2000; Hilmen *et al*., 1999; Rothaemel *et al*., 1997) or by enhancing other deactivation mechanisms such as sintering (Bezemer *et al*., 2010; Bartholomew, 2001), especially in the case of smaller crystallites, because of their higher surface energy (van Steen *et al*., 2005). Thermodynamic calculations (van Steen *et al*., 2005) indicate that smaller cobalt-based crystallites under FTS conditions, at higher water concentrations, are thermodynamically more stable in the oxidised form. Various research groups (Fischer, 2011; Bezemer *et al*., 2010; van de Loosdrecht *et al*., 2007; Storsæter *et al*., 2005) have studied cobalt catalysts under FTS conditions with respect to crystallite size and water effects. Using *ex-situ* and *in-situ* techniques, these research groups found that cobalt may be oxidised under FTS conditions with crystallite size and water

concentration dependencies that correlate with thermodynamics. However, until this time, the oxidation of cobalt crystallites under FTS conditions has not been directly observed.

1.3 Research Techniques

A number of *in-situ* and *ex-situ* methods have been employed in order to understand the performance and stability of cobalt catalysts under FTS conditions, especially for crystallite sizes smaller than 8 nm, and at elevated water concentrations, as results obtained by various groups have been contradictory (van de Loosdrecht *et al*., 2007; Bezemer *et al*., 2006).

A useful and non-invasive characterisation technique for studying crystalline solids is X-ray diffraction (XRD), or powder X-ray diffraction. This provides the identities and certain physical characteristics of a powder mixture of crystalline compounds. *Ex-situ* characterisation identifies the compounds while they are not undergoing chemical modification. This can be done by XRD or a number of other methods, such as Transmission Electron Microscopy (TEM). TEM yields a good representation of crystallites and the means to calculate their size distributions at the nano-scale by high-definition micrographic imagery. Due to the limitations of *ex-situ* techniques, in that direct analysis of catalyst changes cannot be performed under reaction conditions, important information remains concealed. Moreover, it is difficult to preserve spent catalyst samples for *ex-situ* analysis, as they can be easily oxidised upon exposure to air (Mansker *et al*., 1999), thereby inducing further changes to the catalyst. In fact, in some instances, the degree of oxidation of a spent catalyst sample has to be used to determine the extent of success of a passivation technique between extraction and *ex-situ* analysis (Shroff & Datye, 1996).

In-situ characterisation techniques can facilitate the direct observation of catalysts under reaction conditions, during which they may be rapidly transformed. XRD instruments are capable of studying crystalline solids in gaseous environments at elevated pressures and temperatures, such as those found during FTS, provided a suitable reaction cell is employed. The information generated can be used to determine the effects of the reaction conditions on phases present, when they change and the extent of sintering, using Rietveld refinement for size analysis. For example, an appropriate *in-situ* XRD reaction cell can elucidate, under FTS conditions, precisely at which crystallite sizes and water concentrations the oxidation of cobalt catalysts can be expected to occur.

1.4 Project Overview

The aim of the current study was to develop and commission a suitable *in-situ* XRD reaction cell that can be used for the characterisation of Fischer-Tropsch and other heterogeneous catalysts under reaction conditions. The effects of water on a γ-alumina-supported cobalt catalyst under LTFT synthesis conditions were investigated, especially with regard to oxidation and sintering. Water at partial pressures between 0-3 bar, representing extents of conversion up to 91%, was co-fed with the syngas. At these elevated water concentrations, the catalyst composition changes were studied using

the *in-situ* XRD reaction cell. Two catalysts with initial, average Co_3O_4 crystallite sizes of 6.7 nm and 11.1 nm (XRD), respectively, were studied in order to examine possible crystallite size effects with regard to oxidation by water during FTS. Using the *in-situ* XRD reaction cell, information regarding sintering, oxidation and composition was revealed.

1.5 Report Outline

A literature review has been conducted concerning the relevant information about supported, cobalt catalysts under FTS conditions, along with their deactivation mechanisms, crystallite size effects and water effects. The materials used and methods employed have been recorded so that the work performed can be reproduced. The results of the catalyst characterisation, including *ex-situ* TEM and XRD, *in-situ* XRD spectra and analysis, and online and offline gas chromatography results (for catalyst activity and product selectivity) are presented. The results include the design and development of the *in-situ* XRD reaction cell. In a subsequent section, discussion has been made regarding the results obtained, comparing the two catalyst crystallite sizes and what has been found by other research groups. Conclusions have been drawn based on the results obtained and the understanding thereof, and recommendations have been made for improvements to the cell and further experiments that can be performed.

2 Literature Review

The following review of the literature has been compiled in order to understand the context of the current study, including what is presently known about cobalt-based Fischer-Tropsch synthesis (FTS) and *in-situ* X-ray diffraction (XRD). The commissioning reaction, the cobalt-catalysed FTS, is briefly described. An outline of the preparation methods of and supports used for cobalt catalysts is then given. A number of deactivation mechanisms of cobalt catalysts under FTS conditions are discussed, including coking, sintering and the effects of water presence. Cobalt crystallite size effects and water concentration effects are discussed, especially with regard to their influence on catalyst activity and product selectivity. These two sections are given more attention due to their importance in this study. Understanding the changes of cobalt catalysts under FTS conditions can be achieved via *ex-situ* and *in-situ* techniques, and this comparison is made in the last section. Recent developments regarding *in-situ* techniques are then highlighted, especially in the context of XRD.

2.1 The Low-Temperature Fischer-Tropsch Synthesis

Cobalt catalysts for FTS are used only in the Low-Temperature Fischer-Tropsch (LTFT) process as excess methane is produced at higher temperatures (Dry, 2002). Under LTFT conditions, lighter hydrocarbon products consist mainly of linear olefins, while heavier hydrocarbons are mainly paraffinic (Iglesia, 1997). The product spectrum obtained consists of longer, paraffinic hydrocarbons than what is produced with iron-catalysed LTFTS (Dry, 2002). Their high selectivity towards long-chain paraffins makes cobalt catalysts useful in the production of diesel fuel and precursors to diesel fuel (Prieto *et al.*, 2009).

Chain-growth pathways for FTS via insertion have been proposed (figure 2.1), where CH_2 "monomers" are involved in chain growth for the formation of olefins and paraffins. The CH_2 species is not a true monomer as it is formed only "*in situ*", but it is understood to partake in chain growth ("α" in figure 2.1) in a polymerisation-type reaction. Adsorbed species can desorb ("d" in figure 2.1) from the catalyst surface as α-olefins, bond with other monomers to continue chain growth, or be hydrogenated to paraffins, and then desorb (Dry, 2002). This is illustrated in figure 2.1, without assuming any particular reaction kinetics.

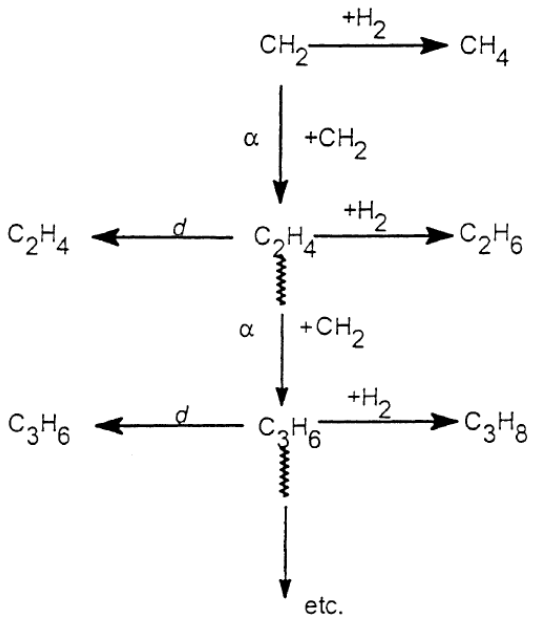

Figure 2.1: Stepwise chain-growth and product desorption pathways in FTS (Dry, 2002).

Desorbed α-olefins can subsequently adsorb onto the catalyst surface and grow longer, be hydrogenated, undergo isomerisation by double-bond shift, or remain in the gas/liquid product phase as primary FT products (Schulz & Claeys, 1999).

The product spectrum, based on carbon number distribution, obtained from cobalt-catalysed FTS can be varied by operating temperature, promoter type and amount, reactor type (Dry, 2004), reactor residence time, and, particularly, the partial pressures of H_2 and CO (Schulz, 2003), *inter alia*. LTFTS is aimed at maximum wax production and the hydrocarbons produced are predominantly linear. Cobalt produces a more saturated product than does iron, as it has a greater hydrogenation activity, while both catalysts produce no aromatics at these conditions (Dry, 2004). Dry (2004) indicated that product selectivity was effectively a function of chain-growth probability, which can increase with carbon number (Schulz, 2003; Iglesia, 1997). The increase in chain-growth probability has been attributed to desorption inhibition in addition to carbon number-dependent olefin re-incorporation (Schulz & Claeys, 1999; Iglesia, 1997; Schulz *et al.*, 1997). Branching probability has been found to decrease with time for cobalt and nickel until a constant value is obtained. Branching is inhibited by spatial constraints while chain-growth space requirements are less demanding (Schulz, 2003).

The product spectrum depends on many factors, with the catalyst's properties arguably being the most important. Catalyst preparation is therefore essential, especially in studying model catalysts and their effects on FTS.

2.2 Preparation Methods of Cobalt Catalysts for FTS

A number of different preparation techniques have been implemented to produce cobalt catalysts. These include deposition-precipitation (Bezemer *et al.*, 2006), co-precipitation (Schulz & Claeys, 1999), electrostatic adsorption of cobalt complexes, reverse micelle techniques (Fischer *et al*., 2011; Prieto *et al*., 2009), mixed sol-gel procedures (Okabe *et al.*, 2004) and incipient wetness impregnation (Panpranot *et al.*, 2002).

The preparation method, which can affect the resultant cobalt structure, and the support used can influence the cobalt activity and selectivity under FTS conditions (Reuel & Bartholomew, 1984). Khodakov (2009) noted that metallic cobalt is predominantly present in the face-centred cubic (fcc) phase on titania, alumina and silica supports that have been reduced at temperatures above 450°C. From thermodynamic analysis, van Steen *et al.* (2005) found that the fcc phase is more stable than is the hexagonal closed-packed (hcp) phase for cobalt crystallites below 100 nm in size, the typical range of sizes for cobalt crystallites in FTS catalysts. Kitakami *et al*. (1997) reported that the fcc phase is the most stable cobalt phase for crystallite sizes below 20 nm, above which the hcp phase is more stable in increasing proportions until a crystallite size of 40 nm. Crystallites larger than 40 nm consist predominantly of the hcp phase (Kitakami *et al*., 1997). The type of phase and the crystallite size influence the number of surface atoms present in addition to the reactivity of the sites, since different sites are suspected to catalyse different reactions under FTS conditions (Schulz *et al*., 2002; Schulz, 1999).

The catalyst calcination and reduction pre-treatments can have significant effects on catalyst performance (Khodakov *et al.*, 2007). Incomplete reduction during catalyst preparation results in cobalt oxide crystallites being present, especially with smaller precursor crystallites. These are inactive towards FT products as it is thought that FTS takes place on only metallic cobalt (Bezemer *et al.*, 2006). Maximum productivity is thus not achieved, resulting in economic inefficiencies in the case of industrial operation. Therefore, careful attention must be given to every step of the preparation process, especially for fine-tuning catalyst properties in the case of the production of model catalysts, the study of which results in increased understanding, which is then transferrable to industrial application.

2.3 Support Materials

Studying cobalt catalysts with different supports requires appropriate research techniques and analysis for understanding their different effects. Coupled with the preparation method, the chosen support influences whether a catalyst is a model catalyst that can be used for accurate research with direct industrial relevance.

Industrially-employed supports in FTS include alumina, silica and titania. It has been found that supports with high surface areas tend to result in high cobalt dispersions (Zhang *et al.*, 2002), depending on the preparation method. Maintaining high dispersions, or preventing sintering,

respectively, are the main roles of supports. Supports also influence the diffusion of reactants and products and chemical and mechanical strength (Jean-Marie *et al.*, 2009).

Storsæter *et al*. (2005) synthesised alumina-, silica- and titania-supported cobalt catalysts. The calculated BET surface areas were 161, 297 and 8 m^2/g, respectively. While the average pore diameter for the alumina and silica catalysts were similar (6.7 and 11 nm, respectively), the titania's pore diameter was reportedly 770 nm. As a result of the different characteristics of the supports, the average cobalt crystallite sizes, according to XRD, were 11, 20 and 39 nm for the alumina, silica and titania catalysts, respectively. Storsæter *et al*. (2005) found the turnover frequencies to be identical for each catalyst, regardless of support identity. While the turnover frequency for the cobalt crystallites on these supports is expected to be the same (Iglesia, 1997), the overall activity (i.e. per gram of metal) would be different, given their different dispersions (with high-area supports going together with high cobalt dispersions).

Saib *et al.* (2002) studied the effects of support pore diameter on reducibility of silica-supported cobalt catalysts, synthesised by the method of incipient wetness impregnation. Pore diameter of the support affected the resultant crystallite size. It was determined that crystallite size increased as pore diameter increased. By temperature-programmed reduction (TPR) they found that as pore diameter increased, the amount of hydrogen consumed decreased. Accordingly, they concluded that as pore diameter increased so did the degree of reduction. They also found that product selectivity during FTS varied with pore size. Pore diameter affected reactant transport and secondary reactions of olefins while C_{5+} selectivity was attributed to be a function primarily of conversion. Alternatively, the effects on product selectivity may have been more significantly a function of crystallite size which is in turn affected by pore diameter.

While oxide supports are generally inert under FTS conditions, they can have an effect on catalyst activity and selectivity. For example, the acidity of the support affects branching. Strongly-acidic ZSM-5 produced branched products while weakly-acidic supports, such as the aforementioned oxides, produced straight-chain FT products (Zhang *et al.*, 2002). They can also have electronic effects on smaller metal crystallites (Jean-Marie *et al.*, 2009), which in turn affect selectivity and activity.

Ma *et al*. (2011) conducted kinetic studies on cobalt-catalysed FTS, on both alumina and silica supports. They suggested that kinetic parameters indicated that the support type affected FT performance, with differences possibly reflecting CO adsorption behaviour. Ma *et al*. deemed Co-Al_2O_3 interactions to be stronger than Co-SiO_2 interactions, noting that the FTS reaction rate would be influenced by water in different ways, depending on the cobalt-support interactions.

2.4 Intrinsic and Extrinsic Deactivation Mechanisms

The relative cost of cobalt, compared with iron, makes regular replacement (in the order of weeks) economically unfeasible for cobalt catalysts, while this is done for iron catalysts. It is thus necessary to understand the mechanisms behind cobalt catalyst deactivation and to minimise the rate of decline in activity (Dry, 2004) and increase the catalyst lifetime. During the first 30-40 days of time on stream, cobalt catalysts can be deactivated by about 40%, with the greatest rate of deactivation occurring within the first 20 days (Saib *et al.*, 2006). This is illustrated in figure 2.2.

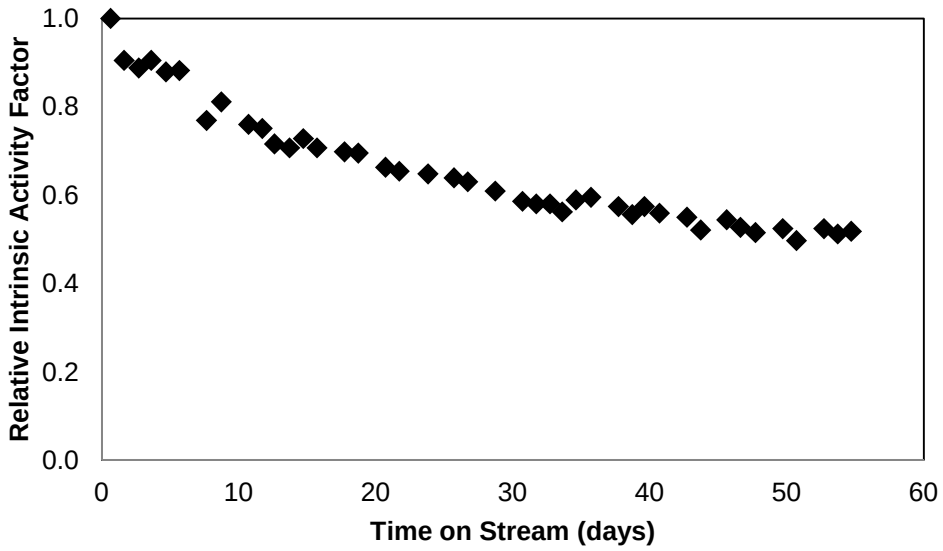

Figure 2.2: Relative intrinsic activity factor (RIAF) for a $Co/Pt/Al_2O_3$ catalyst during FTS (230°C, 20 bar, $H_2/CO = 2$, CO 50-70% conversion) with P_{H_2O}/P_{H_2} = 1-1.5 (Saib *et al.*, 2006).

After about 30-40 days the cobalt deactivates more gradually (Moodley *et al.*, 2009; Saib *et al.*, 2006). It is considered that a number of deactivation mechanisms exist for cobalt catalysts under FTS conditions, including carbon deposition, sintering, surface reconstruction, support migration and oxidation (van de Loosdrecht *et al.*, 2007). Cobalt can be poisoned by sulphur compounds, ammonia and metal carbonyls (Bartholomew, 2001) but these will not be considered here as they lie outside the scope of this study. Three main areas of deactivation have been described, with coking and water presence being extrinsic factors and sintering, while affected by extrinsic factors, being an intrinsic one.

2.4.1 Coking

Carbon deposition on cobalt under LTFT does not occur to any appreciable extent (Dry, 2004). Metallic cobalt's low activity for the water-gas shift reaction results in negligible quantities of CO_2 being produced. This also indicates that the Boudouard reaction does not occur and so no free carbon is expected to be produced via this reaction. Dry (2004) suggested that the observed decline in catalyst activity could be due to a build-up of heavy waxes on the surface and inside the pores, inhibiting the diffusion and adsorption of reactants. Fischer-Tropsch synthesis has been classified as a coke-

insensitive reaction as adsorbed carbon species are hydrogenated and filamentous carbon formation occurs at temperatures above those of HTFT (Bartholomew, 2001). Moodley *et al.* (2008) found polymeric-type carbon to build up on cobalt crystallites and alumina support during FTS. They speculated that the gradual build-up of the carbon on the catalyst may contribute to longer-term catalyst deactivation.

2.4.2 Water Presence

The presence of water in FTS is a major cause of cobalt catalyst deactivation (Dry, 2004). Cobalt catalytic properties change significantly in the presence of water, usually causing deactivation and changes in selectivity (Rothaemel *et al.*, 1997). Oxidation in the presence of water has been postulated (van de Loosdrecht *et al.*, 2007), but is size- (Saib *et al.*, 2006) and structure-dependent, and has never been directly observed (van de Loosdrecht *et al*., 2007; van Berge *et al*., 2000). Water may enhance deactivation mechanisms other than oxidation (van de Loosdrecht *et al.*, 2007), such as the formation of new, catalytically inactive phases, e.g. cobalt aluminate or silicate, in addition to sintering (Bartholomew, 2001). Water effects on cobalt catalysts under FTS conditions are discussed in more detail in section 2.6.

2.4.3 Sintering

Sintering is a prevalent deactivation mechanism for cobalt catalysts in FTS (Saib *et al.*, 2010), contributing up to about 30% of cobalt catalyst deactivation (Overett *et al.*, 2008). As catalyst crystallites are reduced in size, they have a higher tendency to sinter (Overett *et al.*, 2008). This is because smaller, nano-sized crystallites have a higher surface energy (van Steen *et al.*, 2005) and are therefore thermodynamically unfavoured. The active surface area of a catalyst may then be reduced by crystallite growth, driven by the thermodynamically-favoured minimisation of the surface energy of the catalyst crystallites (Tsakoumis *et al.*, 2010).

Generally, it has been found that sintering of supported metal catalysts occurs to a greater extent above 500°C and is promoted by the presence of water vapour (Bartholomew, 2001), the most prevalent FT product. While FTS synthesis occurs well below 500°C, it is a highly exothermic reaction, increasing the potential for sintering (Tsakoumis *et al.*, 2010), especially in the presence of severe heat transport limitations. Geerlings *et al.* (1999) noted that FTS can be operated only in a narrow temperature range; accordingly, reactors have been designed so as to remove severe heat transport limitations. Therefore, temperature effects are ruled out as major drivers for the sintering of catalyst crystallites.

Bartholomew (2001) noted that sintering can occur via atomic and crystallite migration whereby larger crystallites are formed by coalescence, with the rate of occurrence depending on temperature, atmosphere, support, crystallite size and metal loading, *inter alia*. Another mechanism via which sintering can occur is Ostwald ripening, in which the crystallites are transported through the vapour phase by volatiles formation and atomic diffusion. Again, this usually requires much higher

temperatures than those used in FTS (Bartholomew, 2001). Atomic species and volatile compounds are expected to be formed more easily with reducing crystallite size (van Steen, 2010), with larger crystallites having a lower tendency to sinter (Overett *et al.*, 2008). In this process, material is transported from the smaller crystallites and added to the larger crystallites, reducing the overall dispersion. As a result, the average crystallite size increases with time and the rate of sintering decreases as there are fewer small crystallites to be converted to larger ones. This effect can be seen in figure 2.3.

Kiss *et al.* (2003) synthesised amorphous silica-supported, rhenium-promoted cobalt catalysts. The average crystallite size of the fresh catalyst was about 5 nm (TEM). After FTS (220°C, 35 bar, H_2/CO = 2.1, 95% conversion) the average crystallite size was found to have increased to about 11 nm. In another experiment (20 bar, 80% conversion) with the same fresh catalyst, the average crystallite size was found to have increased to about 8 nm. From the catalyst tests it was inferred that water had induced the transformation of the active cobalt. The greater size increase (i.e. the increase to 11 nm) was observed after the reaction that was run at a higher conversion, correlating to a higher water partial pressure. They found that steam-treated fresh catalyst and spent FTS catalyst had similar phases and thus proposed that cobalt crystallites smaller than 10 nm in diameter deactivate under high-conversion FTS conditions by forming cobalt-support oxides.

Saib *et al.* (2010) analysed the change in alumina-supported, platinum-promoted cobalt crystallite size with TEM/HAADF before and after FTS (230°C, 20 bar, H_2/CO = 1.25-2.0, 50-70% conversion). From an initial average crystallite size of 7 nm, the average crystallite size was found to have increased to about 15 nm. Overett *et al.* (2008) also found the average cobalt crystallite size to increase, from about 10 nm to about 15 nm, within the first 10-20 days of FTS (same conditions as those used by Saib *et al*., 2010), after which the size appeared to remain constant.

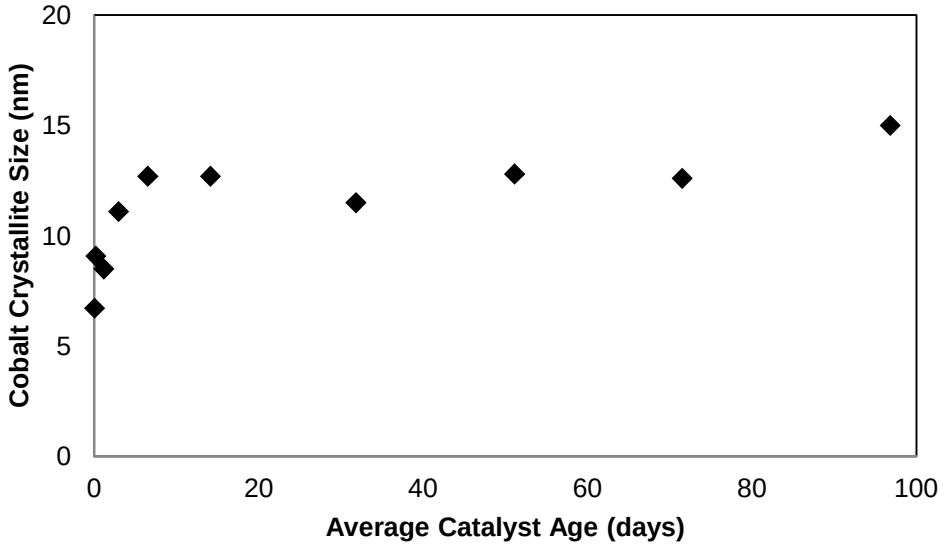

Figure 2.3: Average surface area-weighted cobalt crystallite size (determined by TEM/HAADF) as a function of average catalyst age (Overett *et al.*, 2008).

Sintering is thus deemed mainly to be an intrinsic deactivation mechanism because it is dependent on crystallite size, of which surface energy is an important thermodynamic function. However, it has been found that sintering can be enhanced by external conditions, such as elevated water concentration.

2.5 Cobalt Crystallite Size Effects under FTS Conditions

The size of cobalt catalyst crystallites under FTS conditions has been found to affect both catalytic activity and product selectivity, which are functions of the complexity of the FT reaction.

2.5.1 Activity

FTS has been referred to as a structure-insensitive reaction (that is, the turnover frequency, or activity per cobalt site, does not depend on crystallite size) (Fischer *et al*., 2011; Bezemer *et al*., 2006; Iglesia, 1997), but it becomes structure-sensitive for smaller crystallite sizes, depending on support (den Breejen *et al.*, 2010) and operating conditions (Bezemer *et al.*, 2006). Ponec and van Barneveld (1979) alluded to the structure-sensitivity of FTS, noting that the right crystallite size of a catalyst corresponds to an optimal combination of certain crystallographic sites. They concluded that FTS requires an ensemble of a minimum number of active sites of the appropriate geometries to occur.

Using alumina, silica and titania supports for cobalt catalysts under FTS conditions (200°C, 20 bar, H_2/CO = 2.05, 55-65% conversion), Iglesia (1997) found that turnover frequency (TOF) remained constant as crystallite size decreased from 200 to 9 nm, showing that cobalt-catalysed FTS is structure-insensitive for sizes above 9 nm. Ho *et al.* (1990) also found the TOF to be invariant for crystallite sizes above 10 nm, in FTS (185°C) studies with silica-supported cobalt catalysts. Ho *et al.* noted that TOF values were constant as the electronic properties of cobalt metal were not expected to vary within the studied dispersion range.

Bezemer *et al.* (2006) synthesised cobalt catalysts with crystallite sizes between 2.6-27 nm (measured using XPS) on carbon nanotubes (CNT), as this support is considered to eliminate cobalt-support interactions which have been found to be present with oxide supports, especially with small catalyst crystallite sizes (Bartholomew & Reuel, 1985). Under FTS conditions (220°C, 35 bar, H_2/CO = 2, 60% conversion), Bezemer *et al.* determined the TOF to be independent of size between 8-27 nm, while it decreased with decreasing size from 8 to 2.6 nm. The tests were also conducted at 1 bar and 2% conversion and the same trends were found, with 6 nm being the size below which the TOF decreased with decreasing crystallite size (figure 2.4).

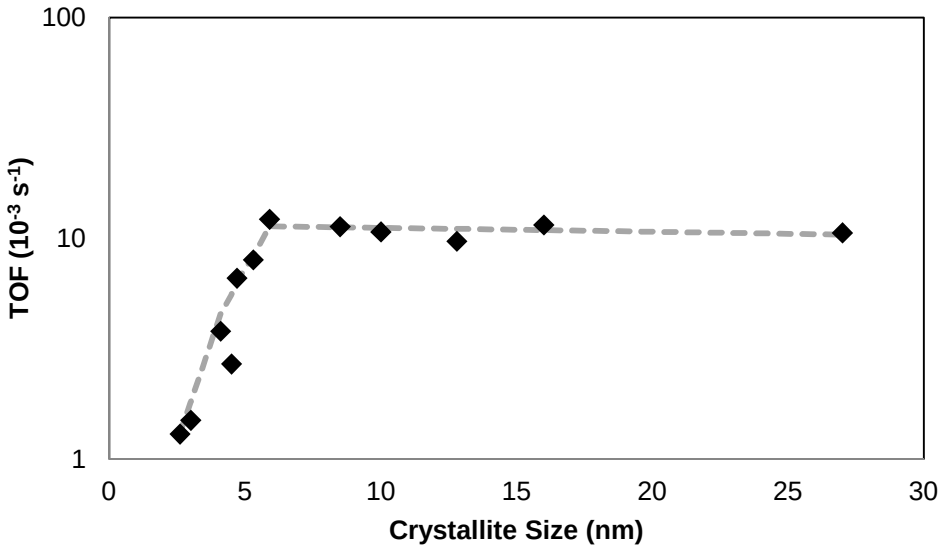

Figure 2.4: The influence of cobalt crystallite size on TOF (220°C, 1 bar, H_2/CO = 2, 2% conversion) (Bezemer *et al.*, 2006).

Under steady-state isotopic transient kinetic analysis (SSITKA) during FTS (210-220°C, 1.85-35 bar, H_2/CO = 2 or 10), den Breejen *et al.* (2009), who also studied CNT-supported cobalt catalysts, found the TOF to be independent of crystallite size for sizes greater than 6 nm (XPS). For catalysts of sizes smaller than 6 nm, the TOF decreased with decreasing crystallite size.

Prieto *et al.* (2009) (using ITQ-2 as support) and Trépanier *et al.* (2010) (using CNT as support) made the same observations for TOF of cobalt-catalysed FTS with crystallite sizes below approximately 10 nm (measuring techniques were H_2-chemisorption and XRD, for the respective groups). Fischer (2011), in studying alumina-supported cobalt catalysts under FTS (190°C, 9.9 bar, H_2/CO = 2, < 10% conversion) found the same trends, in that TOF decreased with decreasing crystallite size. In FTS and experiments he found that a cobalt catalyst with an average crystallite size of 4.7 nm was the most active (per gram of catalyst present) in the initial experimental stages. This same catalyst, during temperature-programmed desorption of carbon monoxide, catalysed the formation of the most methane. For this size he noted that the maximum number or combination of active sites for CO dissociation and methane production per mass of catalyst is present.

Den Breejen *et al.* (2009) inferred, from SSITKA results, that CO was bonded irreversibly to cobalt for crystallites smaller than 6 nm, resulting in a reduction in TOF. They explained that CO bonded with surface atoms with a lower coordination number (corner and edge atoms), which may have been due to an increased localization of valence electrons. Bezemer *et al.* (2006) measured (using EXAFS) a decrease in the cobalt coordination number of the catalyst in the presence of syngas. It could be expected that the resultant surface would exhibit greater chain-growth probability, as low-coordination number sites are those responsible for chain-growth (Schulz, 2003). However, den Breejen *et al*. (2009) found CO adsorption energy to increase significantly with decreasing cobalt cluster size. This would reduce the number of free, active sites available for FTS as more irreversibly-

bonded CO would cover the surface. It may thus be concluded that there is an optimal size at which chain-growth occurs.

Ma *et al.* (2011) studied the reaction kinetics of FTS (220°C, up to 20 bar, H_2/CO = 1-2.5) catalysed by alumina- and silica-supported cobalt catalysts (8-40 nm). It was found that cobalt crystallite size influenced reaction order, rate constant and the degree to which water affected the reaction rate. For the alumina-supported catalyst, it was inferred that CO adsorption was much stronger than H_2 adsorption, with the results indicating that more active sites were occupied by CO molecules than by H_2 molecules, resulting in a suppression of the FT reaction rate. An increase in the reaction rate constant was observed with a decrease in crystallite size, attributed to a higher active cobalt surface site density. It was found that the presence of water negatively affected the reaction rate on the alumina-supported catalyst, while it had a positive effect on the silica-supported one. It was considered that, at higher conversion levels, the greater water partial pressure would have a more significant negative effect on the reaction rate. Upon further reduction in crystallite size, inhibition of the FT rate by strongly-adsorbed CO appeared to decrease, while adsorbed H_2 appeared to favour dissociation.

Similar crystallite size effects under FTS have been observed with ruthenium and iron, in that activity decreased with decreasing crystallite size below 10 nm (Barkhuizen *et al.*, 2006); and for rhodium, where activity decreased with decreasing crystallite size below 30 nm (Mungwe, 2012; Ojeda *et al.*, 2004).

2.5.2 Selectivity

FTS is an important reaction insofar as valuable products can be produced. Methane is undesirable as a product as it is often used as a feedstock and is of far lower economic value than the C_{2+} products (hydrocarbons with at least 2 carbon atoms per molecule). The C_{5+} product category (liquid at room temperature and pressure) contains many of the valuable products of FTS which have various chemical characteristics. One indication of the economic feasibility of a catalyst and the accompanying reaction conditions is the product spectrum, especially with regard to methane and C_{5+} selectivity, in addition to the C_{2-4} product category, which contains valuable products such as ethene and propene.

In studying cobalt-catalysed FTS (1 bar), Bezemer *et al.* (2006) found methane selectivity to increase as crystallite size decreased for sizes below 6 nm. This indicated a lower presence of sites active for chain growth, resulting in an increase in hydrogenation of primary carbon species, forming methane (Bezemer *et al.*, 2006). The catalysts with crystallite sizes below 6 nm had a much greater paraffin/olefin ratio than those with larger sizes. This trend was in agreement with that of the higher methane selectivity for the smaller crystallites, indicating greater hydrogenation activity on the smaller crystallites. However, Bezemer *et al*. noted that the differences in the space velocities for the different tests may have been responsible for secondary hydrogenation and thus partly for the higher paraffin/olefin ratio. Schulz (2003) identified spatial constraints on active sites as contributors to

olefin hydrogenation, making the formation of paraffins as end-products easier. From these results it can be concluded that secondary hydrogenation occurs more readily for smaller crystallites (Schulz, 2003).

Prieto *et al.* (2009) and Trépanier *et al.* (2010) found methane selectivity to increase and C_{5+} selectivity to decrease with decreasing crystallite size below about 9 nm. Bezemer *et al.* (2006) also found C_{5+} selectivity to decrease with decreasing crystallite size below 8 nm. den Breejen *et al.* (2009) determined hydrogen coverage to be independent of size for cobalt crystallite sizes greater than 6 nm. Below that, it was inferred that hydrogen coverage increased as size decreased, contributing to the increased methane selectivity (due to more hydrogen being available for hydrogenation) for crystallite sizes below 6 nm. Yang *et al.* (2010) speculated from their results that larger crystallites can stabilise the transition states of chain propagation intermediate species better than can smaller crystallites, within their studied range of sizes (4-15 nm), indicating that larger crystallites (in the 4-15 nm size-range) have a higher inherent chain propagation probability.

The size of crystallites also affects the geometries of the catalyst sites present. The number of edge and corner atoms (on-top sites) is expected to increase as crystallite size decreases, resulting in a larger fraction of linearly-adsorbed CO (den Breejen *et al.*, 2009), compared with bridge-type adsorbed CO. According to Zhang *et al.* (2007), larger cobalt crystallites allow bridge-type adsorption of CO, which results in a lower selectivity to methane and a higher chain-growth probability, which was in contradiction to what Schulz (2003) considered. Dry (1996) noted that either linear-adsorbed or bridge-type adsorbed CO can lead to the formation of the CH_2 "building block", and thus to chain-growth, with the route via linear-adsorbed CO being the more likely one over cobalt and iron catalysts.

Bezemer *et al.* (2006) suggested, in the knowledge that FTS may consist of a large variety of elementary reaction steps (Claeys & van Steen, 2004), that a number of different sites could be required. Schulz (2003) noted that different cobalt sites exist for different reactions and these sites may appear or disappear during reaction. 6-8 nm was the range of sizes proposed for the existence of the optimal fraction of active sites (Bezemer *et al.*, 2006), which maximises overall activity in addition to selectivity towards C_{5+} compounds. The right proportion of active sites could be the ensemble mentioned by Ponec and van Barneveld (1979). Therefore, as cobalt crystallites are reduced in size, the number of sites of the appropriate geometries for chain-growth decreases. Khodakov (2009) noted that deactivation of cobalt catalysts may also contribute to the differences in selectivity with decreasing crystallite size (e.g. certain active sites may be deactivated and thus removed from an ensemble, resulting in a different product spectrum).

2.6 Water Effects on Cobalt Catalysts under FTS Conditions

The effects of water on cobalt and FTS are not well understood and depend on catalyst crystallite size and support. Water has been found to have both positive and negative effects, with water concentration being an important factor. Water has been found to result in deactivation of cobalt catalysts under FTS conditions, promoting sintering of metallic cobalt crystallites, surface oxidation and the formation of FT-inactive cobalt-support compounds (Dry, 2004)

Under FTS conditions, cobalt metal is much more resistant to oxidation by water than is iron. Furthermore, it shows a much lower water gas-shift activity than does iron (Dry, 2002). The water partial pressure term is absent from most kinetic equations for FT synthesis over cobalt catalysts (Yates & Satterfield, 1991). While the effect of water on FT reaction kinetics has not been correlated to oxidation, it has not been possible to distinguish water-induced changes in catalyst activity between changing kinetics and deactivation, due to the absence of appropriate *in-situ* characterisation tools. van Berge *et al.* (2000) claimed that water did not affect the FT kinetics with cobalt catalysts in their study and thus used a rate equation in which there was no water partial-pressure term. Conversely, Kiss *et al.* (2003) found that the deactivation of supported cobalt catalysts was induced by the presence of water, whether due to increased conversion or upon co-feeding. Ma *et al.* (2011) found that water can in fact affect the FT reaction rate, having a negative effect on Co/Al_2O_3 catalysts and a positive effect on Co/SiO_2 catalysts. These effects become more significant at higher conversion levels, i.e. when the water partial pressure is higher. This was confirmed by Yu *et al.* (2007), who found the reaction rate to decrease with increasing time on stream (i.e. increasing water partial pressure) under FTS conditions (210°C, 20 bar, H_2/CO = 2.1, 50% conversion). Schulz *et al*. (1997) found reaction rate to remain constant with increasing water partial pressure under FTS conditions over a Co/ZrO_2/Aerosil/Ru catalyst. It was concluded that water does not affect the steps of CO adsorption and conversion to the CH_x intermediate (Schulz *et al*., 1997).

2.6.1 Activity

There are differing viewpoints as to the reasons for the deactivation of supported cobalt catalysts. Hilmen *et al.* (1999) and van de Loosdrecht *et al.* (2007) noted that the discrepancies in the literature are probably due to differences in operating conditions, support materials, promoters and preparation methods, *inter alia*. The oxidation of cobalt metal to cobalt oxide or cobalt aluminate (when alumina is the support) by the product water has been postulated to be a major cause of the deactivation of supported, cobalt FTS catalysts (Hilmen *et al.*, 1999). Krishnamoorthy *et al.* (2002) noted that water has been found to increase FTS reaction rates in cobalt systems with silica and titania as supports, but decrease reaction rates where manganese oxide or alumina was used.

Hilmen *et al.* (1999) used a fixed-bed reactor for FTS (210°C, 13 bar, H_2/CO = 2.1) to investigate the effects of water on alumina-supported cobalt catalysts with an average crystallite size of 21 nm (XRD). The catalysts were prepared by incipient wetness impregnation of the supports with aqueous solutions of Co- and Re-containing salts. They were analysed *ex situ*, using various techniques including TPR, TPD, XRD, XPS, pulse adsorption, gravimetry and kinetic experiments. For both Re-

promoted and unpromoted cobalt catalysts, they found, upon the addition of water at a P_{H_2O}/P_{H_2} inlet ratio of 1.5, which corresponds to a conversion of about 73%, that the relative reaction rate decreased, with the unpromoted catalyst losing about 40% of its initial activity (see figure 2.5).

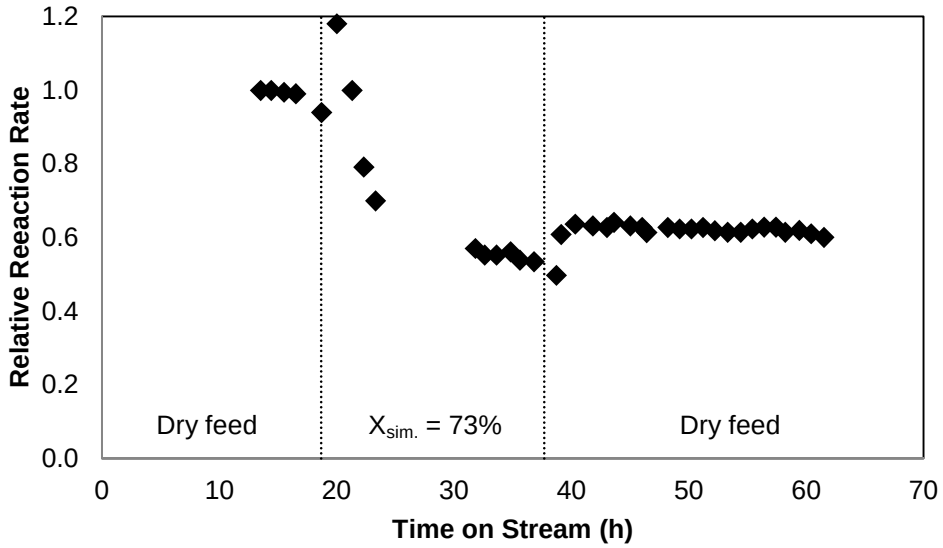

Figure 2.5: Reaction rate relative to the rate of CO consumption as a function of time. Feed composition: 50 mol % (H_2 + CO), H_2/CO = 2.1, balance N_2 + He or N_2 + He + H_2O, P_{tot} = 13 bar, T = 210°C (Hilmen *et al.*, 1999).

Similarly, Storsæter *et al.* (2005) found that the reaction rate decreased with time on stream with a dry feed to a FTS reactor (210°C, 20 bar, H_2/CO = 2.1, conversion = 40-45%) containing alumina-supported cobalt catalysts with an average crystallite size of 11 nm (XRD). Upon addition of water with a P_{H_2O}/P_{H_2} inlet ratio of 0.38 (corresponding to a simulated conversion of 36%), the rate decreased further. When a greater partial pressure of water (P_{H_2O}/P_{H_2} = 0.76, corresponding to a simulated conversion of 59%) was added to the feed, the rate decreased to a greater extent. After the water was removed from the feed, the rate of reaction increased. However, the water effects on activity were apparently irreversible, as the reaction rate in the second dry period was only about 67% of the reaction rate in the initial dry period (see figure 2.6).

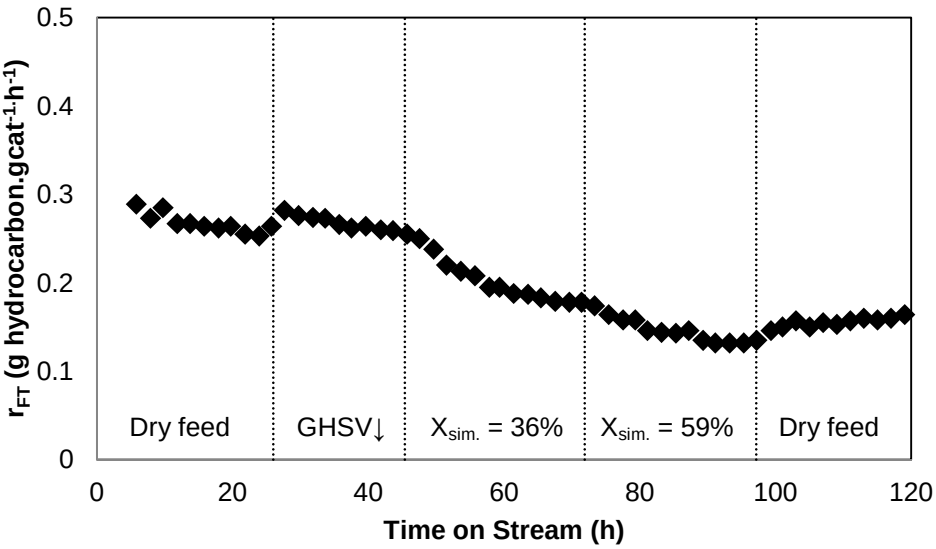

Figure 2.6: Observed reaction rate for formation of hydrocarbons as a function of time on stream 5 hours after start-up for Co (●) and Co-Re (○). P_{tot} = 13 bar, T = 210°C (Storsæter *et al.*, 2005).

Similar trends were observed in both sets of results, and in the work of Hilmen *et al*. (1999) in the cases of both the promoted and unpromoted catalysts, while to differing degrees depending on whether or not the catalyst was promoted. Hilmen *et al.* claimed that the high water partial pressures caused the rapid deactivation of the catalysts, with the unpromoted catalyst being deactivated to a lesser extent. The rate of deactivation decreased with time, as expected from fewer remaining active sites being available. Storsæter *et al.* (2005) proposed that some, but not all, deactivation caused by the water during reaction was reversible. They suggested that the deactivation was due to reoxidation of cobalt metal.

Hilmen *et al.* found that total oxidation to Co_3O_4 was not observed for all Co sites. For both catalysts, phases that interacted strongly with the alumina supports were formed. From analyses with gravimetry, TPR and XPS, no detection was made of any reoxidation of the cobalt catalyst during model experiments (250°C, P_{H_2O} = 5.5 bar, P_{He} = 4.5 bar) (model experiments either involved neither hydrogen nor carbon monoxide being present, or significantly higher P_{H_2O}/P_{H_2} ratios than what would be present under normal FTS conditions). After water exposure under model conditions, pulse adsorption of hydrogen indicated no change in the metal surface area and therefore no sintering. It was found that the promoted catalyst underwent oxidation more easily than did the unpromoted one. It was suggested that because the promoted catalyst crystallites were smaller, they may have been more readily oxidised. During FTS experiments, at a water addition P_{H_2O}/P_{H_2} ratio of 0.38 (simulated conversion of 36%), Storsæter *et al.* (2005) observed cobalt structural changes, and the formation of cobalt aluminate species was confirmed by EXAFS. Catalysts with smaller cobalt crystallites were found, by others (Jacobs *et al.*, 2002), to be more sensitive to deactivation by water. It was determined that size has an influence on the level of deactivation under both FTS and model (H_2O only) conditions.

Saib *et al.* (2006a) synthesised cobalt crystallites of sizes 4 nm (by precipitation), 13 nm and 28 nm (the latter two by impregnation) on silica supports. They also employed various characterisation techniques, including HRTEM, XANES, TPR, and dynamic *in-situ* XRD (catalyst samples periodically removed from the reactor and analysed) to test the catalysts under model conditions (25-300°C, P_{H_2O} = 0.04-0.3 bar, 2-3h exposure time) for oxidation in the presence of only water and helium. They found that the crystallites were made up of a mixture of face-centred cubic (fcc) and hexagonal closed-packed (hcp) crystal phases, with the fcc content increasing as the crystallite size decreased. These phase mixtures may have resulted from the presence of stacking faults in cobalt crystallites which can arise from sliding of cobalt layers. This sliding of the layers has a low activation energy requirement of 14 kJ/mol Co, which can be readily supplied at reduction temperatures (Saib *et al*., 2006a).

The catalysts were tested at water partial pressures of 0.04 bar (the balance being helium). The large crystallites underwent 2% oxidation at 300°C, reaching 5% oxidation for a water partial pressure of 0.3 bar at 100°C; the intermediate-size crystallites reached an oxidation of 30% at 300°C, and it appeared that the small crystallites underwent no oxidation up to 400°C for water partial pressures up to 0.3 bar. It was acknowledged that oxidation under these conditions (only water and an inert gas) was expected from bulk thermodynamics, as was shown by van Berge *et al.* (2000). Saib *et al.* proposed that the larger crystallites were more stable towards oxidation because they are well-faceted and have fewer defects in the crystallite stacking. The crystallites of size 13 nm underwent substantial oxidation, driven by the increased curvature of the crystallites, which increased the number of defects (Saib *et al*., 2006a). Dissociation of water is preferred at defective sites which increase the extent of oxidation. From a dispersion relationship, it was determined that the 13 nm crystallites had three to four layers of oxidation of cobalt oxide. It was indicated that silica can migrate under reduction temperatures and, as was revealed by high-resolution transmission electron microscopy (HRTEM), a layer of silica shielded the small (4 nm) crystallites from oxidation. Thus no information regarding their susceptibility towards oxidation was discovered. The model experiments conducted by Hilmen *et al.* (1999) and Saib *et al.* (2006a) provided insight into cobalt's tendency to be oxidised under conditions which thermodynamically favour oxidation, but which require P_{H_2O}/P_{H_2} ratios (if hydrogen was even present) that are unrealistically high under normal FTS conditions.

Saib *et al.* (2006b) employed platinum-promoted, alumina-supported cobalt catalysts predominantly 6 nm in diameter (XANES) in FTS (230°C, 20 bar, H_2/CO = 2, 50-70% conversion) in a 100 bbl/day slurry bubble column reactor. It was noticed that catalytic activity declined by about 40% within the first 30-40 days, after which it began to level (see figure 2.2). The cobalt phase in the fresh catalyst consisted of about 53 wt % Co, with the remainder being CoO and possibly $CoAl_2O_4$ (Saib *et al*., 2006b). After the first 8 days of operation, the catalyst was gradually reduced to consist of about 85 wt % Co. The decline in catalytic activity was attributed to sintering, which resulted in the formation of larger crystallites which are more easily reducible than are smaller crystallites. Saib *et al.* speculated that these larger crystallites were reduced over the first 80 days, with the first 30 days including both sintering and reduction. This speculation was supported by the observation that the *in-situ* reduction did not result in an increased activity, as crystallites larger than 6 nm under these

conditions were expected to exhibit a lower overall activity than those of 6 nm in diameter. Saib *et al.* discarded oxidation as a major deactivation mechanism for $Co/Pt/Al_2O_3$ catalysts with Co crystallites of predominantly 6 nm during FTS. They noted that other deactivation mechanisms might have been present, including sintering, as mentioned, as well as carbon deposition and surface reconstruction.

van Steen *et al.* (2005) conducted a thermodynamic analysis for the stability of cobalt oxide under typical Fischer-Tropsch synthesis conditions for a temperature range of 220-250°C. They assumed that the crystallite shapes were spherical, had smooth surfaces and were free from packing faults and defects. They determined for bulk cobalt that oxidation would occur only for a P_{H_2O}/P_{H_2} ratio of at least 128 at 220°C (corresponding to a simulated conversion of 99.6%). Therefore it was determined that bulk cobalt metal will not oxidise under these conditions. The following equations indicate the general reactions that occur during FTS (van Steen *et al.*, 2005), in formation of the CH_2 "monomer".

$$CO + H_2 + Co \leftrightarrow CoO + CH_2 \quad (2.1)$$

$$CoO + H_2 \leftrightarrow Co + H_2O \quad (2.2)$$

The cobalt catalyst will be deactivated if the regeneration of the cobalt site (equation 2.2) is not thermodynamically feasible. That is, if cobalt oxide and hydrogen are energetically favoured over metallic cobalt and water, the catalyst will remain deactivated, i.e. as CoO (van Steen *et al.*, 2005).

The stability of nano-crystallites is different from that of bulk-phase metal. As the size of the crystallites decreases, the contribution from the surface energy becomes more significant. Cobalt crystallites with a diameter below 100 nm were considered to be thermodynamically stable as fcc cobalt (van Steen *et al.*, 2005). Other phases that are present would be in a form of metastable state, as may have been the case with the crystallites synthesised by Saib *et al.* (2006a) where the hcp phase was found to be present. Supported cobalt catalysts usually contain crystallites that are smaller than 100 nm in diameter, as indicated by Hilmen *et al.* (1999), Saib *et al.* (2006a, 2006b), Storsæter *et al.* (2005) and van de Loosdrecht *et al.* (2007), *inter alia*.

At 220°C, it was found that fcc cobalt crystallites of diameter smaller than 4.4 nm are expected to be unstable and will be present as CoO for typical FTS P_{H_2O}/P_{H_2} ratios (van Steen *et al.*, 2005). The size below which CoO will be present for fcc cobalt crystallites was later revised to be approximately 2.6 nm (Swart, 2008).

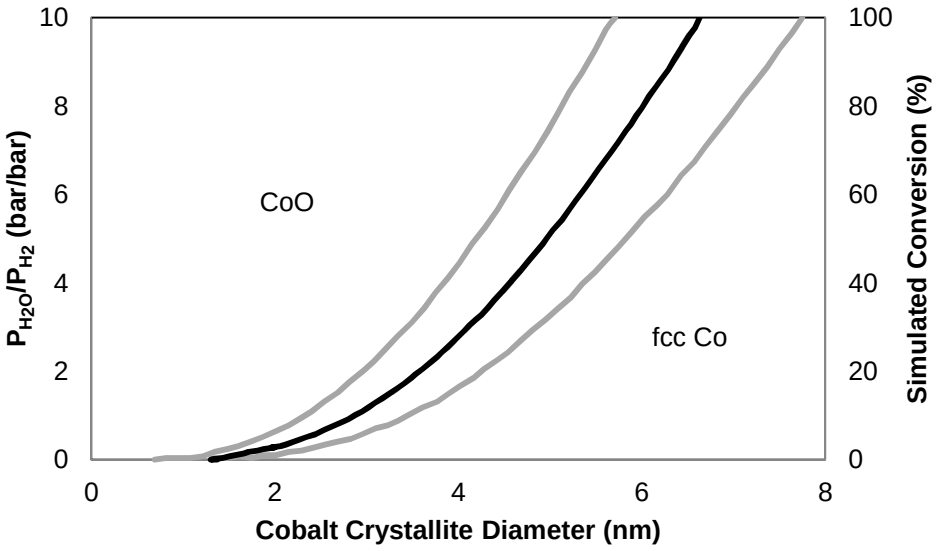

Figure 2.7: Stability region of spherical fcc and CoO crystallites in P_{H_2O}/P_{H_2} atmospheres at 220°C as a function of diameter of a spherical metal Co crystallite. Grey lines represent a surface-energy margin of 10%. An increase of 14% in the surface energy corresponds to hcp which would further destabilise the metallic phase (van Steen *et al.*, 2005). Correction by Swart (2008) not shown. Second vertical axis relates P_{H_2O}/P_{H_2} ratios directly to simulated conversion.

For the hcp phase, van Steen *et al.* (2005) found that the diameter below which cobalt oxide is formed was 5 nm under FTS conditions. The stability of the hcp cobalt crystallites was determined to increase with temperature, but only by approximately 0.1 nm for 250°C.

As industrial catalysts are made up of a distribution of sizes, a number of the crystallites which are small may not be regenerated, and those which are in intimate contact with the support may form cobalt-support species (van Steen *et al.*, 2005) such as cobalt aluminate, silicate or titanate, which are thermodynamically more stable. Storsæter *et al.* (2005) found aluminate species to be present and Hilmen *et al.* (1999) found that phases that interacted strongly with the alumina were formed. It was suggested that cobalt catalysts may also be deactivated by the formation of an oxide shell surrounding a metallic core. However, this is thermodynamically unfavourable (van Steen *et al.*, 2005).

van de Loosdrecht *et al.* (2007) employed a 100 bbl/day reactor for FTS (230°C, 4-6 bar, $P_{H_2}/P_{CO} = 2$) and characterised their alumina-supported, platinum-promoted, cobalt catalysts, with an average crystallite size of 6 nm (TEM), by pseudo *in-situ* XRD, XANES and magnetic measurements. The freshly-reduced catalyst was found to contain CoO (47 wt % by XANES) which was possibly made up of unreduced, small CoO crystals (Saib *et al*., 2006a), in addition to metallic Co. They periodically extracted catalyst samples from the reactor and kept them in an inert environment so that no further changes would occur between extraction and characterisation. The cobalt oxide phase was found to be reduced to metallic cobalt during reaction for the first 10 days and then remain in the metallic phase, even though the intrinsic activity was found to decrease for about 40 days, after which it appeared to approach a constant value (figure 2.8). Speculations were made as to the reason for the reduction of the catalyst during reaction. van de Loosdrecht *et al.* (2007) proposed that the hydrogen partial

pressure was high enough to reduce the catalyst, the presence of CO may affect water-cobalt interactions (Bertole *et al.*, 2002), or that sintering could have occurred, resulting in larger, easily-reducible cobalt crystallites while also explaining the observed decrease in intrinsic activity (van de Loosdrecht *et al*., 2007).

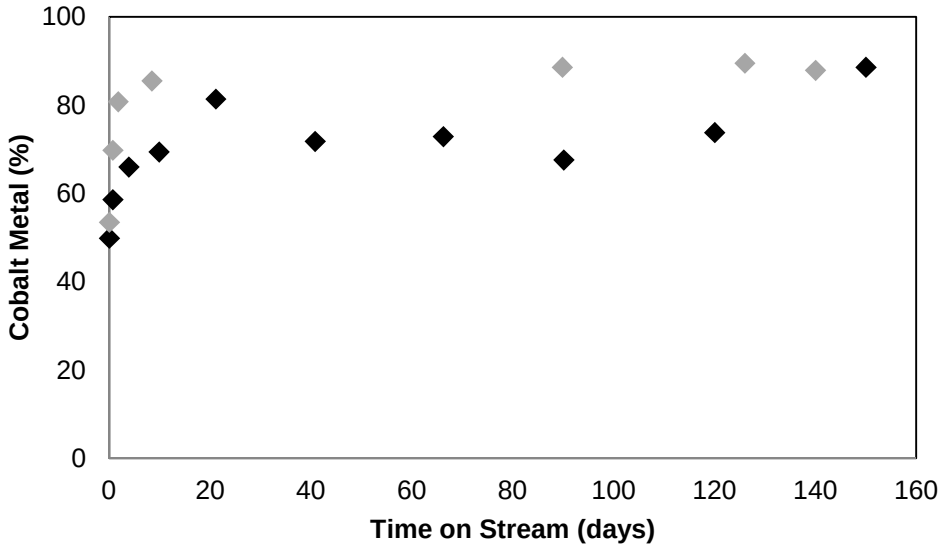

Figure 2.8: Fraction of cobalt metal in spent cobalt catalyst samples taken from the FTS run, as a function of time online, as determined by magnetic measurements (◆) and XANES (◆) (van de Loosdrecht *et al.*, 2007).

Van de Loosdrecht *et al.* (2007) concluded from their findings that oxidation could not be a deactivation mechanism. Bezemer *et al*. (2010) also concluded that oxidation is not a deactivation mechanism under industrial operation, even for smaller cobalt crystallites due to the low P_{H_2O}/P_{H_2} ratios under FTS conditions. Parameters that may affect the deactivation of cobalt in the presence of water include different support materials (Storsæter *et al.*, 2005), promoters, preparation methods, process conditions and apparent differences due to inconsistent characterisation techniques (van de Loosdrecht *et al.*, 2007). It was noted that water could facilitate other deactivation mechanisms such as surface reconstruction, support migration, carbon deposition, the oxidation of existing CoO to cobalt-support compounds, or the oxidation of metallic crystallite structural defects (sites) which may previously have been responsible for enhanced activity. These may occur to differing extents, depending on the different conditions of the various systems employed for this kind of work. Indirect techniques used to monitor cobalt's oxidation states may lead to an overestimation of the degree of oxidation and thus its influence on deactivation (van de Loosdrecht *et al.*, 2007).

Oxidation may occur for a number of the cobalt crystallites present yet not be adequately quantified because there is a size distribution of crystallites, even though oxidation may not be expected for the reported average size (i.e. the smallest crystallites may be oxidised but a fraction of the average-sized crystallites would be reported as being oxidised since the extent to which the different-sized crystallites are oxidised is not quantified). Values from various research groups that were compared by van de Loosdrecht *et al.* (2007) included only those where the characterisation technique employed

could directly determine the oxidation state of cobalt (i.e. XPS, XANES, EXAFS, TEM, XRD and magnetic measurements). These results seemed to agree on the range of P_{H_2O}/P_{H_2} ratios and crystallite sizes where oxidation of cobalt crystallites would occur, in accordance with the aforementioned experimental findings. However, all of these techniques were performed *ex situ*, and, as a result, the oxidation state of cobalt could be identified only after the studied catalyst was extracted and passivated. Oxidation can and often does occur even during "successful" passivation methods (see section 2.7.1). This range was in agreement with thermodynamics (van Steen *et al.*, 2005) and appeared to be independent of the support identity (silica and alumina were compared). However, as support geometries and chemical properties differ and affect the crystallite size due to different pore sizes, surface areas and cobalt-support interactions, it must be noted that there may be important differences with silica, alumina and titania (Lögdberg *et al*., 2011; Storsæter *et al*., 2005). Lögdberg *et al*. (2011) studied γ-alumina-supported cobalt catalysts under FTS conditions (210°C, 20 bar, H_2/CO = 2.1) and attributed the different effects on reaction rate to different kinetic effects in the presence of an increased water partial pressure, rather than to deactivation.

2.6.2 Selectivity

Schulz *et al.* (1997) performed experiments with a Co-ZrO_2-Ru-Aerosil catalyst under Fischer-Tropsch conditions (190°C, 10-17 bar, H_2/CO = 2). They co-fed water with the feed, while maintaining the partial pressures of H_2 and CO at approximately 6 bar and 3 bar, respectively. The feed water partial pressures were varied between 1 bar and 8.5 bar. The rate of CO consumption was found to remain approximately constant with increasing water partial pressure. Methane selectivity decreased with increasing water partial pressure while C_{5+} selectivity increased. The methane selectivity is coupled with the C_{5+} selectivity, in that the propagation of the C_1 species (where C_{5+} selectivity increases) is favoured over hydrogenation to methane (Storsæter *et al.*, 2005). They considered that the effect of increased water partial pressure on C_{5+} and methane selectivities was due to a change in the surface kinetics. An increased water partial pressure was found to increase chain-growth probability for products with carbon numbers up to C_{16} (Schulz *et al.*, 1997). Olefin selectivity also increased. Schulz *et al*. concluded that secondary hydrogenation is inhibited at high water concentrations. Iglesia (1997) also found that secondary hydrogenation of primary olefins to paraffins is restricted in the presence of water. Storsæter *et al.* (2005) suggested that this effect may contribute to increased C_{5+} selectivity, stating that more olefins are available for insertion and subsequent chain growth at increased water concentrations.

Schulz *et al.* (1997) observed an increase in primary olefin content with increased water partial pressure. They noted that water inhibited secondary olefin isomerisation by double-bond shift, reducing the content of secondary olefins produced. It was concluded that water restricted most secondary olefin reactions. It has been proposed that water assists in CO dissociation and thus its reactivity (Bertole *et al.*, 2002) and Schulz *et al*. noted that water may influence elemental reaction steps. Storsæter *et al.* (2005) discussed the transport of H_2 and CO to active surface sites and how it is modified by water, which may in turn affect the chain termination mechanism. Upon replacement of

the feed water with argon, the original selectivities were obtained, indicating that the effects of water on selectivity were reversible (Schulz *et al.*, 1997).

Lögdberg *et al*. (2011) studied Re-promoted γ-Al_2O_3-, α-Al_2O_3- and TiO_2-supported cobalt catalysts under FTS conditions (210°C, 20 bar, H_2/CO = 2.1). These catalysts were found also to contain B, Na and Cl ions, generally in larger fractions than that in which the Re was present. Water addition during FTS reaction runs resulted in an increased space-time yield of hydrocarbons for catalysts supported on the wider-pored α-Al_2O_3 and TiO_2, while the space-time yield of hydrocarbons decreased upon water addition for the catalyst supported by the narrower-pored γ-Al_2O_3. No conclusive comments could be drawn due to the observed rapid and extensive deactivation of the catalysts. In a subsequent FTS experiment performed with the γ-Al_2O_3-supported catalyst, water was added to the feed with intermediate periods where no water was added. During the water-addition periods, the space-time yield of hydrocarbons increased, while space-time yield of methane decreased. During the periods where no water was co-fed, the opposite trends were observed. It was considered that the addition of water changed the surface kinetics of CO hydrogenation, and mass-transfer limitations were ruled out. Lögdberg *et al*. claimed that the addition of co-fed water enhanced the activity of sites active for FTS and that "pure methanation" sites developed upon exposure to higher water concentrations. Water addition to the Co/γ-Al_2O_3 catalyst resulted in increased conversion and increased C_{5+} selectivity, and, correspondingly, decreased methane selectivity since the production of C_{2+} products reduces the number of CH_2 "monomers" that can be hydrogenated to methane.

In conclusion, higher water concentrations (i.e. higher conversions) result in favourable product selectivity in that methane selectivity decreases and C_{5+} selectivity increases. In order to understand these effects and deactivation mechanisms that may be enhanced by water, appropriate research techniques must to be employed. As a result, perhaps an optimum range, for a particular set of operating conditions, of both crystallite sizes and water concentrations can be established.

2.7 Understanding the Performance of Cobalt Catalysts under FTS Conditions

The extent of understanding of cobalt catalysts under FTS conditions influences the industrial operation and its economic feasibility. Analysing cobalt catalysts and their changes requires the right equipment and methods, and progress is constantly being made in this area. New techniques are discussed here.

2.7.1 Analysis of Spent Cobalt Catalysts

The analysis of spent cobalt catalysts can be performed *ex situ*, with steps taken to prevent further catalysts changes. Some of these preventative measures include, for example, blanketing spent catalysts in a nitrogen atmosphere before analysing with XANES (van de Loosdrecht *et al.*, 2007); removing wax with deoxygenated tetrahydrofuran in an argon atmosphere, followed by vacuum

drying and catalyst crushing, before being analysed with XPS (Moodley *et al.*, 2009); or pelletising wax-coated spent catalysts in a low-O_2 (<1 ppm) environment and sealing in Kapton tape, before analysing with XANES (Saib *et al.*, 2006). Generally, procedures are implemented which usually include sampling spent catalysts after a certain time on stream, removal of wax, keeping the catalysts in an inert atmosphere (sometimes the wax itself) that prevents further changes from occurring due to oxidation in air, and then characterising them. During the time taken between sampling and characterisation, the catalyst may have changed to some extent, and these methods can be expensive and time-consuming (Shroff & Datye, 1996). Mansker *et al*. (1999) studied iron catalysts, which exist in a number of carbide phases, under FTS conditions. XRD is a useful instrument for distinguishing between these different phases. However, upon extraction and passivation of the spent catalysts, they found that oxidation had occurred, either during the extraction process or upon subsequent exposure to air, thus compromising analysis to some extent. Shroff and Datye (1996) describe the problems that arise in spent catalysts if correct passivation methods are not employed, and how, even upon the implementation of an appropriate passivation method, the spent catalyst is still susceptible to oxidation. In fact, the extent of oxidation, as determined by HRTEM, was used to determine whether a passivation procedure was considered "successful" (Shroff & Datye, 1996).

A superior alternative to analysing spent catalysts after exposure to reaction conditions is to analyse them *in situ*. *In-situ* characterisation allows the changes to be observed under reaction conditions without risking the occurrence of further changes. Rønning *et al.* (2010) noted that *in-situ* characterisation techniques must be able to operate at reaction conditions, with a need for transient phenomena involved in catalyst deactivation to be adequately tracked. However, to date very little *in-situ* characterisation of FT catalysts has been reported.

2.7.2 *In-Situ* XRD Cells

Commercial *in-situ* XRD cells have been in existence for a number of years. However, implementing a commercially-available *in-situ* reaction unit for laboratory scale XRD instruments, such as the XRK 900 (Anton Paar, Austria), poses a number of problems. The first is that its large volume (up to 500 cm^3) houses dead volume, where unobservable reaction conditions are present. In these zones, plug-flow conditions usually do not exist and this may introduce unknown parameters into the system with regard to predictability and characterisation. Moreover, even though this cell allows flow through the catalyst bed, the flow pattern through the catalyst does not exhibit plug-flow behaviour and the catalyst bed temperature is not directly measured, thus affecting the quality of performance data obtained using this cell. As a result, kinetic analysis is difficult, if not impossible. Another problem, with direct regard to FTS, is that commercial cells are often manufactured with beryllium in their windows, an element which is suitable for X-ray analyses. However, it can react with steam, forming beryllium oxide and hydrogen (Druyts & van Iseghem, 2001). Steam is produced in FTS and is often co-fed in experimental studies of water effects on FT catalysts (Storsæter *et al.*, 2005). Kapton film (DuPont), which does not react with water, is also used in commercial cell windows, but oxidation of the windows is nonetheless regularly observed. Steam can also lead to corrosion of heating elements

used inside such cells. Furthermore, the Anton Paar XRK 900 is limited in its operating conditions to 900°C and 10 bar, with the pressure being below that of many catalytic applications.

Various research groups (Jensen *et al*., 2010; Karaca *et al*., 2009; Rønning *et al*., 2010; Grunwaldt *et al*., 2004; Li *et al*., 2001; Moggridge *et al*., 1992; Clausen *et al*., 1991) have developed *in-situ* XRD cells. Clausen *et al*. (1991) developed a cell with a capillary tube of quartz or glass as the reaction vessel that was heated using hot air blown around it. They noted that the capillary tubes could be operated at conditions up to 450°C and 50 bar, conditions suitable for industrially-relevant FTS and with the pressure rating exceeding that of the Anton Paar XRK 900. Temperature-uniformity was maintained by the presence of an enclosure of Kapton film around the tube and the reaction zone temperature was controlled via a thermocouple positioned 1 mm below the tube (Clausen *et al*., 1991). While their design facilitated online kinetic analysis, the position of the thermocouple (outside the catalyst bed and outside the tube) resulted in inaccurate temperature control. The heating method, while resulting in good temperature uniformity, and the general setup were such that the cell could not easily be mounted to and detached from a commercial X-ray diffractometer, reducing its potential to be widely used.

Moggridge *et al*. (1992) developed an *in-situ* XRD cell heated by external ovens. The temperature of the reaction zone was controlled via an internal thermocouple, positioned after the catalyst bed. They performed their experiments at 700°C and 1 bar, lower than the maxima of which the XRK 900 (Anton Paar) is capable. Moggridge *et al*. noted that the steel thermocouple sheath may have affected kinetic analysis results, such that they stated that the trends in their results were qualitatively but not quantitatively accurate. For a reaction such as FTS, with a complex product spectrum, accurate kinetic analysis is essential. It appeared, from a schematic (Moggridge *et al*., 1992), that their cell was not designed to exhibit plug-flow conditions, furthering the lack of integrity of their kinetic results. The cell design in this case, though not described in as much detail as that of Clausen *et al*. (1991), was also such that it could not be mounted to a commercial X-ray diffractometer.

Other designs (Rønning *et al*., 2010; Karaca *et al*., 2009) employed quartz capillary tubes as the reaction vessel and used hot-air blowers to heat the reaction zone, and Karaca *et al*. (2009) used high-temperature epoxy glue to seal the capillary tube from gas leaks. Their operating conditions were 210°C and 20 bar. Rønning *et al*., 2010 used a glass capillary tube as the reaction vessel and performed FTS at 210°C and 18 bar. Jensen *et al*. (2010) developed a cell that employed a sapphire capillary tube as the reaction vessel, heated by a custom-built heating element and sealed using Vespel ferrules. They found the capillary's burst pressure at room temperature to be 900 bar, and it to be suitable for operation temperatures (at lower pressures) up to 1000°C. The capillary's structural integrity depends on its quality, on it being free from crystal and surface defects (Jensen *et al*., 2010). The cell's design, like the other two aforementioned ones, failed to permit mounting to a commercial X-ray diffractometer. From the developments by these research groups, it can be concluded that quartz, glass and sapphire capillary tubes have the structural capabilities to operate soundly at industrially-relevant reaction conditions which exceed those of which the XRK 900 (Anton Paar) is capable. Unlike the cells developed by these research groups, however, it is essential that a useful tool

such as an *in-situ* XRD cell be easily mountable to standard X-ray diffractometers, making its benefits transferrable, and that the methods via which it is heated and sealed to prevent gas leaks make it reusable, with minimal wastage of parts.

In order to eliminate the problems associated with commercial cells and those developed by the aforementioned research groups, an *in-situ* XRD cell that has no dead volume and is not reactive with water, while at the same time allows accurate kinetic analysis with direct temperature measurement and is suitable for X-rays, has to be developed. It must also be mountable to any commercial X-ray diffractometer so that, through ease of operation, its benefits are easily transferrable. The development of such a cell and its testing with cobalt model catalysts under FTS reaction conditions is the subject of this thesis. The following section details the synthesis of the catalysts, the development of the cell and the experiments conducted.

3 Materials and Methods

In conducting Fischer-Tropsch synthesis experiments while making use of *in-situ* X-ray diffraction, it is important that model catalysts are used so that size and water effects, with respect to catalyst composition, activity and selectivity, can be attributed to specific physical characteristics. In this section, the methods used for catalyst synthesis, *ex-situ* characterisation (via X-ray diffraction and transmission electron microscopy) and atomic absorption spectroscopy are described. The development of the *in-situ* XRD cell and the experiments performed using it are discussed. These experiments include *in-situ* temperature-programmed reduction and FTS. Finally, the details of the kinetic analysis for activity and product selectivity are also recorded.

3.1 Catalyst Synthesis and *Ex-Situ* Characterisation

3.1.1 Catalyst Preparation by Microemulsion

Two supported cobalt catalysts, A and B, were synthesised by employing a reverse micelle technique. A reverse micelle is a water droplet within an oil phase, with a surfactant interface. It is a thermodynamically stable mixture, dependent on temperature and composition (Fischer *et al.*, 2011). The catalyst preparation followed a method developed by Fischer (2011). In this method the water phase contains dissolved cobalt nitrate, and precipitation of cobalt within the constraints of the nano-sized reverse micelles is achieved via addition of an ammonium hydroxide solution. The obtained nano-crystallites (after calcination) are then deposited onto an alumina support. Two distinct crystallite sizes were prepared in this study via variation of the composition of the respective reverse micelle systems.

The support employed was γ-alumina (S_{BET} = 162 m^2/g, V_{pore} = 0.47 cm^3/g, d_{pore} = 11.5 nm, $d_{particle}$ = 150-200 μm; Puralox/Catalox SCCa 5-150 Series (Batch 9574), Sasol, Germany). An aqueous cobalt nitrate hexahydrate (Sigma-Aldrich) solution, n-hexane (Kimix, RSA), and the non-ionic surfactant Berol 050 (pentaethylene glycol dodecyl ether, or PEGDE, AkzoNobel) constituted the microemulsions in which the cobalt crystallites were formed. All steps were conducted at room temperature, unless otherwise stated.

The hexane and surfactant were mixed together and stirred for 1 hour using a magnetic stirrer. The stirring speed was 300 RPM in all the steps where stirring was performed. Aqueous cobalt nitrate solution was then added drop-wise at a rate of about 20-30 ml/min to the organic phase while stirring and the mixture was subsequently stirred for 2 hours, after which it was left to equilibrate for 12 hours (for the composition of the two reverse micelle solutions used to obtain the two catalyst precursors, see table 3.1). This solution had a clear, pink appearance.

Table 3.1: Reverse micelle compositions for the catalyst precursors studied in this work.

	Mass (g)				Ammonium	ω^a
Catalyst	**Hexane**	**Berol 050**	**Water**	**$Co(NO_3)_2 \cdot 6H_2O$**	**Hydroxide (ml)**	
A	999.90	136.65	52.76	5.12	5.40	0.400
B	2000.01	273.59	54.24	1.32	1.35	0.200

[a] Molar water-to-surfactant ratio

Aqueous ammonium hydroxide solution (25 wt % in water, Sigma-Aldrich) was added drop-wise at a rate of about 3-6 ml/min, at the correct stoichiometric molar ratio of cobalt nitrate ($2NH_4OH$: $Co(NO_3)_2$), and the mixture was stirred for 30 minutes. The solution changed in colour from pink to green, while remaining macroscopically homogeneous. Ammonium hydroxide causes the precipitation of $Co(OH)_2$ within the reverse micelles, according to equation 3.1.

$$Co(NO_3)_2 + 2NH_4OH \rightarrow Co(OH)_2 + 2NH_4NO_3 \qquad (3.1)$$

Acetone (500 ml) was then added drop-wise to the solution at a rate of about 8 ml/min, while stirring. Acetone collapses the reverse micelles, freeing the precipitated $Co(OH)_2$ particles, which are amorphous (Fischer, 2011). After settling for 12 hours, the clear phase was decanted and 700 ml acetone was added, in a process where the surfactant is washed away. Decanting the clear phase and washing with acetone was repeated a further five times, with 12 hours of settling time allowed between adding the acetone and decanting. When smaller crystallites were being synthesised (catalyst B), the latter washing steps sometimes required longer settling times (24-48 hours), with the clarity of solution indicating the state of settling.

The clear phase was finally decanted and the remaining liquid was boiled off on a hot plate at 50°C, with hot air blown over it. The partially-dried particles were then ground using a pestle and mortar, before being thoroughly dried in an oven at 130°C for 12 hours. The $Co(OH)_2$ particles were again ground using a pestle and mortar. Calcination in air was performed in an oven that was heated up to 200°C over 2 hours, and then held at 200°C for 5 hours. The higher temperature dehydrates the amorphous $Co(OH)_2$, forming crystalline Co_3O_4, according to equation 3.2.

$$3Co(OH)_2 + ½\ O_2 \rightarrow Co_3O_4 + 3H_2O \qquad (3.2)$$

The Co_3O_4 crystallites were added to a round-bottom flask with 30 ml deionised water. The flask was placed into an ultrasonic bath for 90 minutes to suspend the particles. The alumina was added to the suspension, with the support being present in the right quantity to achieve a cobalt loading between 5-10 wt %. The new mixture was placed into a rotary evaporator operating at 80°C and 0.2 bar for 3 hours. The resultant alumina-supported Co_3O_4 was reduced to metallic cobalt in the reaction cell, in the presence of hydrogen, according to equation 3.3.

$$Co_3O_4 + 4H_2 \rightarrow 3Co + 4H_2O \qquad (3.3)$$

3.1.2 X-Ray Powder Diffraction and Rietveld Refinement

A Bruker AXS D8 Advance X-ray laboratory diffractometer was used for all the X-ray powder diffraction in this work. The diffractometer has a Co source ($\lambda_{K\alpha 1}$ = 0.178897 nm) and a VÅNTEC position-sensitive detector. A 0.6 mm slit was in place on the X-ray source side of the instrument. The diffractometer was operated in reflection mode, using parallel beam geometry, with a voltage of 35 kV and a current of 40 mA.

In-situ scans were taken over the range of 2θ angles between 40-90°. This was done to maximise resolution while minimising the time required to perform each scan, also taking into account that all the major peaks were in this range. This simultaneously eliminated the borosilicate background contribution for angles below 40° (see figure 4.3). The average crystallite sizes were determined by Rietveld refinement of the XRD spectra in TOPAS 4.2 (Bruker AXS). This method calculates the average, volume-weighted crystallite size, with 2 nm being the lower limit for what is considered reliable, using this method. The alumina used was predominantly γ-alumina with a small portion of an unknown alumina phase, possibly θ-alumina. γ-alumina and θ-alumina structure files were used for the refinements of the small crystallite sizes. For the catalyst with the large crystallite sizes, a "peaks phase" tool was used instead of the θ-alumina structure file. This was found to yield more stable results (the calculation errors were reduced in magnitude), especially because of an overlap between the XRD spectra of fcc cobalt and the θ-alumina at a 2θ angle of 52°.

3.1.3 Transmission Electron Microscopy

TEM was performed using three microscopes: a LEO 912 Omega, operating at 120 kV, an FEI Tecnai $G^2$20 with a LaB6 filament, operating at 200 kV, and an FEI Tecnai TF20 with a Field Emission Gun, operating at 200 kV. The latter two were used to produce both TEM and HRTEM micrographs. Unsupported Co_3O_4 and supported samples were suspended in ethanol and dispersed by ultrasonication before being deposited on carbon-coated copper grids for TEM analysis. Image J, a freeware programme, was used to measure crystallite sizes from TEM micrographs, from which particle size distributions (PSD) were generated. A PSD was generated from the sizes of 300-500 crystallites. These were counted by taking the length of the crystallites, as indicated in figure 3.1.

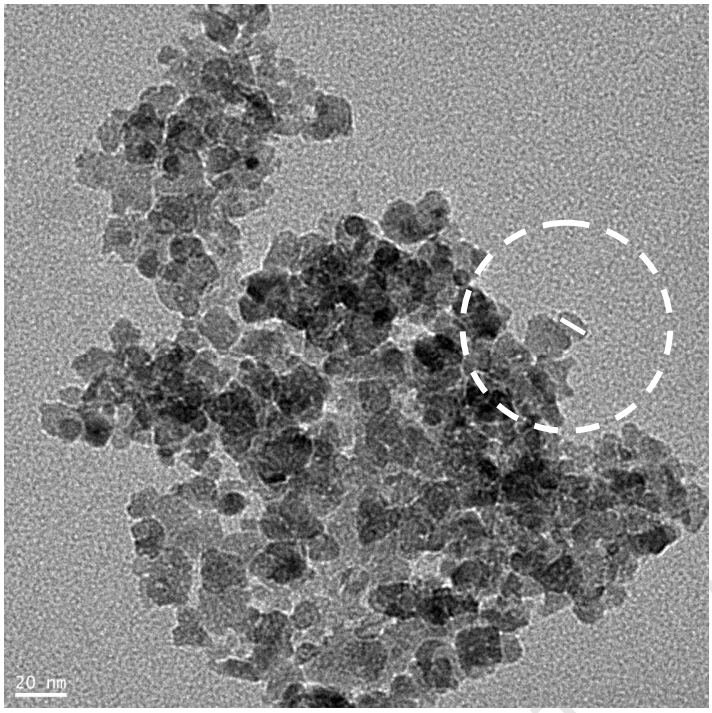

Figure 3.1: TEM image of unsupported Co_3O_4 of catalyst A. The white line within the highlighted zone indicates the way in which crystallites were measured to generate a number-based PSD from TEM.

TEM analysis yields number-based sizes. In order to compare these with XRD sizes, which are volume-based, TEM volume-based sizes were calculated from the TEM number-based sizes, according to the following equation.

$$d_{TEM,vol} = \frac{\sum n_i d_{TEM,num}^4}{\sum n_i d_{TEM,num}^3} \quad (3.4)$$

Where $d_{TEM,vol}$ is the calculated, volume-based TEM size, n_i is the number of measured crystallites of a particular size (i.e. $d_{TEM,num}$), and $d_{TEM,num}$ is the number-based TEM size, as measured from the micrographs.

3.1.4 Atomic Absorption Spectroscopy

The metallic cobalt loadings of the Al_2O_3-supported Co_3O_4 were obtained from elemental analysis, using Atomic Absorption Spectroscopy (AAS). A Varian SpectraAA 110 AAS instrument was used. Approximately 100 mg of each supported sample was digested in 10 ml of a 4:1 HCl/HF mixture. The acid concentrations for HCl and HF were 30 wt % and 40 wt %, respectively. The mixture was heated to its boiling temperature at which point 10 ml HNO_3 was added. The volume was reduced to 2 ml by boiling. 5 ml of concentrated $HClO_4$ was added and the mixture volume was again reduced to 2 ml by boiling. The cooled mixture was transferred to a volumetric flask and the volume increased to 100 ml by the addition of distilled water. The liquid was filtered using filter paper and the filtrate was analysed using AAS.

3.2 *In-Situ* XRD Cell Development

The development of an *in-situ* XRD cell was the main aim of the current study. It must be suitable for *in-situ* experiments at realistic reaction conditions (i.e. temperatures and pressures up to and above 450°C and 20 bar, respectively). The design must be such that plug-flow conditions are present and that the reaction zone temperature is measured accurately so that reliable online kinetic analysis can be performed. The reaction vessel needs to be gas-tight, which must be achieved by an appropriate, reusable set of materials. The *in-situ* XRD cell must also be designed so that it can be mounted to any commercial X-ray diffractometer or synchrotron, thereby making its benefits widely transferrable. A challenge with this last point includes the fact that laboratory-scale X-ray diffractometers have considerably lower power sources than do synchrotrons, resulting in potentially significant interference from the reaction cell itself. This must also be addressed.

3.2.1 Reactor Design and Setup

A suitable reaction cell must be able to withstand appropriate reaction conditions, as mentioned above, while also exhibiting plug-flow conditions for kinetic analysis. A glass capillary tube, in accordance with what has been found by others (see section 2.7.2), is an appropriate starting place for such a reaction vessel. Capillaries of differing dimensions and construction materials were obtained. In table 3.2 the acquired capillaries and their dimensions are listed. Concerning the capillary names, "H" refers to Hilgenberg GmbH (Germany) and "C" refers to Capillary Tube Supplies (UK), the suppliers of the correspondingly-named capillaries. Linear absorption coefficients for quartz and borosilicate have been reported as being 75.8 cm^{-1} and 71.0 cm^{-1}, respectively (Capillary Tube Supplies, 2009). This is an indication of how much the X-ray signal is affected by these materials, with a higher number indicating a greater loss in signal. Unfortunately, no information for the loss of X-ray signal through sapphire could be obtained.

Table 3.2: Tested capillaries and their dimensions. Each capillary was 75 mm in length.

Capillary Name	Construction Material	Outer Diameter (mm)	Wall Thickness (mm)
H2S	Sapphire	2	0.20
H1S	Sapphire	1	0.10
H2Q02	Quartz	2	0.20
H2Q01	Quartz	1	0.10
CQ002	Quartz	1	0.02
CQ001	Quartz	1	0.01
CB002	Borosilicate	1	0.02
CB001	Borosilicate	1	0.01

The *in-situ* XRD cell (see schematic in figure 3.2) has been designed so that it can be mounted to the Bruker AXS D8 Advance X-ray laboratory diffractometer in the same manner in which the commercial attachments are mounted. This design also allows it to be mounted to any other laboratory diffractometer. Capillary CB002 (of wall thickness 0.02 mm) was used as the reactor in this study. This material was selected over quartz due to its lower linear absorption coefficient in CuK radiation

(Capillary Tube Supplies, 2009), which is similar in wavelength to that of CoK radiation. In testing the capillaries, spectra of superior quality were obtained when using the borosilicate capillaries (see figures 4.2-4.5). Due to the crystal structure or greater presence of structural or chemical defects in borosilicate capillaries in comparison with quartz capillaries, their safe upper temperature limit is about 500°C whereas quartz capillaries can operate up to 1000°C and higher. Quartz capillaries of approximate wall thickness 0.02 mm can be operated up 50 bar and higher (Clausen *et al*., 1991). Dimension effects are significant for borosilicate capillaries and an operating pressure of 25 bar is expected to be achieved with a wall thickness of 0.02 mm. The upper operating pressure limits in both cases depend on the way in which the capillaries are manufactured and on their crystal and surface defects (Jensen *et al*., 2010). The sapphire capillaries studied were too thick so that no XRD spectra were generated. While other research groups have used sapphire capillaries (Jensen *et al*., 2010), they also used synchrotrons for their XRD work. Synchrotrons have much greater operating voltages than do laboratory-scale X-ray diffractometers. This means that the X-rays generated have sufficient energy to penetrate the thicker capillaries and generate high-quality signals. Signal quality is also a function of scan time (16.5 minutes was found to be the optimum in this study), where longer scans result in signals of higher intensities, while shorter scans better approximate real-time catalyst characterisation. Sapphire capillaries are capable of higher operating temperatures and pressures, theoretically up to 2000°C and operationally up to 900 bar (Jensen *et al*., 2010). Sapphire capillaries of wall thickness 0.02 mm are difficult to manufacture and it was not possible to obtain them for this study.

In figure 3.2 is a schematic of the first-generation *in-situ* XRD cell that was used in the current study. All the capillaries listed in table 3.2 were tested in this cell, without any changes required to do so, thus confirming its capacity to accommodate any capillary of 1 or 2 mm outer diameter. Plug-flow conditions are achieved with these dimensions (Grunwaldt *et al*., 2004) and the flow-rates used in the current study, resulting in accurate kinetic analysis, provided a suitable temperature profile exists.

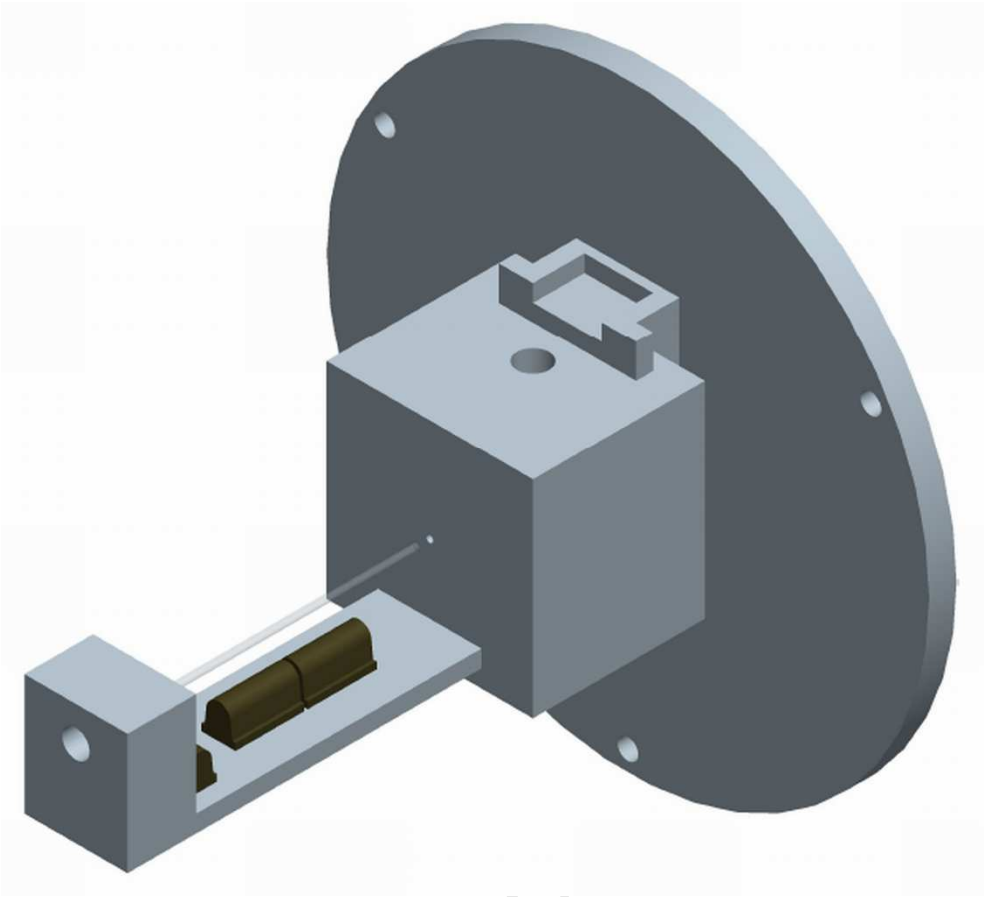

Figure 3.2: Simplified schematic of the first-generation *in-situ* XRD cell with diffractometer mounting plate, height-adjustable extension block, capillary reactor and infrared heaters (image courtesy of Marc Wüst).

Attached to the mounting is a height-adjustable feature (see figure 3.4) to ensure that the catalyst bed is at the diffractometer's level of detection. Therefore, the background signal from the capillary material can be minimised by adjusting the height. To prevent both breakage of the capillaries and inconsistent XRD signal, it was important for the design to be as rigid as possible to eliminate lateral movement.

Yttrium oxide, Y_2O_3, was used as a standard to determine the appropriate height for the cell, as well as the background contribution introduced from the capillary walls. The catalyst bed (made up of approximately 0.1-0.2 g of catalyst) was approximately 2.5 cm long and was packed on either side with silane-treated glass wool.

Heaters beneath the reaction zone of the cell maintain the operating temperature, which is controlled via an internal thermocouple. Elstein MSH infrared heaters (Elstein, Germany) 20 mm long and 10 mm wide were used, capable of heating the reaction zone to temperatures above 500°C. They were positioned in different ways, to find an optimum temperature profile. The final combination was as indicated in figure 3.2, with two placed end-to-end. A transformer (Eloff Transformers, RSA) of potential up to 12 V and current capacity up to 13 A was installed as was required by the infrared heaters. Their power output was controlled using a programmable temperature controller (Gefran 800P) (Unitemp, RSA). A heat shield was manufactured from aluminium sheeting and DuPont

Kapton film (RS Components), which does not interfere with X-rays. It was attached to the aluminium shield by magnetic strips (Technical + General Distribution, RSA). A schematic of this setup is shown in figure 3.3.

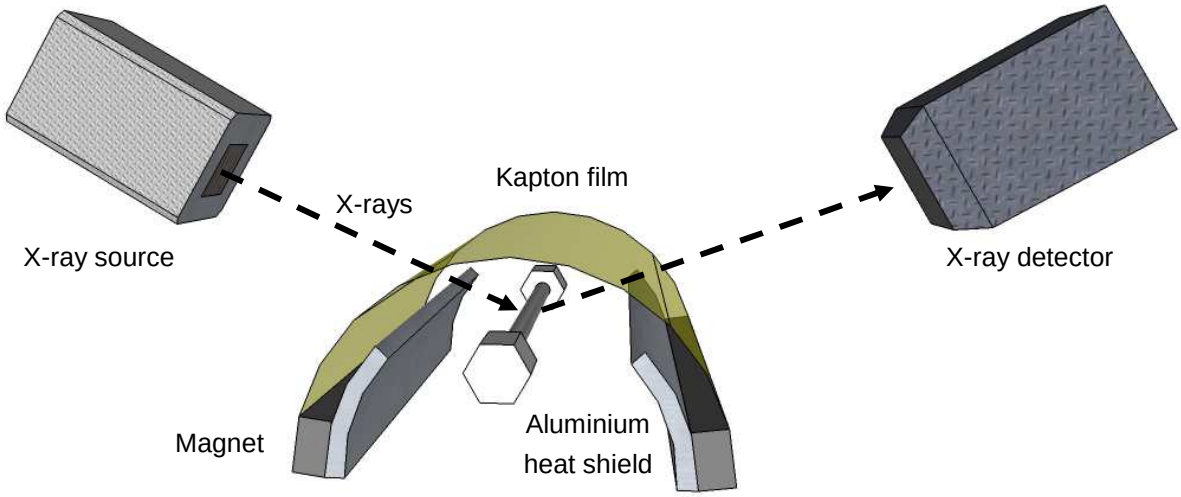

Figure 3.3: Schematic of aluminium heat shield and surrounding Kapton film. Capillary shown fitted within hexagonal Swagelok eighth-inch fittings. Note that the heat shield does not interfere with the X-ray beam path.

The heat shield and Kapton film made up an enclosure for the reaction cell and resulted in improved temperature control of the reactor (see temperature profile in figure 4.6). In addition to the reactor heating, a heating cartridge with incorporated thermocouple (not shown) was placed into the large block, on the inlet side of the reactor (see figure 3.4). This prevented water condensation during co-feeding experiments.

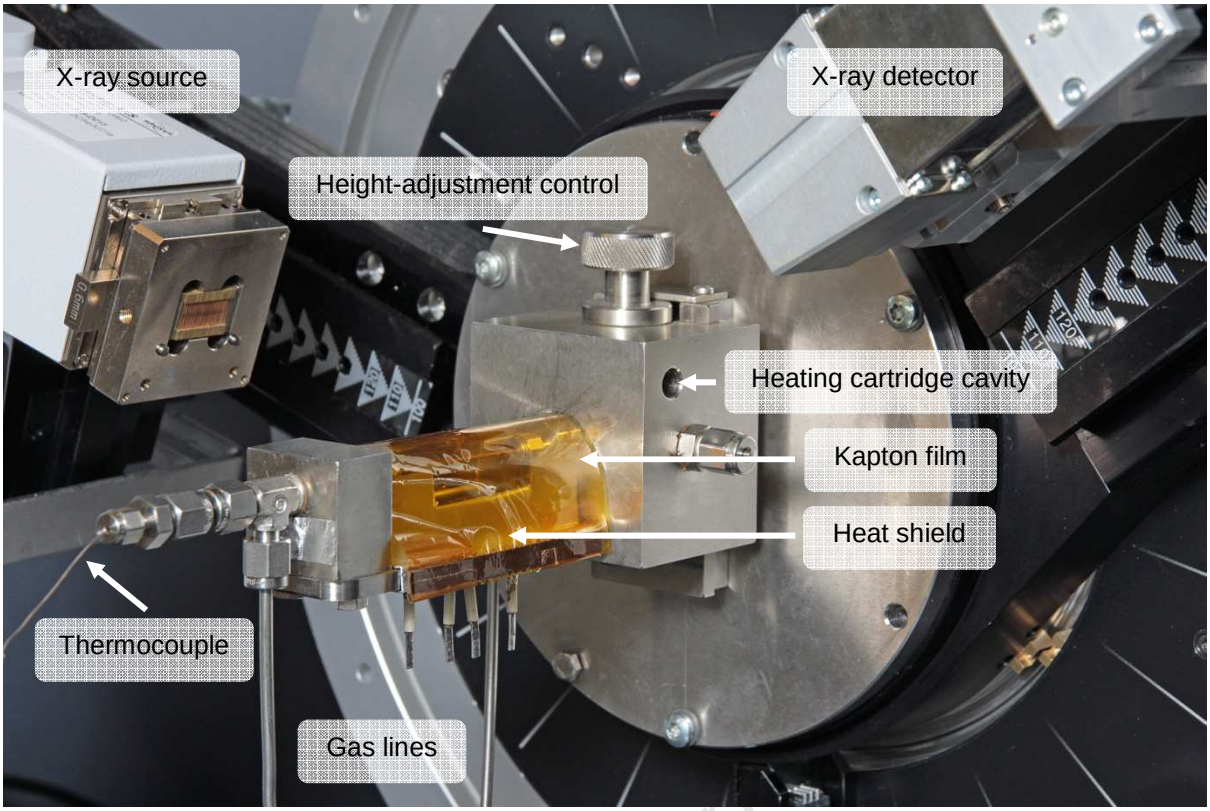

Figure 3.4: XRD capillary stage with heat shield and Kapton film. Inlet and exit lines for illustration only (real gas lines were heated and insulated). Thermocouple was supported during operation (diagram for illustration only).

The capillary was sealed to the Swagelok sixteenth-inch tube connectors by using Agilent short graphite ferrules with internal diameter 1 mm (Chemetrix, RSA), PTFE tape (Swagelok) and DuPont Kalrez 7075 O-rings with internal diameter 1.07 mm and thickness 1.27 mm (Spartan Fluid Sealing JHB, RSA). The PTFE tape was wrapped around the mounted graphite ferrule and stainless steel connector because the graphite-steel interface was not perfectly gas-tight, either due to the material or combinatorial size differences. An internal thermocouple (Temperature Controls, RSA) 0.5 mm in diameter, and with a maximum-rated operating temperature of 1000°C, was placed inside the capillary, within the catalyst bed, but outside of the X-ray beam path (approximately 1.5 cm wide).

3.2.2 Flow Sheet

The experimental flow sheet of the overall setup is presented in figure 3.5, indicating gas inlet lines with mass flow controllers, heated lines (dashed lines), saturator, reactor circuit, water knock-out drum (and water-release valve), ampoule sampling for external kinetic analysis and exit lines to online gas chromatograph and vent system. A photograph of the major components is shown in figure 3.6.

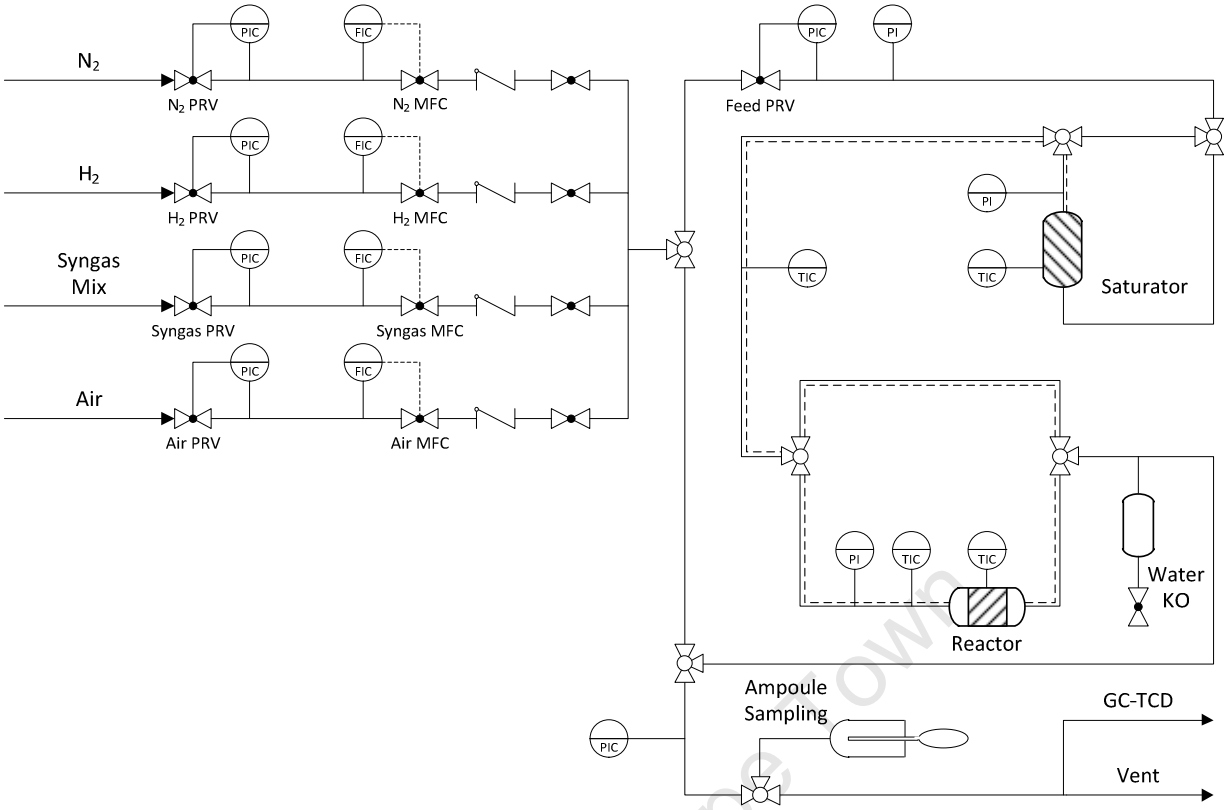

Figure 3.5: Flow sheet of reactor circuit for *in-situ* XRD FTS experiments.

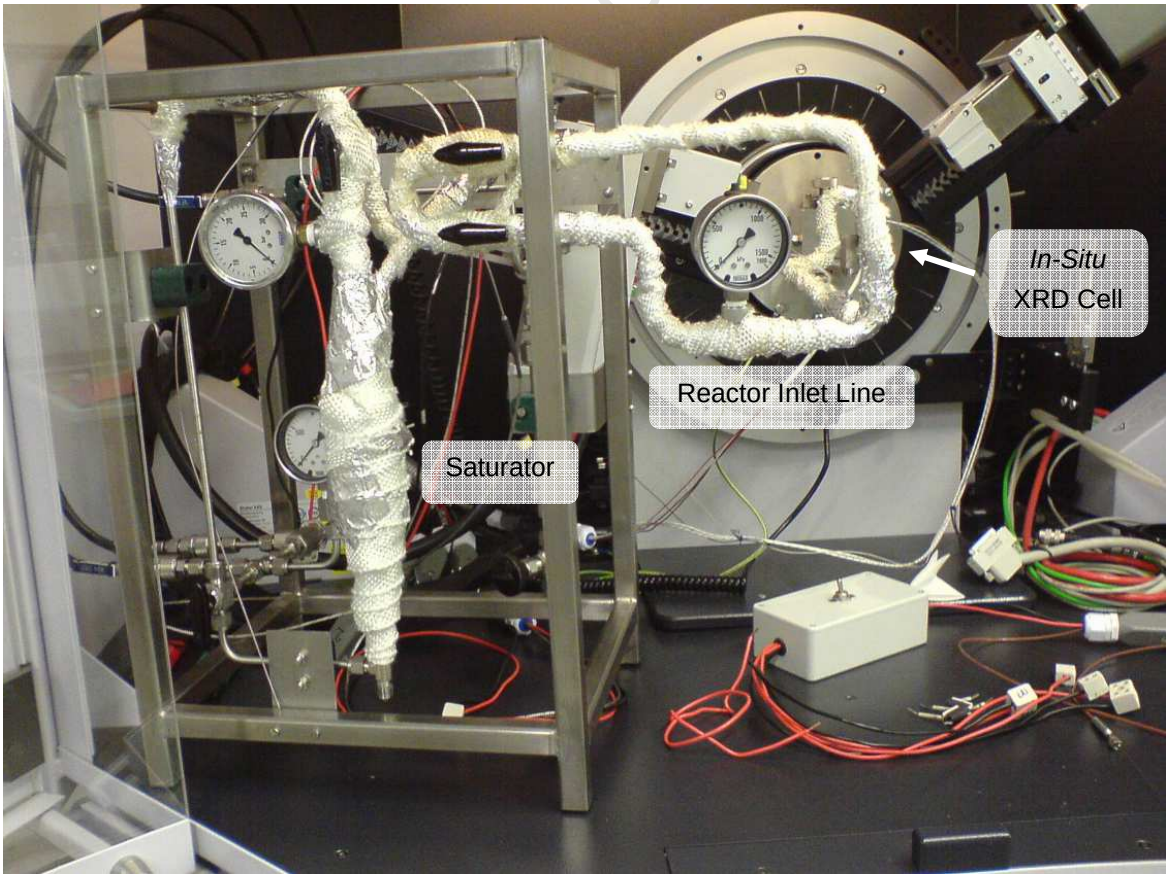

Figure 3.6: Circuit with vertically-positioned saturator and reactor inlet line, both with accompanying inline pressure gauges.

The cell has been designed with a water saturator (details in section 3.3.1) such that water can be co-fed with the syngas at various partial pressures, allowing the effects of different simulated extents of conversion to be studied. The reaction volume and chemical nature of this cell have been chosen to eliminate the problems associated with commercial *in-situ* cells (see section 2.7.2), while exhibiting plug-flow conditions. The gas feed and effluent lines were heated by heating wire and the extension block's heating cartridge, both at 200°C. The heating lines, saturator and heating cartridge were all controlled by using dedicated temperature controllers (Gefran 600) (Unitemp, RSA). The reaction zone heaters were controlled, in conjunction with the internal thermocouple, by a dedicated, programmable temperature controller (Gefran 800P).

3.3 *In-Situ* Experiments

Temperature-programmed reduction and FTS experiments were performed using the *in-situ* XRD cell. The two catalysts that were synthesised, A and B (of different crystallite sizes), were used in these experiments, and identical reduction and reaction conditions were employed for each one. Reduction was performed using temperatures up to 450°C and 1 bar(a) hydrogen, and FTS was performed at 220°C and pressures between 1-4 bar(a) (1 bar syngas; the balance was co-fed water). Kinetic analysis was performed using gas chromatography.

3.3.1 Reduction and Fischer-Tropsch Synthesis

Each catalyst was reduced *in situ* in pure hydrogen at atmospheric pressure with a space velocity of 80 $ml(NTP)\cdot min^{-1}\cdot g^{-1}$. The catalysts were reduced at 450°C, in accordance with the conditions used by Fischer *et al.* (2011). The temperature was increased from room temperature at a rate of 1°C/min, and was maintained at 450°C for 6 hours. The crystalline phase changes occurred as the catalyst was reduced in two steps, according to equations 3.5 and 3.6.

$$Co_3O_4 + H_2 \leftrightarrow 3CoO + H_2O \quad (3.5)$$

$$CoO + H_2 \leftrightarrow Co + H_2O \quad (3.6)$$

The reactor was cooled to 220°C at a rate of 2°C/min with constant hydrogen flow at the reduction flow-rate. When the reactor had cooled to the reaction temperature of 220°C, syngas, a pre-mix of 60% H_2, 30% CO and 10% Ar (Afrox, RSA), was introduced to the system. It was allowed to flow at 5 ml(NTP)/min (100% of the installed mass flow controller's capacity) through the reactor for 10 minutes to decrease the time required for CO to make up 30% of the reactant gas volume. This progress was monitored by an online gas chromatograph with thermal conductivity detectors. After this, a high syngas space velocity of 80 $ml(NTP)\cdot min^{-1}\cdot g^{-1}$ was used to ensure low conversions so that the water concentrations present could be well controlled by the designed saturator system. For each reaction condition, the syngas partial pressure was maintained at 1 bar(a). Between conditions, the system pressure was increased to the required value, with the reactor circuit open, using the back-pressure regulator, at a syngas flow-rate of 5 ml(NTP)/min, after which the saturator temperature was increased to the appropriate value to result in the desired water vapour pressure. The syngas flow-rate

was then reduced to the reaction flow-rate. Each condition was maintained for 6 hours. In table 3.3, the water partial pressure of each condition is related to the corresponding simulated conversion, as well as the system pressure for that condition and the saturator's operating temperature required to supply the feed gas with water at the required partial pressure. Simulated conversion was calculated as follows, with the water-gas shift reaction considered negligible (Dry, 1996). See table 4.2 for the catalyst masses and hydrogen and syngas flow-rates employed.

$$X_{CO} = \frac{x_{H_2O}}{x_{H_2O} + x_{CO}} \tag{3.7}$$

Where *x* is mole fraction.

Table 3.3: Water partial pressures and corresponding simulated conversions.

Water Partial Pressure (bar(g))	**Saturator Temperature (°C)**	**Simulated Conversion (%)**	**Total System Pressure (bar(a))**
0.5	82	63	1.5
1	100	77	2
2	120	87	3
3	134	91	4

The saturator, a stainless steel, double-ended cylinder with an internal volume of 75 ml (Swagelok code: 304L-HDF4-75), was positioned vertically with the gas entering from the bottom. It contained sufficient Chromosorb P (acid-washed, 60-80 Mesh) (Sigma-Aldrich) to hold approximately 40 ml of water which was used to saturate the syngas stream. The Chromosorb was secured with silane-treated glass wool above and beneath it. The saturator was heated using heating wire and its temperature was controlled via an internal thermocouple. System pressures from 1-4 bar(a) were used, with the difference between the syngas pressure and total pressure being made up by the water partial pressure. Co-feeding steam in this way, coupled with the high space velocity, allowed simulated conversions to be controlled.

XRD scans 16.5 minutes long over the 2θ range of 40 to 95° were taken continuously for the entirety of the reduction process, from heating up, holding at reduction temperature, to cooling down to reaction temperature. During FTS, scans 16.5 minutes long were taken continuously. The 2θ range was selected as all the significant peaks for the cobalt and alumina phases were between 40 and 95°. The scan time was selected so as to maximise peak intensity and minimise time during which unmonitored catalyst changes could occur. An online gas chromatograph fitted with thermal conductivity detectors was installed after the XRD and used to analyse the effluent gases with respect to Ar, CO, CO_2, H_2O, CH_4, O_2 and N_2. Reaction effluent gas was also captured using ampoules, the composition of which was analysed using an offline gas chromatograph with a flame ionisation detector, which allowed the analysis of hydrocarbons to be performed. The methane peaks were used to tie the two chromatograms together.

3.3.2 Gas Chromatography with Thermal Conductivity Detectors

Online gas chromatography was performed on the reactor effluent gases using an online Varian CP-4900 Micro-GC fitted with thermal conductivity detectors. Two columns, which used hydrogen as a carrier gas, were employed. The first, a 20 m Poraplot Q PLOT column, operated at 1.8 bar(a) column head pressure and 60°C, and the second, a 10 m Molecular Sieve 5A PLOT column, at 1.7 bar(a) and 40°C. The software programme Varian Galaxie Chromatography Data System 1.9.3.2 was used to control the gas chromatograph and to calculate peak areas of the components from the chromatograms. The chromatograph was calibrated using a sample of gas of known composition. Calibration factors were calculated, as follows, with argon as the reference gas (equation 3.8).

$$F_i = \frac{x_i A_{Ar}}{x_{Ar} A_i} \tag{3.8}$$

Where x_i is the mole fraction of component i and A_i is the integrated area of component i, calculated from the chromatogram.

The flow-rate of methane was calculated from GC-TCD analysis, as the reference/tie compound for GC-FID analysis (section 3.4.2).

$$\dot{v}_{CH_4} = \frac{A_{CH_4} F_{CH_4} \dot{v}_{Ar}}{A_{Ar}} \tag{3.9}$$

Where $\dot{v}_i$ is the volumetric flow-rate of component i.

3.4 *Ex-Situ* Catalyst Characterisation and Kinetic Analysis

3.4.1 Transmission Electron Microscopy

Spent catalysts were cooled from 220°C to 25°C in flowing N_2. At 25°C, 1% O_2 in N_2 was used to oxidise the surface of the catalysts to prevent further oxidation upon exposure to the atmosphere. They were then characterised by Transmission Electron Microscopy. This was done to potentially identify different compounds, such as Boehmite, an AlO(OH) phase, that may have formed during the water co-feeding experiments. This particular compound may not be XRD-visible either because of an overlap of its peaks with alumina or because it may be amorphous.

3.4.2 Kinetic and Product Analysis

Kinetic and product analysis were performed via offline gas chromatography on the ampoule samples taken under steady state conditions. The samples were injected manually, via syringe, into a Varian CP 3900 fitted with a flame ionisation detector (FID). The column, which used hydrogen as a carrier gas, was a non-polar CP Sil 5CB, 25 m in length and 0.15 mm in diameter (film thickness: 2 μm). The column operated at 1.38 bar(a) head pressure and the split ratio was 10. The injector and FID operated

at 225°C and 200°C, respectively. For each run, the initial column temperature was -55°C. It was held at -55°C for 1.5 minutes, after which it was heated up to 0°C at 20°C/min. It was then heated to 100°C at 14°C/min, after which it was heated to 280°C at 16°C/min. It was held at 280°C for 7.36 minutes. The software programme Varian Galaxie Chromatography Data System 1.9.3.2 was used to control the chromatograph and obtain the component areas from the chromatograms. The molar flow-rates of all components (on a carbon basis) were calculated (equation 3.10) based on the methane molar flow-rate calculated from GC-TCD calibration and analysis (equation 3.9).

$$\dot{n}_{i,c} = \frac{A_i \dot{n}_{CH_4}}{A_{CH_4}} \tag{3.10}$$

Where $\dot{n}_{i,c}$ is the molar flow-rate of component *i* on a carbon basis and A_i is the integrated area of component *i*, calculated by the GC program, from the chromatogram. Note that no correction factors were used for the hydrocarbon products, and oxygenates formation was negligible in this study.

Compounds with carbon numbers up to 7 could be detected on the column (for GC-FID chromatograms, see appendix A1). An Anderson-Schulz-Flory plot for each water partial pressure was constructed using the straight-chain products with carbon numbers 3-6 (for ASF plots, see appendix A2). To construct this plot, the natural logarithm of the ratio of the mole fraction (carbon basis) of component *i* to its carbon number, $ln\frac{x_{i,c}}{n_c}$, was plotted as a function of carbon number, n_c. The chain-growth probability, α, could then be calculated from the gradient of the straight line obtained, which is described by equation 3.11.

$$ln\frac{x_{i,c}}{n_c} = n_c ln\alpha + ln\frac{1-\alpha}{\alpha} \tag{3.11}$$

The straight line was extrapolated, assuming constant chain-growth probability for products of higher carbon numbers, to account for all the products up to a carbon number of 50, representative of all products formed. The mole fraction for a product with carbon number *i* could then be calculated. This was multiplied by the carbon number to obtain the product's mole fraction on a carbon basis.

$$x_{i,c} = \dot{n}_c \exp\left(\ln\frac{x_{i,c}}{n_c}\right) \tag{3.12}$$

Where $x_{i,c}$ is the mole fraction of component *i* on a carbon basis. The value for the exponent was obtained from the extrapolated straight line (equation 3.11).

The total molar flow-rate was calculated from the molar flow-rate of the C_3 products and their mole fraction. This could be done with any of the products in the carbon number range 3-6, as these were used to construct the ASF plots for each FTS condition.

$$\dot{n}_{total} = \frac{\dot{n}_{C_3 products}}{x_{C_3 products}} \tag{3.13}$$

The molar flow-rates, on a carbon basis, for each component between C_8-C_{50} were then calculated by multiplying a component's mole fraction by the total molar flow-rate.

$$\dot{n}_{i,c} = x_{i,c}\dot{n}_{total} \tag{3.14}$$

The conversion in Fischer-Tropsch synthesis is calculated based on CO. Assuming cobalt exhibits negligible water gas shift activity, the conversion is calculated as follows:

$$X_{CO} = \frac{\dot{n}_{CO,in} - \dot{n}_{CO,out}}{\dot{n}_{CO,in}} \tag{3.15}$$

Where $\dot{n}_{CO,in}$ is the molar flow-rate of CO into the reactor and $\dot{n}_{CO,out}$ is the molar flow-rate of CO out of the reactor.

The conversion levels in this study were deliberately kept low (i.e. 1-5%; see appendix A3) so as to allow gradientless operation. As a consequence, accurate conversion measurement from CO flow-rates was not possible as only very small changes in CO flow-rates were present. The conversion was thus calculated from the product formation rates on a carbon basis, which would be equal to the difference between the molar flow-rate of CO in the reactor feed and the molar flow-rate of CO in the reactor effluent (equation 3.15). The conversion was therefore calculated according to equation 3.16.

$$X_{CO} = \frac{\sum_1^{50} \dot{n}_{i,c}}{\dot{n}_{CO,in}} \tag{3.16}$$

Where $\sum_1^{50} \dot{n}_{i,c}$ is the sum of the molar flow-rates of the Fischer-Tropsch products in the carbon number range 1-50, on a carbon basis, representative of all products formed.

The yield of a compound (on a carbon basis) could be calculated as the ratio of that compound's molar flow-rate to the inlet CO molar flow-rate, on a carbon basis.

$$Y_{i,c} = \frac{\dot{n}_{i,c}}{\dot{n}_{CO,in}} \tag{3.17}$$

From this ratio, the selectivity for a compound (on a carbon basis) could be calculated, which is the ratio of the yield of that compound to the conversion.

$$S_{i,C} = \frac{Y_{i,c}}{X_{CO}} \tag{3.18}$$

The formation rate of a compound can be used as an indication of the catalytic activity towards producing that compound. It can be used for a single compound or a group of compounds, as follows.

$$r_i = \frac{\dot{n}_{i,c}}{m_{cat}} \text{ or for a group, } r_{C_{5+}} = \frac{\sum_5^{50} \dot{n}_{i,c}}{m_{cat}} \tag{3.19}$$

Where r_i is the formation rate of compound i, $r_{c_{5+}}$ is the rate of formation of compounds with carbon numbers between 5-50 and m_{cat} is the mass of the catalyst employed.

The turnover frequency, TOF, used to indicate the surface activity, is the number of CO molecules converted per mole of exposed, surface cobalt atoms per unit time (equation 3.20).

$$TOF = \frac{\sum_1^{50} \dot{n}_{i,c}}{N_{exp,tot}} N_A \tag{3.20}$$

Where $N_{exp,tot}$ is the total number of exposed cobalt atoms on the surface and N_A is Avogadro's number (i.e. $6.022141 \cdot 10^{23}$ mol^{-1}).

Statistical methods published by van Hardeveld and Hartog (1969) provide the means to calculate the total number of atoms and the number of surface atoms, as functions of crystallite size. These methods are applicable for the face-centred cubic phase in this study, as well as for other crystal structures. In order to calculate the total number of exposed cobalt atoms on the surface, the total number of cobalt atoms in the crystallite must be calculated (equation 3.21).

$$N_{tot,cryst} = \left(\frac{d_{cryst}}{1.105 d_{Co}}\right)^3 \tag{3.21}$$

Where d_{cryst} is the average crystallite size and d_{Co} is the atomic radius of cobalt ($125.3 \cdot 10^{-3}$ nm). The d_{cryst} size was obtained from XRD size analysis and is therefore a volume-weighted size. Due to the nature of this project, it was not possible to extract catalyst samples throughout experimental runs and analyse them using TEM. Therefore, the volume-weighted sizes (calculated from Rietveld refinement of the XRD spectra), which are typically slightly larger than the number-weighted sizes, were used.

The number of edge atoms, m, is found by equating the total number of cobalt atoms (equation 3.21) to an expression that has been derived as a function of the number of edge atoms.

$$N_{tot,cryst} = 16m^3 - 33m^2 + 24m - 6 \tag{3.22}$$

With the number of edge atoms known, the number of exposed cobalt atoms can be calculated.

$$N_{exp,cryst} = 30m^2 - 60m + 32 \tag{3.23}$$

The total number of exposed cobalt atoms on the surface can then be calculated.

$$N_{exp,tot} = N_{exp,cryst} \frac{L_{Co} m_{cat}}{M_{Co}} \frac{N_A}{N_{tot,cryst}} \tag{3.24}$$

Where L_{Co} is the cobalt loading, obtained from AAS measurements and M_{Co} is the molar mass of cobalt.

Molar olefin fractions were calculated for the C_2-C_7 product fractions, by using the following equation. Branched products were excluded from this analysis as only the linear hydrocarbons (olefins and paraffins) were included.

$$o_i = \frac{\dot{n}_{o,i}}{\dot{n}_{o,i}+\dot{n}_{p,i}} \tag{3.25}$$

Where o_i is the linear olefin fraction of product fraction i (i.e. C_2-C_7 product fractions), $\dot{n}_{o,i}$ is the molar flow-rate of linear olefins of product fraction i and $\dot{n}_{p,i}$ is the molar flow-rate of linear paraffins of product fraction i.

Another olefin analysis was performed to study the isomerisation of the primary-product, linear olefins to secondary-product, linear olefins (those which have internal double bonds). In this calculation, for a given carbon number, the linear α-olefin fraction was divided by all linear olefins.

$$o_{\alpha,i} = \frac{\dot{n}_{\alpha,i}}{\dot{n}_{\alpha,i}+\dot{n}_{\beta,i}} \tag{3.26}$$

Where $o_{\alpha,i}$ is the fraction of primary-product, linear olefins in the portion of linear olefins in product fraction i, $\dot{n}_{\alpha,i}$ is the molar flow-rate of primary-product, linear olefins in product fraction i, and $\dot{n}_{\beta,i}$ is the molar flow-rate of secondary-product, linear olefins (i.e. those linear olefins that have internal double bonds) in product fraction i.

The branched product ratio (the ratio of branched hydrocarbons to linear hydrocarbons) was calculated, as a function of water partial pressure, for the C_5 product fraction only, as a representative product fraction.

$$b_{C_5} = \frac{\dot{n}_{b,C_5}}{\dot{n}_{o,i}+\dot{n}_{p,i}} \tag{3.27}$$

Where b_{C_5} is the fraction of branched compounds in the C_5 product fraction and $\dot{n}_{b,C_5}$ is the molar flow-rate of all branched compounds in the C_5 product fraction.

4 Results

The results for the experiments conducted in this study are presented here. The unsupported catalyst precursors, as synthesised using the reverse micelle technique (see section 3.1.1), were characterised using transmission electron microscopy. The results of the X-ray interference tests of the selected borosilicate capillary are presented. A temperature profile over the capillary was generated, with emphasis on the reaction zone. The commissioning of the *in-situ* X-ray diffraction cell entailed *in-situ* temperature-programmed reduction and Fischer-Tropsch synthesis. The results of the catalyst changes throughout these experiments are presented and described. Finally, the analysis of catalyst activity and product selectivity is presented. Discussion of these results is made in section 5, and for maximum clarity these two sections should be read in parallel.

4.1 *Ex-Situ* Characterisation of Fresh Catalysts

Crystallite size distributions were generated using TEM and average size analysis was performed using XRD, for each catalyst sample. TEM size analysis results in a number-based size distribution, while XRD yields a volume-based size. In order to compare these two, the number-based average size (generated from TEM analysis) was converted to a volume-based size (equation 3.4). This was done because XRD analysis was the main context of this study. The details of the instruments and the respective methods implemented can be found in sections 3.1.2 and 3.1.3.

Catalysts A and B were employed for the *in-situ* runs. The characteristics of these catalysts are listed in table 4.1.

Table 4.1: Characteristics of the catalysts synthesised in this study.

Catalyst	ω[a] (mol/mol)	$Co(NO_3)_2 \cdot 6H_2O$ Conc. (mol/l)	Co_3O_4 Crystallite Size XRD[b]	Co_3O_4 Crystallite Size TEM[c]	Loading (AAS[d]) (%)
A	0.4	0.32	11.1	10.3±1.9	6.4
B	0.2	0.08	6.7	6.1±1.4	4.0

[a] Molar water-to-surfactant ratio

[b] XRD sizes (volume-based average) calculated using Rietveld refinement in TOPAS 4.2

[c] TEM sizes are volume-based, calculated from the number-based sizes using the following equation: $d_{TEM,vol} = \frac{\sum n_i d_{TEM,num}^4}{\sum n_i d_{TEM,num}^3}$, where $d_{TEM,vol}$ is the calculated, volume-based TEM size, n_i is the number of measured crystallites of a particular size (i.e. $d_{TEM,num}$), and $d_{TEM,num}$ is the number-based TEM size, as measured from the micrographs.

[d] Atomic Absorption Spectroscopy

TEM micrographs of the unsupported, fresh Co_3O_4 in catalysts A and B, with corresponding crystallite size distributions, are presented in figure 4.1. The reverse micelle technique resulted in

narrow crystallite size distributions, indicated by the size of the standard deviation in each case (see table 4.1). A narrow size distribution is essential for catalysts A and B to be model catalysts.

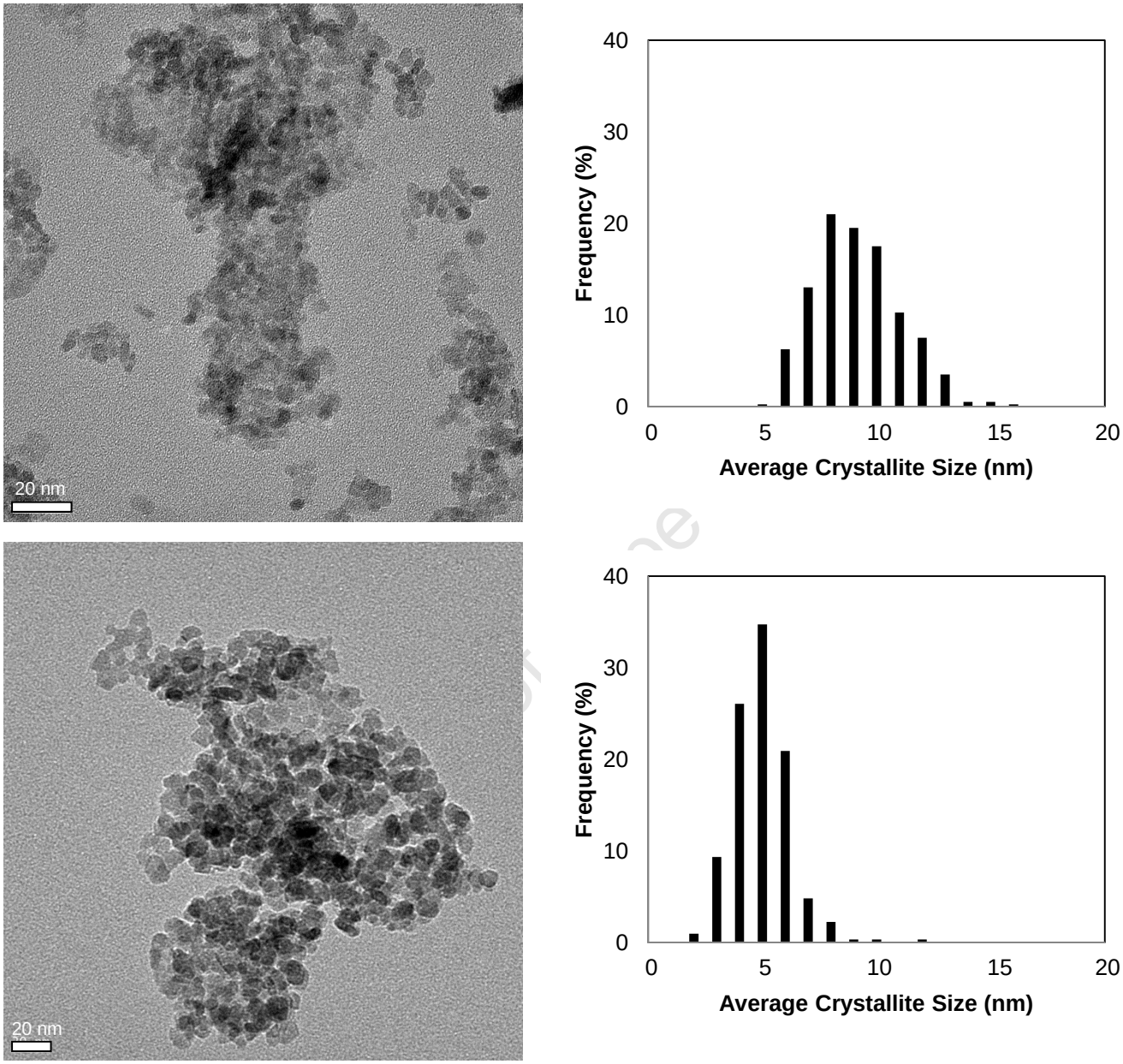

Figure 4.1: TEM micrographs and number-based, crystallite size distributions of unsupported Co_3O_4 of catalyst A, above, and B, below. The number-based sizes are slightly smaller than the volume-based sizes.

4.2 Cold Cell Commissioning

In commissioning the *in-situ* cell, it was important to understand the background contribution from the capillary tube after X-rays had passed through it and were detected. In order to do this, an experiment was performed where an XRD spectrum of a sample of Y_2O_3 was generated. This sample of large crystallites resulted in a spectrum with narrow peaks of high intensity, making it ideal for the

interference study. After a suitable height for the reaction cell was obtained, using the designed height-adjustment feature (see figure 3.4), a sample of catalyst A was studied. It had smaller crystallites than did the Y_2O_3 sample, resulting in wider peaks with lower intensities. This resulted in a more realistic scenario for the *in-situ* experiments. A temperature profile of the capillary, with emphasis on the zone where the catalyst bed and X-ray beam coincided, was generated. This was performed with an empty capillary by moving a thermocouple through it. In this case, the potential difference across the infrared heaters was kept constant to maintain a constant power output.

4.2.1 X-Ray Interference

Capillaries H2S (sapphire; wall thickness of 0.2 mm) and H2Q02 (quartz; wall thickness of 0.2 mm) (see section 3.2.1 for details) provided no readings when Y_2O_3 was loaded into them, as their walls were too thick. The thinner-walled CQ002 (quartz; wall thickness of 0.02 mm) and CQ001 (quartz; wall thickness of 0.01 mm) provided readings with sufficient information to identify the crystal phases present, with CB002 (borosilicate; wall thickness of 0.02 mm) and CB001 (borosilicate; wall thickness of 0.01 mm) providing the best results. CB002 was selected for the *in-situ* experiments, as its wall thickness of 0.02 mm provided increased structural integrity over that of CB001 (wall thickness of 0.01 mm).

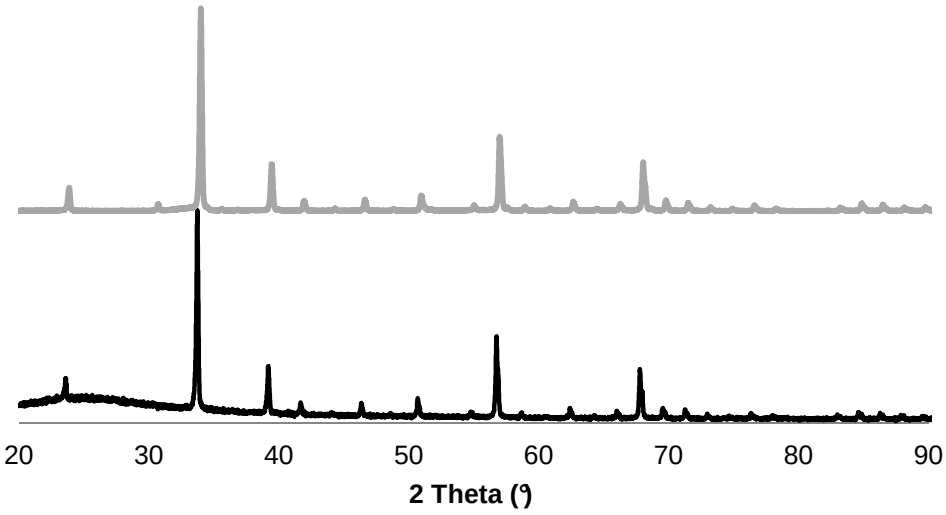

Figure 4.2: XRD scans of Y_2O_3 within capillary CB002 (black) and standard *ex-situ* method (i.e. using a zero-background holder) (grey).

It can be seen from figure 4.2 that the characteristic peaks of Y_2O_3 are identifiable when using capillary CB002. The presence of a background bump between 2θ angles of 20-40° (figure 4.2, black spectrum) is a contribution from the amorphous borosilicate phase (see figure 4.3), especially at low angles where X-rays have to travel through more of the capillary (see schematic in figure 5.1). The relative peak heights in both spectra in figure 4.2 are almost identical, confirming the presence of Y_2O_3, and indicating almost no signal intensity loss when using this capillary.

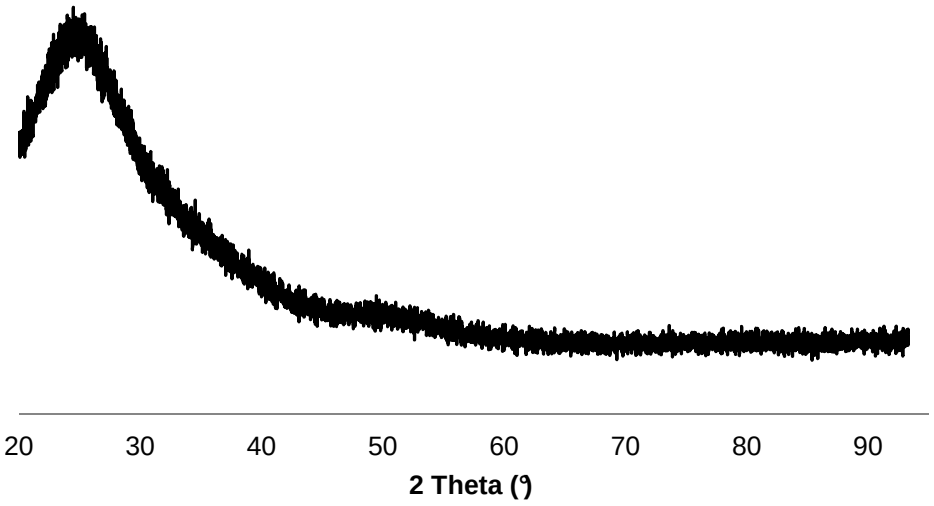

Figure 4.3: XRD scan of crushed borosilicate, using standard *ex-situ* method (i.e. using a zero-background holder).

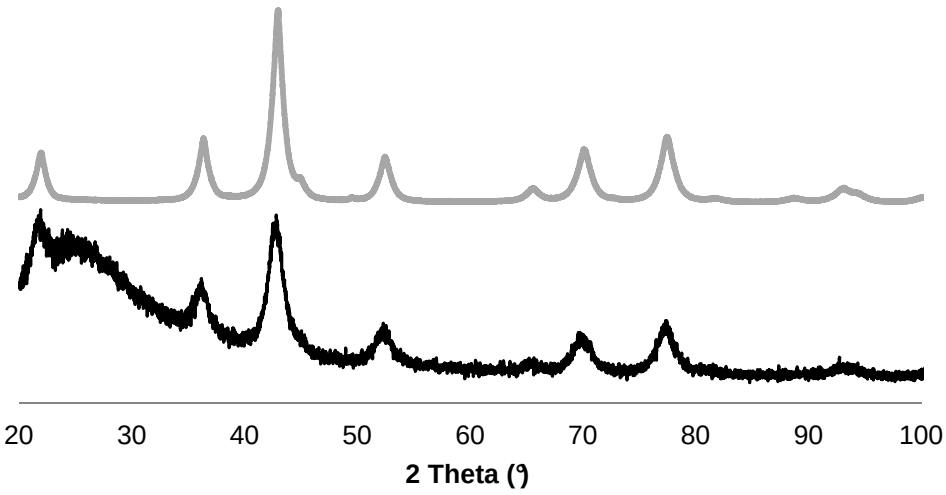

Figure 4.4: XRD scans of unsupported catalyst A (i.e. Co_3O_4) within capillary CB002 (black) and standard *ex-situ* method (grey). Note contribution from amorphous borosilicate between 20-40°.

The characteristic peaks and their positions of the sample of unsupported catalyst A (i.e. Co_3O_4) (figure 4.4, black spectrum) are identifiable. Rietveld refinement in TOPAS was performed on this scan, for 2θ angles between 30-120°, yielding a size of 9.7 nm, which is in agreement with the size of 11.1 nm, calculated from refinement of the standard *ex-situ* scan (figure 4.4, grey spectrum). TOPAS is able to analyse and subtract the background contribution from the borosilicate capillary (seen in figure 4.4 (black spectrum) for the unsupported Co_3O_4 and in figure 4.5 (black spectrum) for the supported Co_3O_4/Al_2O_3). Additionally, because the scans for the *in-situ* experiments were taken between 2θ angles of 40-90° (as all the major peaks of the cobalt phases are present in this range), the bulk of the background contribution was inherently eliminated.

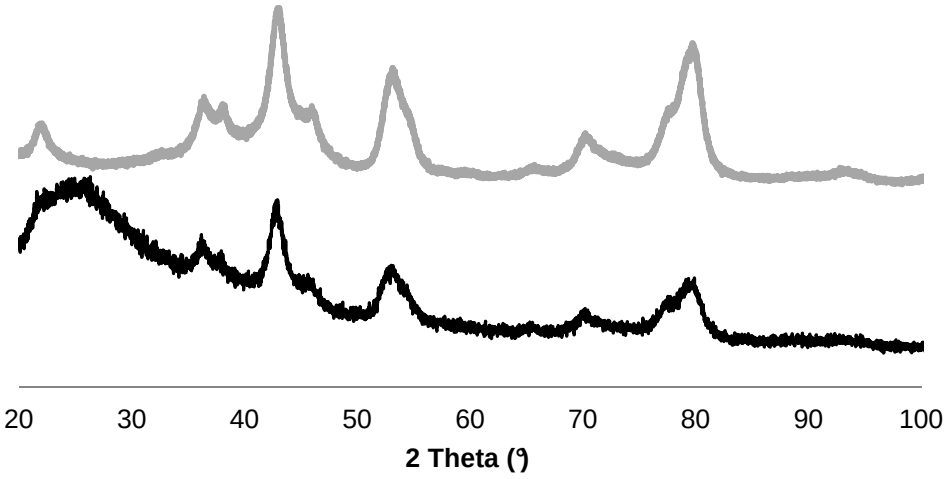

Figure 4.5: XRD scans of catalyst A (i.e. Co_3O_4/Al_2O_3) within capillary CB002 (black) and standard *ex-situ* method (grey).

4.2.2 Temperature Profile of Capillary Reaction Cell

The temperature profile along the capillary (figure 4.6) with the infrared heaters placed in the position as described in section 3.2.1 (i.e. end-to-end) was generated by moving a thermocouple through the capillary and is presented in figure 4.6. During the generation of the temperature profile, a constant voltage was maintained across the infrared heaters. Over the length of the catalyst bed, temperature deviations of ±4°C were present for the approximate reaction temperature of 220°C. At a higher temperature of about 340°C, the deviation was ±4.3°C, indicating that good temperature control is maintained at higher temperatures. Outside of the catalyst zone the temperature decreases rapidly. It should be noted that during these measurements the inlet and outlet zones of the cells were not heated.

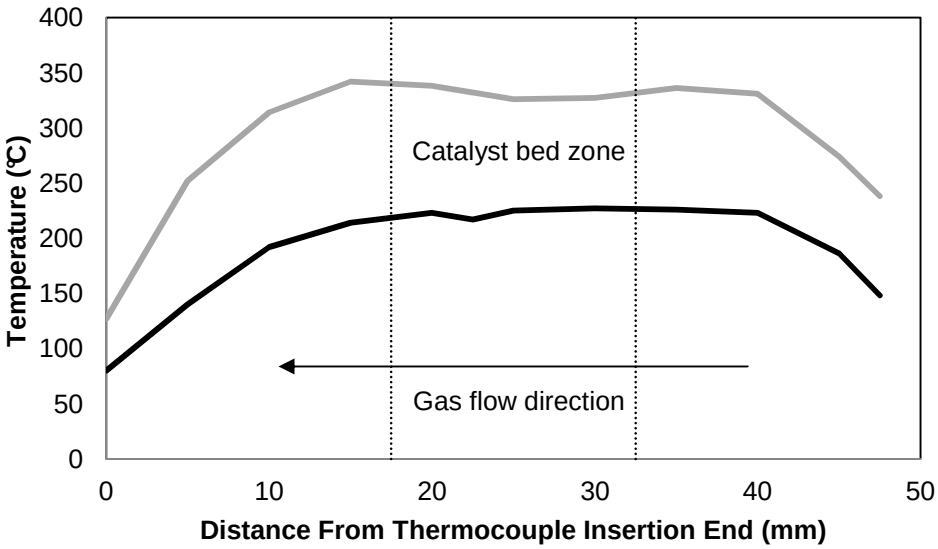

Figure 4.6: Axial temperature profile across capillary. Two profiles were measured, one at a lower temperature (black), around the reaction temperature of 220°C, and one at about 340°C (grey).

4.3 *In-Situ* Reduction and Fischer-Tropsch Experiments

4.3.1 Temperature-Programmed Reduction

Catalysts were reduced *in situ*, according to the method described in section 3.3.1. Figures 4.7-4.8 were constructed from the *in-situ* XRD diffractograms and illustrate the results of the temperature-programmed reduction for the catalysts studied. Crystal phases are identified according to the relative intensities of the peaks, the positions of which are functions of the angle 2θ. The colours represent intensity levels, increasing in the following order: dark blue, light blue, green, yellow, orange and red.

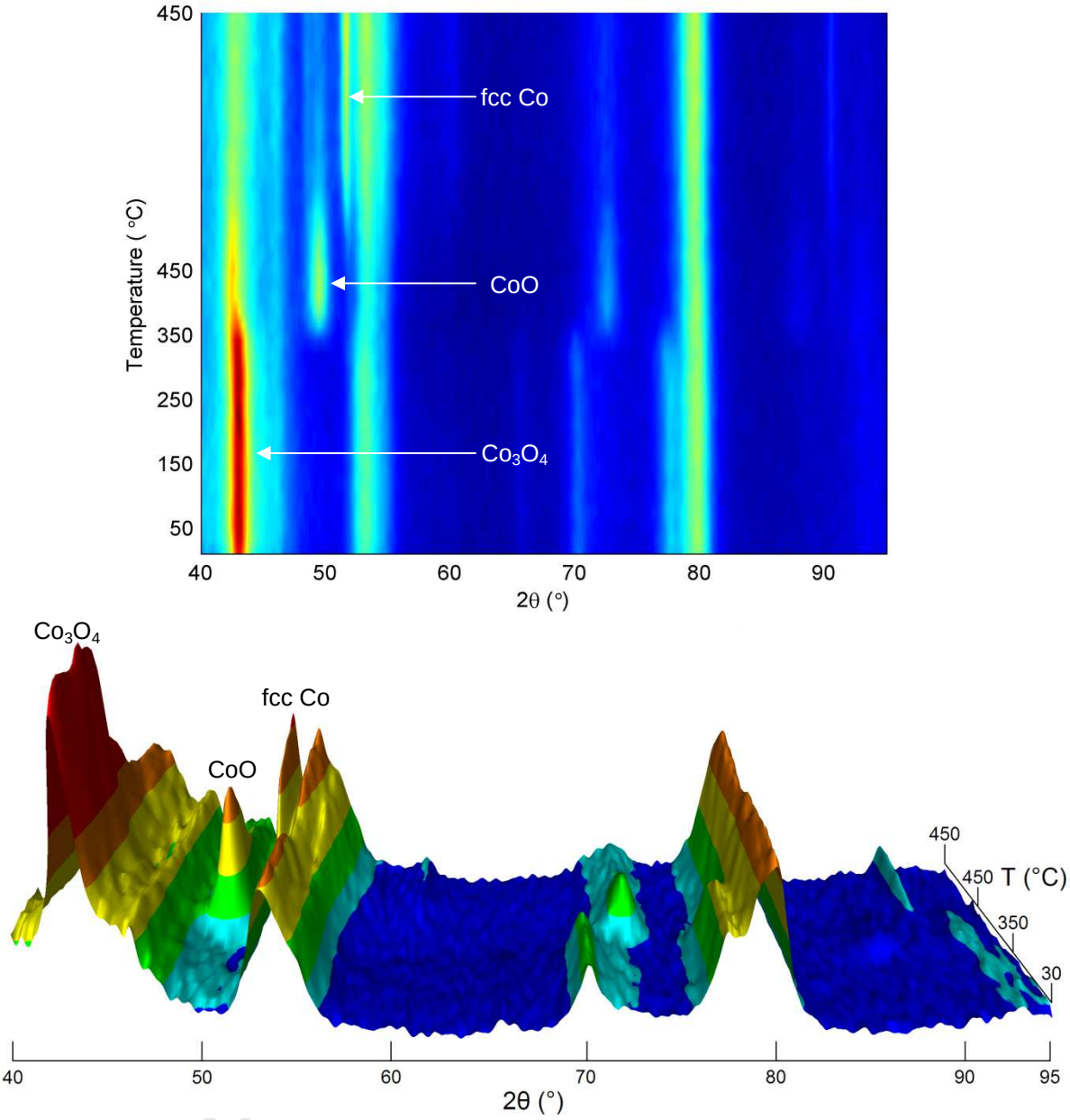

Figure 4.7: Top view, above, and three-dimensional view, below, of the XRD spectra obtained during the *in-situ* reduction of catalyst A (the catalyst with the larger crystallites), illustrating phase changes from Co_3O_4 to CoO to fcc Co, as functions of temperature and the angle 2θ. Major peaks for the cobalt-based phases are highlighted.

The permanent peaks at 2θ angles 43, 53 and 80° (more clearly visible in the top view) are characteristic of the γ-alumina phase present. In the case of catalyst A (the catalyst with the larger crystallites), the Co_3O_4 phase, identified by the peaks present at 2θ angles 43, 70 and 78°, was reduced to CoO between 350 and 450°C. CoO is identified by the peaks present at 2θ angles 50 and 73°. This phase was reduced, though not fully, to face-centred cubic (fcc) Co at 450°C, identified by the peaks at 2θ angles 52 and 91°. The most significant peak for the hexagonal closed-packed (hcp) Co phase, which would appear at 2θ angle 55°, was considered insignificant in comparison with the intensity of the fcc Co peak (refer to three-dimensional view in figure 4.7), resulting in the conclusion that the metallic Co present was essentially pure fcc.

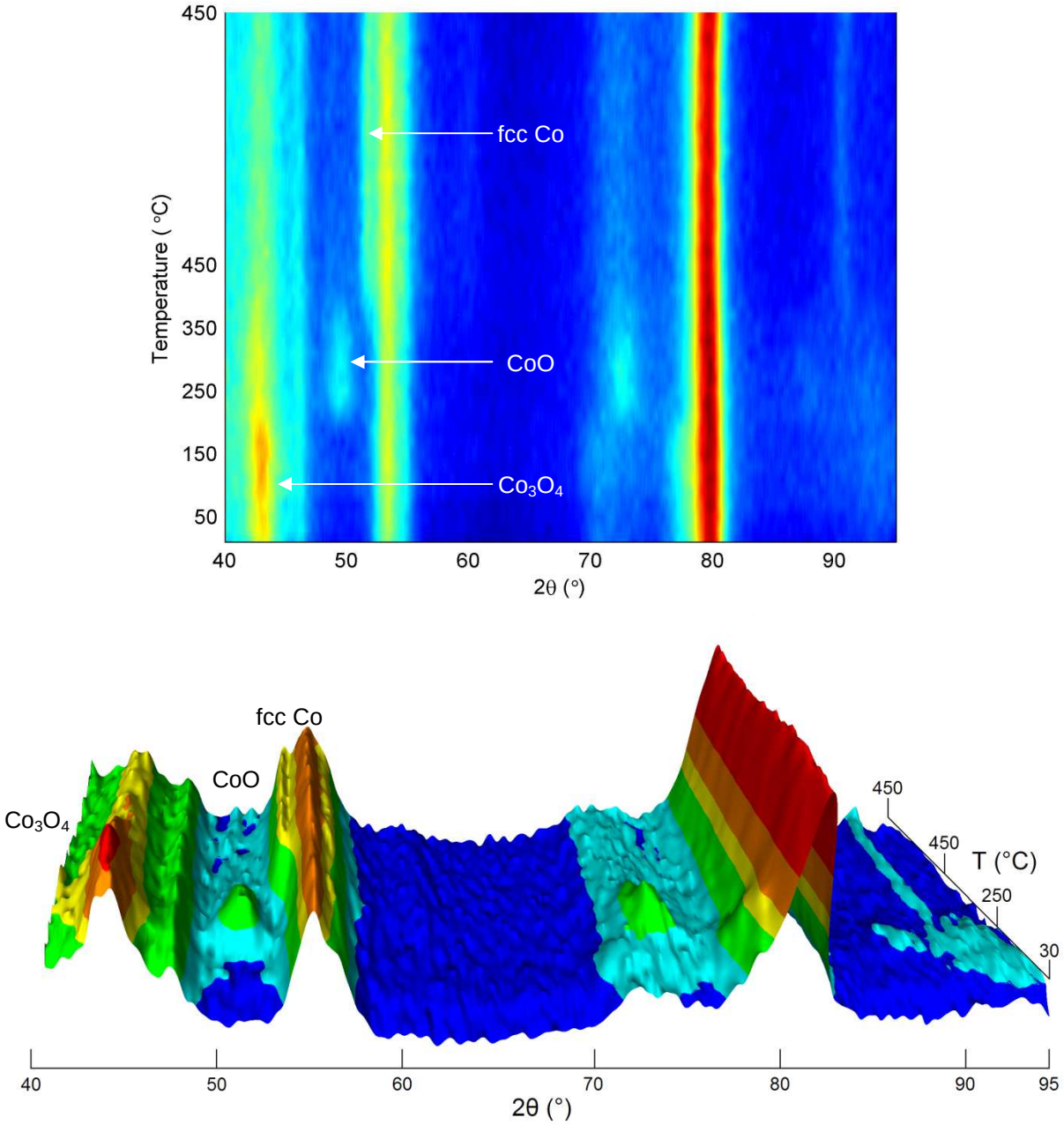

Figure 4.8: Top view, above, and three-dimensional view, below, of the XRD spectra obtained during the *in-situ* reduction of catalyst B (the catalyst with the smaller crystallites), illustrating phase changes from Co_3O_4 to CoO to fcc Co, as functions of temperature and the angle 2θ. Major peaks for the cobalt-based phases are highlighted.

In the case of catalyst B (the catalyst with the smaller crystallites), the Co_3O_4 phase, identified by the peaks present at 2θ angles 43, 70 and 78°, was reduced to CoO between 190 and 380°C. This phase was reduced to fcc Co at 450°C, identified by the peaks at 2θ angles 52 and 91°. The metallic Co present (2θ angles 52 and 91°) was essentially pure fcc, as was the case with catalyst A. Catalyst A was reduced to the intermediate oxide and final metallic phases at higher temperatures (figure 4.7), indicating its lower reducibility.

4.3.2 Fischer-Tropsch Synthesis

Fischer-Tropsch synthesis experiments were carried out at 220°C and 1 bar(a) syngas (60% H_2, 30% CO, 10% Ar). Water was co-fed with the syngas at increasing partial pressures to simulate higher conversions. In table 4.2 are the catalyst masses and reduction and syngas flow-rates used in the reduction and FTS runs, respectively. The manner in which the catalysts were packed into the capillary was the same, being a function of the particle size distribution of the support.

Table 4.2: Catalyst masses and gas flow-rates used in reduction and FTS experiments.

Catalyst	**Mass (mg)**	**H_2 Flow-Rate (ml(NTP)/min)**	**Syngas Flow-Rate (ml(NTP)/min) [a]**
A	10.3	0.824	0.916
B	13.7	1.096	1.218

[a] syngas flow-rate includes Ar, which was present in the gas mixture

Figures 4.9-4.10 were constructed from the *in-situ* XRD diffractograms of the catalysts during the FTS runs with both catalysts and illustrate how the phases changed as a function of water partial pressure, P_{H_2O}.

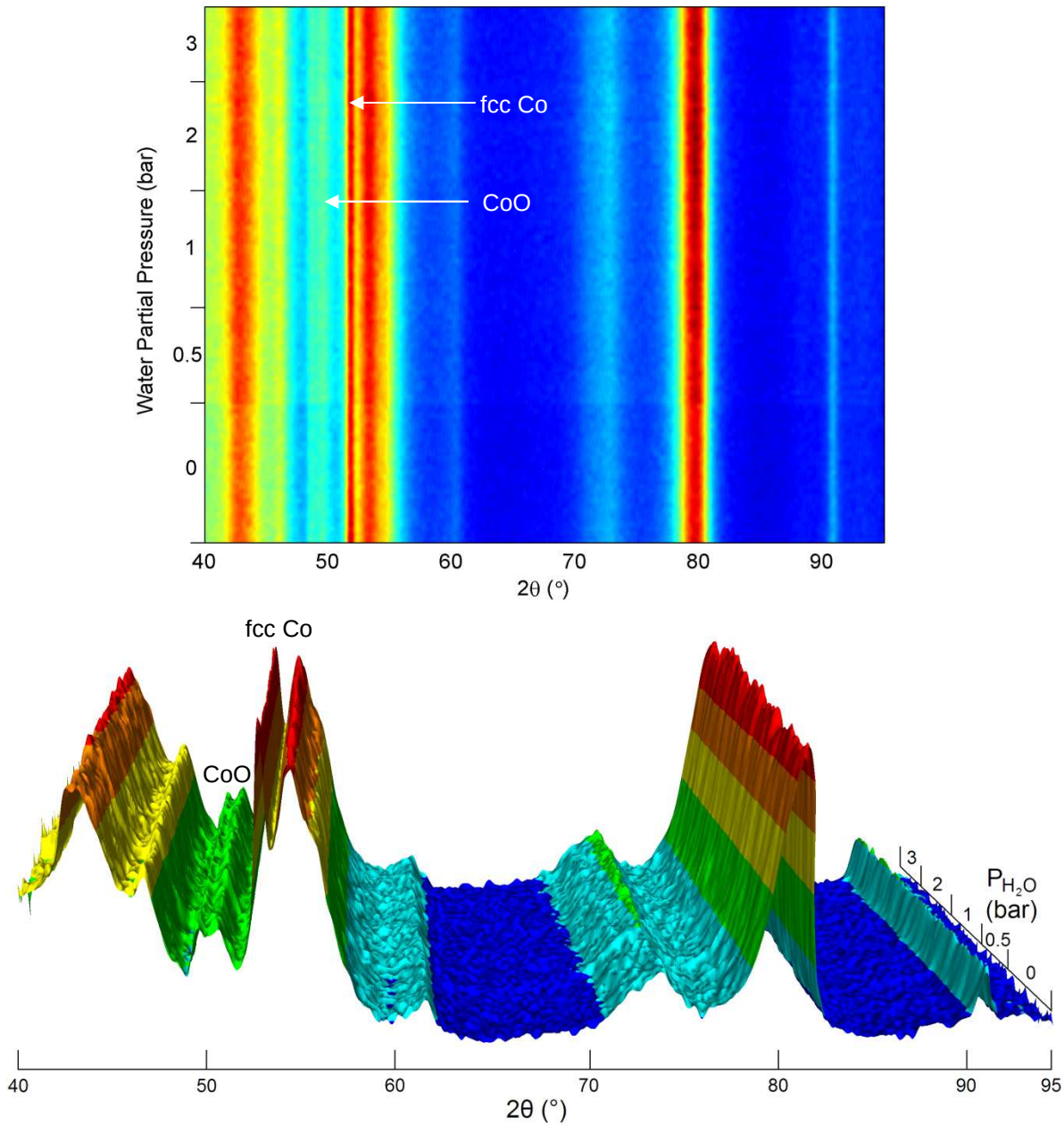

Figure 4.9: Top view, above, and three-dimensional view, below, of the XRD spectra obtained during the *in-situ* FTS runs with catalyst A (the catalyst with the larger crystallites). Major peaks for the cobalt-based phases are highlighted.

In figure 4.9 it can be seen that no oxidation of catalyst A (the catalyst with the larger crystallites) occurred as fcc Co peaks at 2θ angles 52 and 91° remained throughout the time on stream. A small portion of CoO was present throughout the reaction, the phase that was not fully reduced to Co during reduction. No peaks disappeared nor did new peaks appear, indicating that the catalyst composition remained the same.

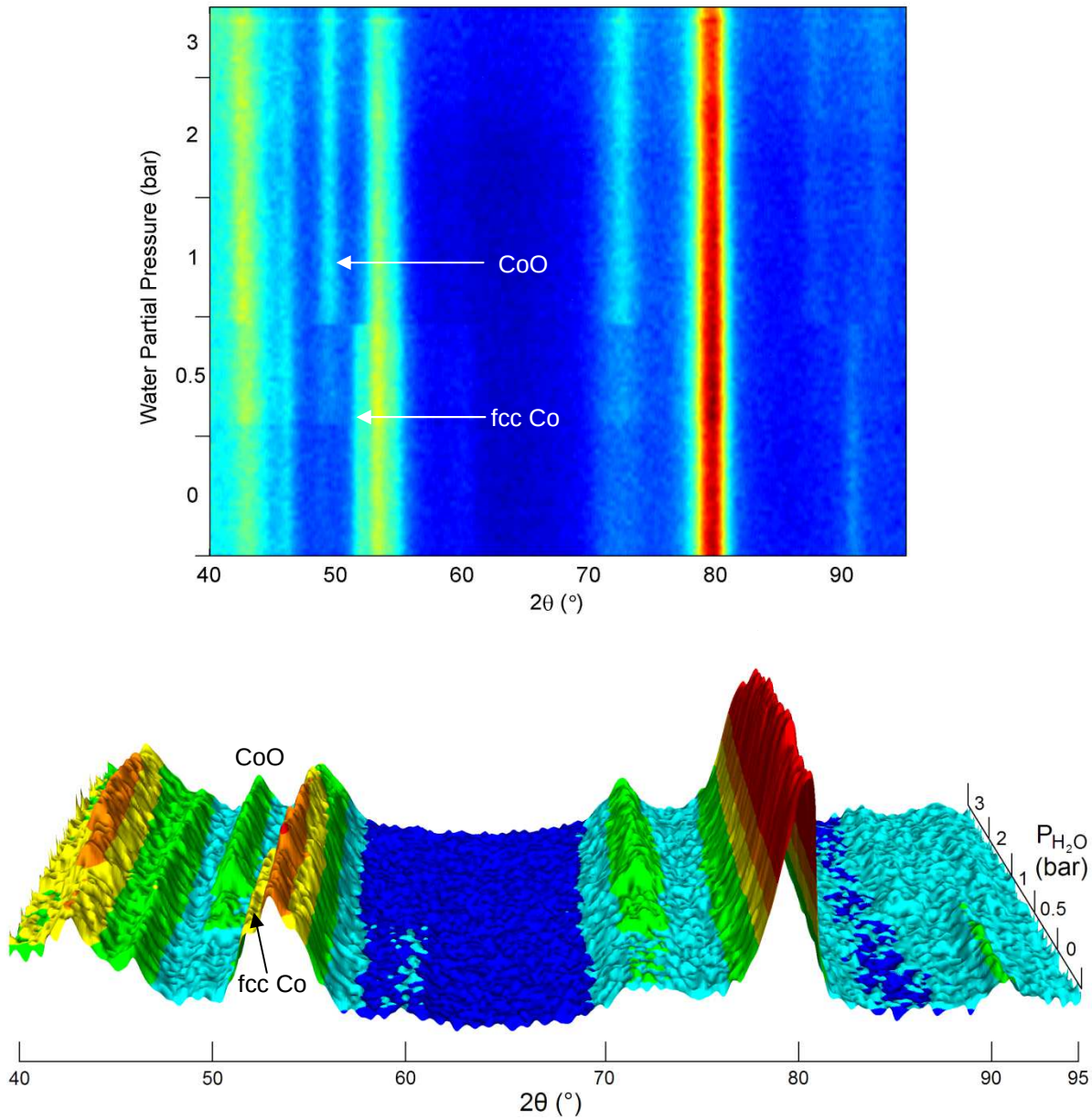

Figure 4.10: Top view, above, and three-dimensional view, below, of the XRD spectra obtained during the *in-situ* FTS runs with catalyst B (the catalyst with the smaller crystallites). Initiation of reoxidation of Co to CoO observed at a P_{H_2O} of 0.5 bar, and a complete reoxidation to CoO observed at a P_{H_2O} of 1 bar. Major peaks for the cobalt-based phases are highlighted.

In the case of catalyst B (the catalyst with the smaller crystallites), it can be seen that the fcc cobalt phase was present after dry syngas conditions ($P_{H_2O} \approx 0$ bar) during the FTS runs (figure 4.10). The CoO phase began to form at a P_{H_2O} of 0.5 bar, with fcc Co still present. At a P_{H_2O} of 1 bar, the fcc Co had been completely oxidised to CoO. It must be noted that this is the first time ever that oxidation has been observed directly and in real time.

Crystallite size analysis of the cobalt phases over the duration of the reduction and FTS runs was performed using Rietveld refinement in TOPAS (see section 3.1.2 for details). This permitted the simultaneous determination of the sizes of all cobalt phases present.

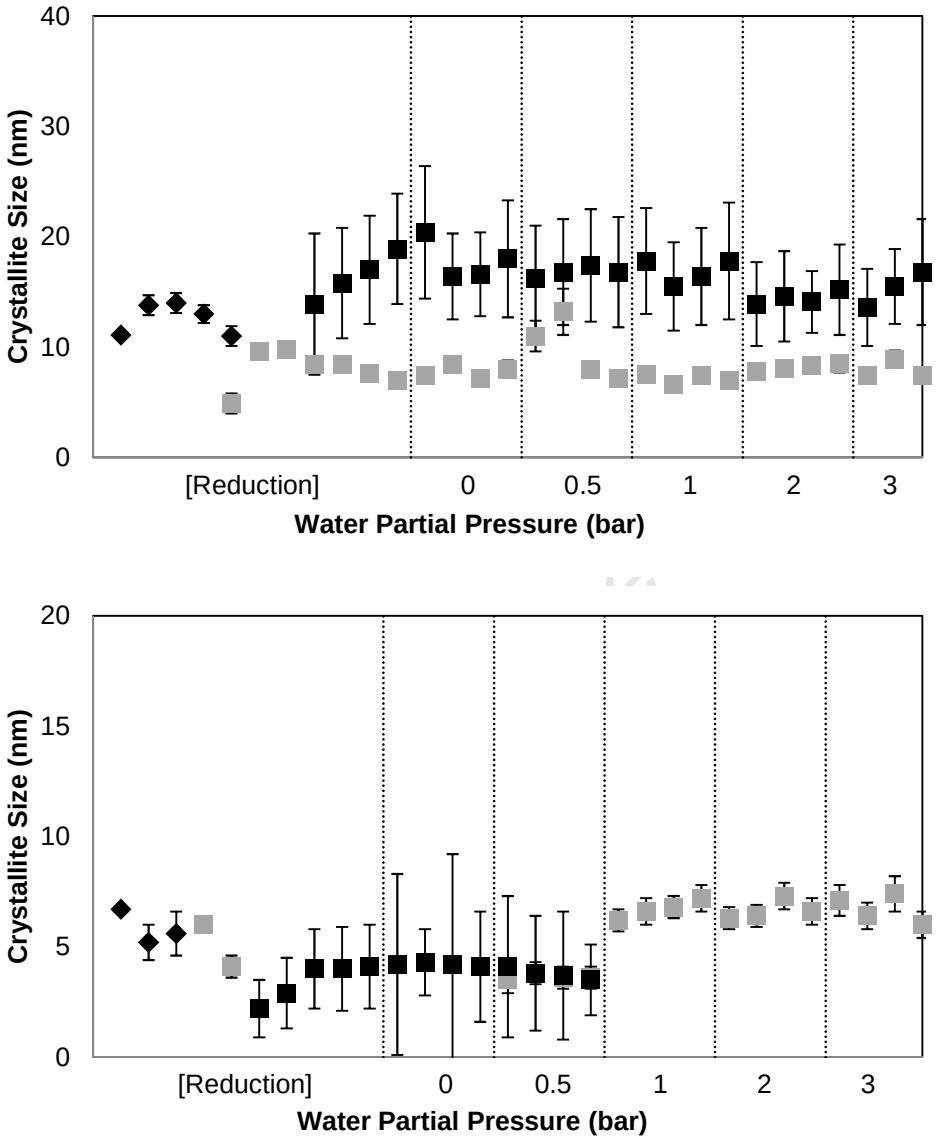

Figure 4.11: Crystallite sizes of Co_3O_4 (◆), CoO (■) and Co (■) in the cases of catalyst A, above, and B, below, as determined by Rietveld refinement (errors calculated in TOPAS).

From the size analyses (figure 4.11), it can be seen, in the case of catalyst A, that the crystallites of the metallic Co phase, after formation, increased in size under reduction conditions. A size increase is also observed in the case of catalyst B, but not to the same degree as in the case of catalyst A. Subsequently, the crystallites of both catalysts underwent no sintering throughout the FTS runs.

In table 4.3 are listed the cobalt crystallite sizes, as calculated from the *in-situ* XRD spectra, where cobalt was stable in the metallic form under FTS conditions with the corresponding P_{H_2O}/P_{H_2} ratios. In the case of catalyst B, oxidation was found to begin at a P_{H_2O}/P_{H_2} ratio of 0.83 and metallic cobalt was

no longer XRD-visible for a P_{H_2O}/P_{H_2} ratio of 1.67. Therefore, for a cobalt crystallite size of approximately 3.5 nm, complete oxidation is expected to occur with a P_{H_2O}/P_{H_2} ratio of 1.67.

Table 4.3: Crystallite sizes where cobalt is stable in the metallic form under FTS conditions and elevated simulated conversions. Actual conversion maintained below 5% at all times (see appendix A3).

P_{H_2O} (bar)	P_{H_2O}/P_{H_2}	Simulated Conversion (%)	Cobalt Crystallite Size (XRD) (nm)	
			Catalyst A	Catalyst B
0.0	0.00	0	18.0	4.1
0.5	0.83	63	16.8	3.5 [a]
1.0	1.67	77	17.8	3.5 [b]
2.0	3.33	87	15.2	[-]
3.0	5.00	91	16.8	[-]

[a] metallic phase still present, making up 30 wt % of the cobalt-containing phases (balance CoO)

[b] metallic phase not XRD-visible; size listed is for the metallic phase at the previous condition, as an indication of the size at which oxidation is expected to occur; this is also presented in figure 4.12

The results of this work were compared with thermodynamic calculations, graphically presented in figure 4.12. The sizes in figure 4.12 are the metallic cobalt sizes that are stable under FTS conditions at the corresponding P_{H_2O}/P_{H_2} ratios.

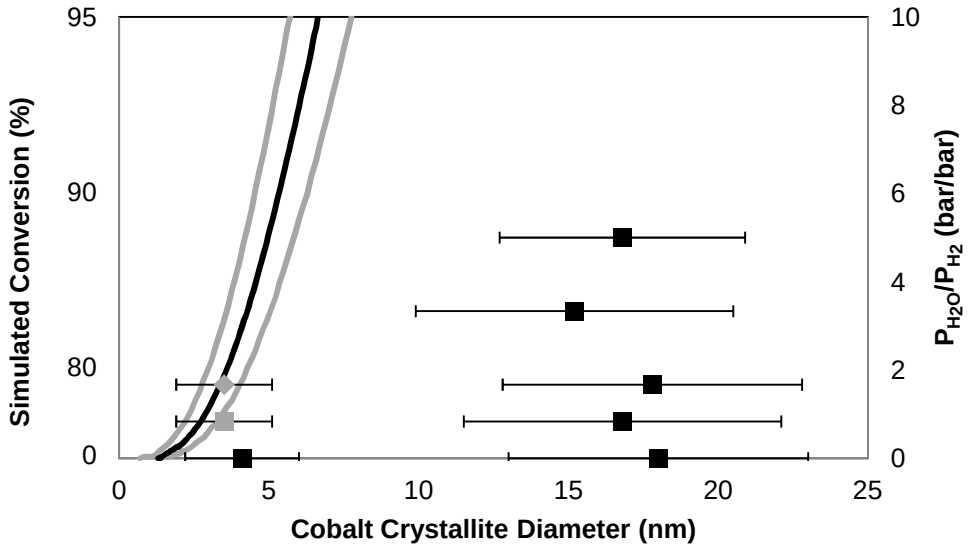

Figure 4.12: Cobalt crystallite sizes and corresponding FTS conditions at elevated simulated conversions compared with thermodynamic calculations. Thermodynamic line (black) calculations performed by van Steen *et al*. (2005). Grey lines represent a surface energy margin of 10%. Values generated in this study include non-oxidised cases (■), case where oxidation was first observed and metallic phase was still present (■), and a hypothetical case where complete oxidation is expected to occur (◆). All sizes are metallic cobalt sizes at the corresponding simulated conversion, and in the hypothetical case, the size of the metallic cobalt immediately before complete oxidation was observed.

In the case of catalyst A, no oxidation of the fcc cobalt phase was observed (figure 4.12). In the case of catalyst B, after exposure to dry FTS conditions (P_{H_2O} of 0 bar), the fcc cobalt phase was the only XRD-visible phase in which cobalt was present. The average fcc cobalt crystallite size for this case was about 4.1 nm. After exposure to FTS conditions and a P_{H_2O} of 0.5 bar, corresponding to a simulated conversion of 63%, the fcc cobalt average crystallite size was calculated to be about 3.5 nm (within error range of the previously-calculated 4.1 nm). Under these conditions, the metallic cobalt began to be oxidised to CoO, the thermodynamically more stable phase (figure 4.12), such that the metallic phase made up 30 wt % of the cobalt-containing phases, as calculated from Rietveld refinement. At a P_{H_2O} of 1 bar, corresponding to a simulated conversion of 77%, the fcc cobalt had been completed oxidised to CoO. In figure 4.12, the grey diamond represents the metallic fcc cobalt size at which complete reoxidation is expected to occur (i.e. it is the average fcc cobalt crystallite size after exposure to FTS conditions and a P_{H_2O} of 0.5 bar). Remarkably, these results are in agreement with thermodynamic calculations.

4.4 *Ex-Situ* Characterisation of Spent Catalysts

TEM micrographs were taken of the passivated cobalt catalysts after FTS conditions. These are presented in figure 4.13.

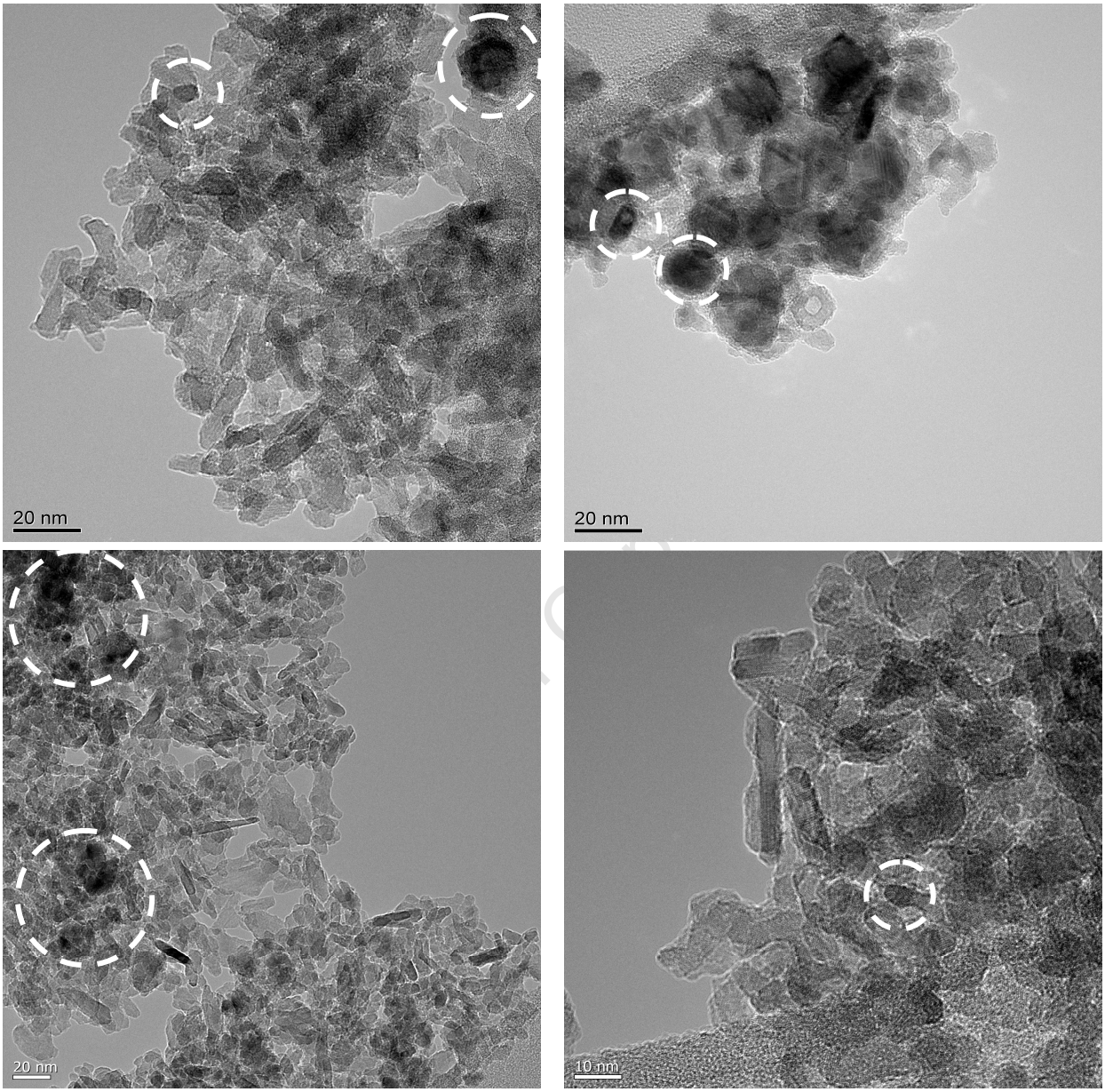

Figure 4.13: TEM micrographs of spent catalyst A, above two, and B, bottom two. The white circles highlight regions where a crystallite or group of crystallites has been identified.

Due to difficulties in distinguishing between the cobalt and alumina phases, no size distributions for the spent catalysts could be generated (see discussion in section 5.4). However, the few crystallite sizes that were identified were in agreement with the sizes calculated from Rietveld refinement of the XRD spectra. The needle-like structures in the top-left image and bottom two images in figure 4.13 may be Boehmite (Tsakoumis *et al*., 2010), an AlO(OH) phase.

4.5 Kinetic Analysis

Online GC-TCD analysis was performed to determine when steady state for each condition had been achieved (see appendix A1 for methane flow-rates, which were used to determine steady state). Methane, the flow-rate of which was calculated from GC-TCD calibration and analysis, was used as the reference/tie compound for GC-FID data, in order to calculate the molar flow-rates for the other compounds.

Ampoule samples were taken, when steady state operation had been achieved, for each set of FTS conditions (i.e. each water partial pressure). Due to technical problems, ampoules samples could not be taken for experiments where water with a partial pressure of 3 bar was co-fed with the syngas. From offline GC-FID analysis, the following observations regarding FT activity and product selectivity were made for FT operation with both catalysts. Note that even though the XRD spectra indicated no metallic phase present for catalyst B from a P_{H_2O} of 1 bar, product formation was still detectable. The remaining metallic phase was no longer XRD-visible, either due to crystallite size or the low concentration of the phase.

Chain-growth probabilities were calculated from Anderson-Schulz-Flory (ASF) plots (see appendix A2 for ASF plots) constructed from the molar product fractions of the C_3-C_6 compounds for each set of FTS runs for each catalyst. The ASF plot for each water partial pressure was extrapolated to C_{50}, assuming chain-growth probability to be constant with increasing carbon number, approximating ideal polymerization (Schulz, 2003). The flow-rates of all the compounds could subsequently be calculated. Selectivities of methane and the C_{5+} compounds (on a carbon basis) and turnover frequencies (TOF) were thus calculated. Olefin and branching analyses were also conducted. The results of the kinetic analyses are presented in the following sections.

4.5.1 Activity

The formation rate for all Fischer-Tropsch products (figure 4.14) as well as for methane and C_{5+} products (figure 4.15) were calculated.

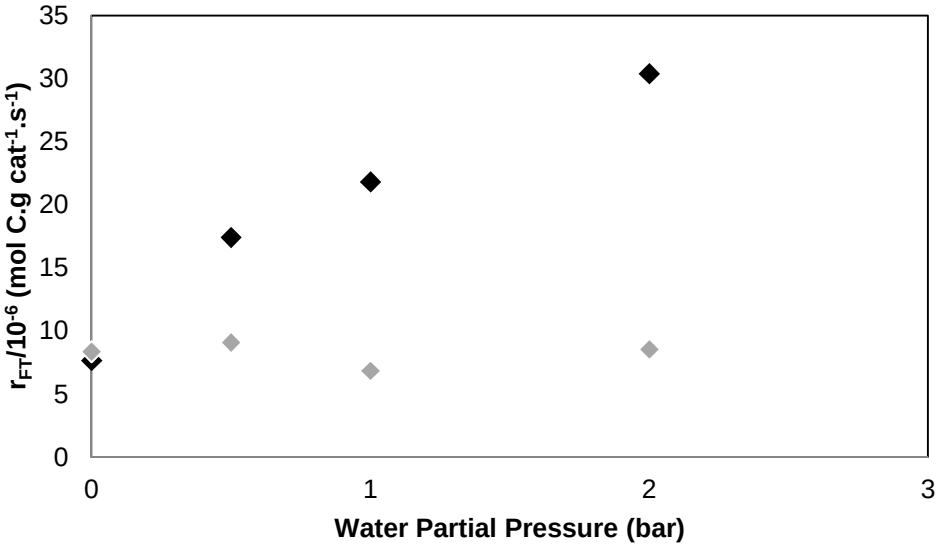

Figure 4.14: Formation rate of Fischer-Tropsch products for runs with catalysts A (◆) and B (◆).

The formation rate of FT products was found to increase with increasing water partial pressure in the case of catalyst A and remain approximately constant in the case of catalyst B. The discussion for the reasons behind these trends is made in section 5.5.1.

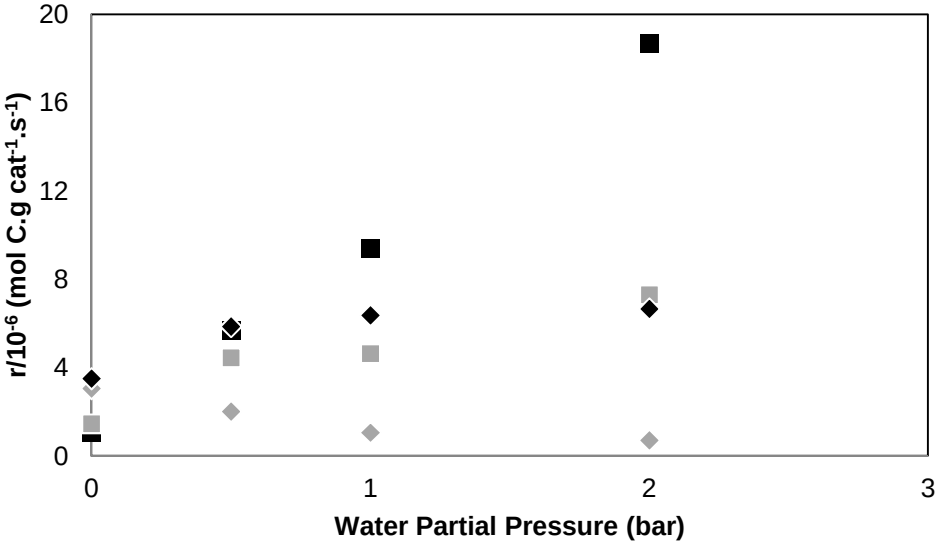

Figure 4.15: Methane (◆, ◆) and C_{5+} (■, ■) formation rates for FTS runs with catalysts A (black) and B (grey).

For both catalysts, the methane formation rate was approximately the same and the C_{5+} formation rate was approximately the same during the dry condition. In the case of catalyst A, the C_{5+} formation rate increased with increasing water partial pressure, while the methane formation rate, after increasing between the dry condition and a P_{H_2O} of 0.5 bar, remained approximately constant for the conditions with the higher water partial pressures. In the case of catalyst B, the methane formation rate decreased

and the C_{5+} formation rate increased with increasing water partial pressure, with the C_{5+} formation rate increasing to a much lower extent than in the case of catalyst A.

Turnover frequencies (TOF) were calculated for each FTS condition. These are presented in table 4.4 and figure 4.16. The TOF is a good indication of catalyst activity as it is the number of carbon monoxide molecules converted per surface cobalt atom per unit time. Crystallite size affects the TOF as the number of surface atoms depends on size. For the case of catalyst B, at a P_{H_2O} of 0.5 bar, the metallic cobalt was calculated, from the Rietveld refinement results, to make up 30 wt % of the cobalt-containing phases (fcc Co and CoO). The atmosphere also has an important influence on TOF. This latter factor's effect is observed in the current study as the crystallite sizes of the respective catalysts were approximately equal.

Table 4.4: Turnover frequencies for each catalyst under each FTS condition with corresponding crystallite sizes.

Catalyst	**fcc Co Size (XRD) (nm)**	**P_{H_2O} (bar)**	**TOF ($molC \cdot gCo^{-1}s^{-1}$)**
A	18.0	0	3.4×10^{-3}
	16.8	0.5	6.9×10^{-3}
	17.8	1	9.2×10^{-3}
	15.2	2	11×10^{-3}
B	4.1	0	1.3×10^{-3}
	3.5 [a]	0.5	4.3×10^{-3}

[a] Co calculated to be 30 wt % Co of the cobalt-containing phases (balance CoO)

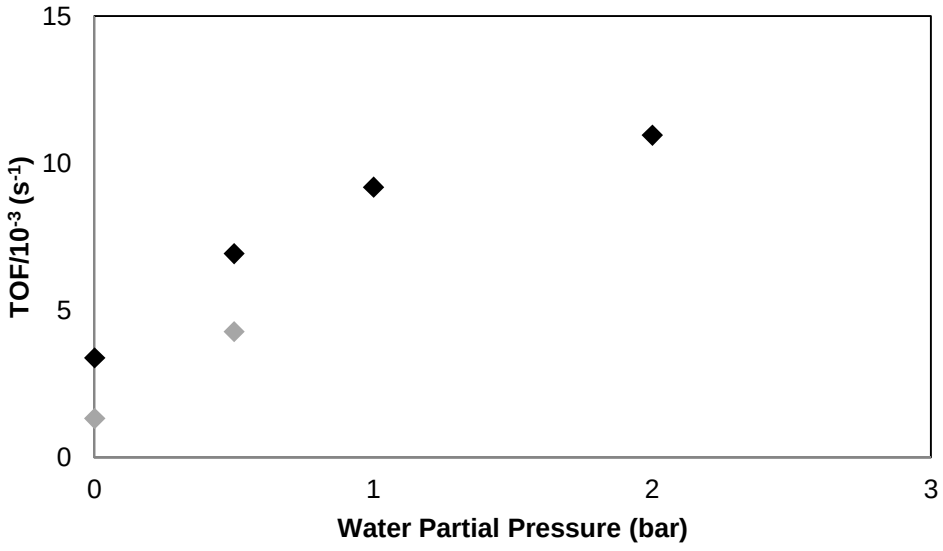

Figure 4.16: Turnover frequencies calculated for each set of FTS runs for each water partial pressure where fcc Co crystallite size was quantifiable, for catalysts A (◆) and B (◆).

In the case of catalyst A, the TOF was found to increase between the dry condition and a P_{H_2O} of 0.5 bar. It appeared to further increase with increasing water partial pressure with the rate of increase

being smaller with higher P_{H_2O} values. In the case of catalyst B, the TOFs could not be calculated at water partial pressures of 1 and 2 bar because the fcc cobalt was not XRD-visible at these conditions and so no fcc cobalt crystallite size could be calculated (see equations 3.20-3.24). The TOF was found to increase between the dry condition and a P_{H_2O} of 0.5 bar, as was the case with catalyst A. The remaining fcc Co made up 30 wt % of the cobalt-containing phases, indicating that the fcc Co present was more active at this water partial pressure.

4.5.2 Selectivity

Selectivity analyses were performed with respect to methane, C_{5+} products, linear olefin formation and isomerisation, and branching, all as functions of water partial pressure.

Chain-growth probabilities were calculated for each FTS condition (figure 4.17).

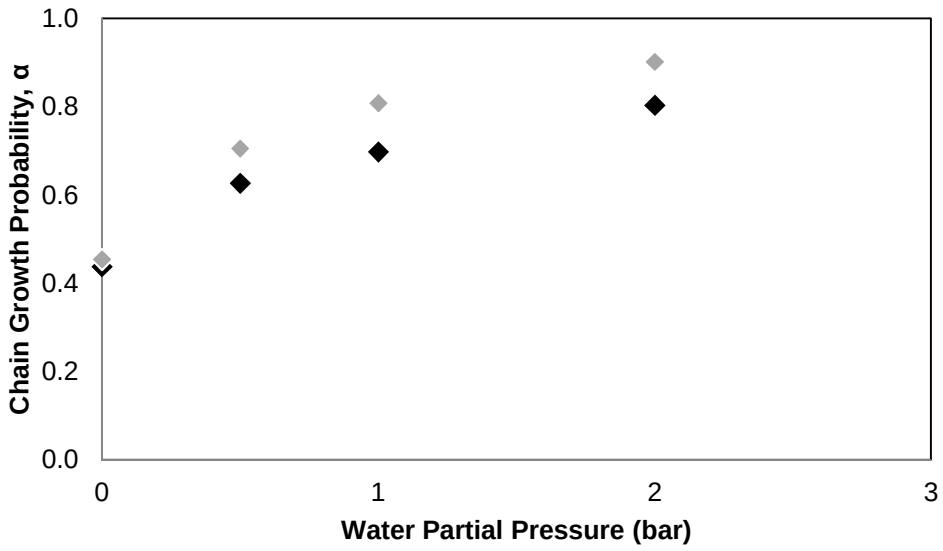

Figure 4.17: Chain-growth probability, α, for FTS runs with catalysts A (◆) and B (◆).

In the cases of both catalysts, chain-growth probabilities increased with increasing water partial pressure. Further discussion about chain-growth probability is made in section 5.5.2.

Methane and C_{5+} selectivities were calculated for each set of FTS runs with each catalyst, the results of which are presented in figure 4.18. Selectivity was calculated as the number of carbon-moles of a certain product or product range per number of carbon-moles in all the carbon-containing products (see section 3.4.2).

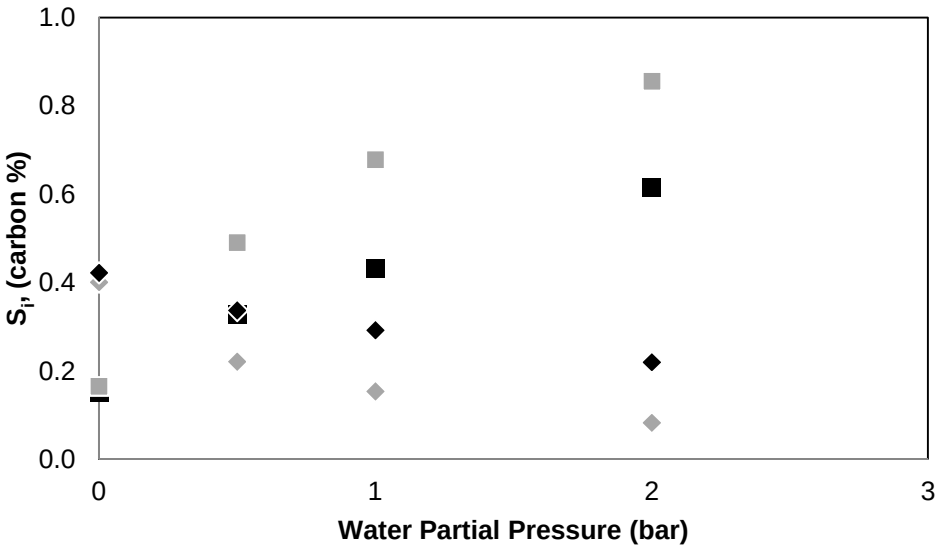

Figure 4.18: Methane (◆, ◆) and C_{5+} (■, ■) selectivities for FTS runs with catalysts A (black) and B (grey).

As was the case with the methane and C_{5+}formation rates, (figure 4.15), in the cases of both catalysts, methane selectivity was the same and C_{5+} selectivity was the same during the dry condition. For both catalysts, methane selectivity decreased and C_{5+} selectivity increased with increasing water partial pressure. In both cases, the greatest change was observed between the dry condition and a water partial pressure of 0.5 bar. In the case of catalyst B, the C_{5+} selectivity was higher and the methane selectivity was lower than their respective values in the case of catalyst A.

Molar olefin fractions of the straight-chain hydrocarbons in product fractions with carbon numbers 2-7 were calculated for each set of FTS runs with each catalyst, the results of which are presented in figure 4.19.

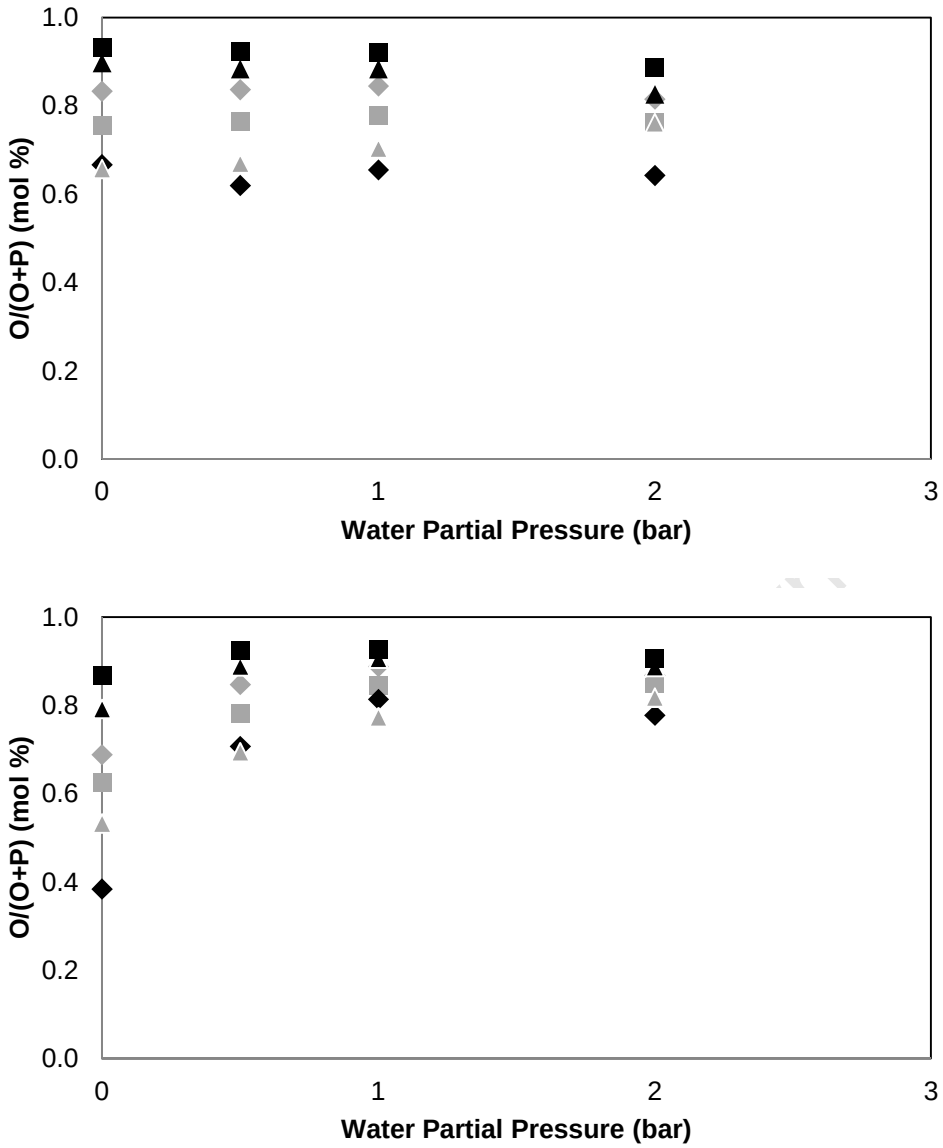

Figure 4.19: Molar olefin fractions of straight-chain hydrocarbons in product fractions with carbon numbers 2 (◆), 3 (■), 4 (▲), 5 (◆), 6 (■) and 7 (▲), in the cases of catalyst A, above, and B, below.

While approximately constant for catalyst A, generally, for catalyst B, molar olefin fractions in the straight-chain hydrocarbon product fractions increased between the dry condition and P_{H_2O} of 0.5 bar, after which they either remained approximately constant or increased with increasing water partial pressure. The olefin fraction decreased with increasing carbon number, with the C_2 fraction being the exception (see discussion in section 5.5.2). A low relative olefin content indicates preferred secondary olefin hydrogenation.

Primary-product, linear olefin fractions (i.e. α-olefins) were calculated by dividing the α-olefin molar-flow-rate by all the linear olefin molar flow-rates (α-olefins and olefins with internal double bonds). This was done for product fractions with carbon numbers 4-7. These results are presented in figure 4.20. This analysis was done to determine the extent of formation of secondary, straight-chain olefins (i.e. straight-chain olefins with internal double bonds), from primary olefins, by double-bond shift.

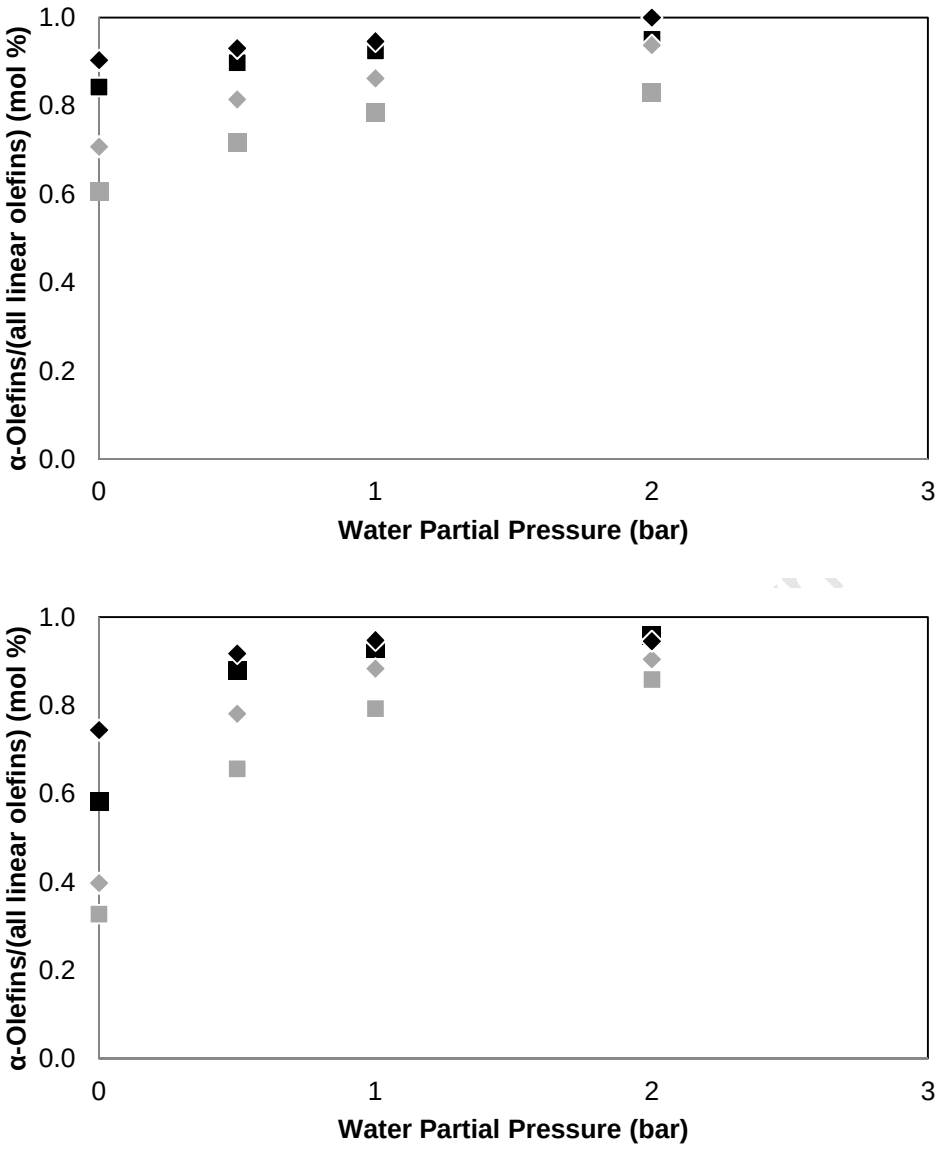

Figure 4.20: α-olefin fractions within straight-chain olefin product fractions with carbon numbers 4 (◆), 5 (■), 6 (◆) and 7 (■), in the cases of catalyst A, above, and B, below.

Generally, in the cases of both catalysts, α-olefin fractions in the straight-chain olefin fractions increased or remained approximately constant with increasing water partial pressure. This indicates that the rate of formation of secondary olefins from primary olefins by double-bond shift decreased with increasing water partial pressure. This trend is again more pronounced for catalyst B. The reasons for the decrease in olefin isomerisation are discussed in section 5.5.2.

The ratio of branched to straight-chain hydrocarbons in the C_5 product fraction was also calculated and is presented in figure 4.21.

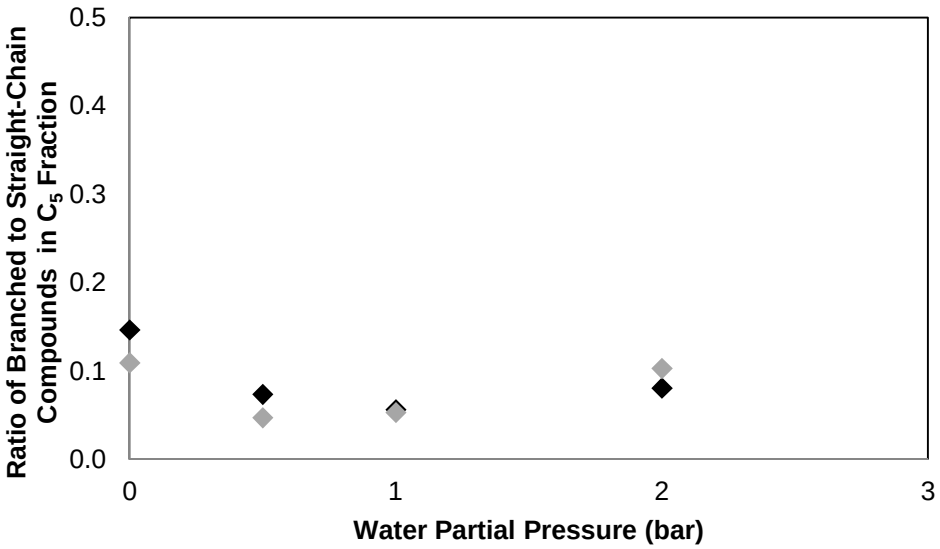

Figure 4.21: Ratio of branched to straight-chain hydrocarbons in the C_5 product fraction, in the cases of catalysts A (◆) and B (◆).

In the cases of both catalysts, the ratio of branched products to straight-chain products decreased with increasing water partial pressure up to a P_{H_2O} of 1 bar (with catalyst A) or 0.5 bar (with catalyst B), after which it remained approximately constant, given the scale.

The results presented in this section are discussed in detail in the following section. In the discussion, the results obtained from the experiments performed with the two catalysts are compared, in conjunction with other research findings.

5 Discussion

In this section, which parallels the previous section, the results obtained are discussed with reference to what has been found by other research groups. The importance of the catalyst synthesis technique employed is highlighted. The commissioning of the *in-situ* XRD cell is discussed with respect to X-ray interference by the borosilicate capillary tube (affecting the XRD results) and the temperature profile of the reaction zone (affecting kinetic analysis and composition during reduction). The results obtained from the *in-situ* XRD analysis during the temperature-programmed reduction and Fischer-Tropsch synthesis experiments are then discussed, with particular interest in the size and oxidation effects and the differences between the results obtained with the two catalysts. Observations made using TEM performed on the spent catalysts, regarding the changes in catalyst composition, are then briefly discussed. Finally, the results of the kinetic analysis, with the focus on catalyst activity and product selectivity, and their differences as functions of crystallite size and water partial pressure, are explained.

5.1 Synthesis and *Ex-Situ* Characterisation of Fresh Catalysts

Two alumina-supported catalyst precursors were synthesised using a reverse micelle technique developed by Fischer (2011), yielding crystallites of narrow size distributions. For a given catalyst precursor, the cobalt nitrate concentration in the aqueous cobalt nitrate solution and the water-to-surfactant ratio were found to affect the resultant crystallite size. In general, the size was found to decrease with decreasing concentration and decreasing water-to-surfactant ratio, with the effect from the latter factor being more significant. These factors are discussed in detail by Fischer (2011).

Industrially-employed catalysts are usually synthesised using precipitation and impregnation methods (Dry, 2002; Schulz *et al*., 2002; Schulz, 1999; Schulz and Claeys, 1999) as these are the most economically feasible, resulting in catalyst crystallites of wide size distributions. The microemulsion method requires high organic phase volumes relative to the mass of catalyst produced, making this method unfeasible for industrial application. In this study, the Co_3O_4 crystallite sizes calculated for catalysts A and B were, respectively, 10.3±1.9 nm and 6.1±1.4 nm (TEM; volume-weighed sizes), as determined from TEM micrographs of the fresh, unsupported catalysts (figure 4.1). Narrow size distributions were obtained for the synthesised model catalysts, as verified by the standard deviations. It is important to study catalysts with crystallites of narrow size distributions so that specific effects, such as activity, selectivity and oxidation by water, can be attributed to particular crystallite sizes, especially with crystallite sizes below 6-8 nm, where Fischer-Tropsch synthesis is a surface-dependent reaction (Fischer, 2011; Bezemer *et al*., 2006), and for smaller sizes (and high water partial pressures) where oxidation by water is expected to occur according to thermodynamics (van Steen *et al*., 2005). Therefore, this particular method of catalyst synthesis was deemed necessary for increased understanding of catalyst effects under reaction conditions.

5.2 Cold Cell Commissioning

The *in-situ* XRD cell consists of many parts, most of which are custom-made and therefore not easily obtainable. The capillary tube, an important section that poses the most challenges (e.g. successfully sealing it against gas leaks), is one such part. In testing various capillary tubes to find the most suitable one to be used, X-ray interference had to be taken into account with respect to material and thickness, given that the maximum X-ray operating voltage was 35 kV. In addition to ensuring adequate signal intensity for *in-situ* XRD studies, the reaction zone had to have a flat temperature profile for accurate kinetic studies. This factor depended on the heaters used, their arrangement and the isothermal nature of the enclosure surrounding the reaction zone. These challenges are discussed below.

5.2.1 X-Ray Interference

The $K\alpha_{average}$ radiation wavelengths of copper and cobalt (the latter being used in the X-ray source in this work) are similar, being 1.54 Å and 1.79 Å, respectively (Bearden, 1967). It is thus assumed that the effects of the studied materials would be comparable in the presence of X-rays generated from either a Cu or a Co source. It is reported that borosilicate has a linear absorption coefficient of 71.0 cm^{-1} and quartz has a linear absorption coefficient of 75.8 cm^{-1} in Cu Kα radiation (Capillary Tube Supplies, 2009). The difference in the absorption was evident from the results obtained from XRD performed on the various capillaries loaded with Y_2O_3. Sample peaks were more clearly observed for the borosilicate capillaries, with the thinnest-wall capillaries (wall thickness of 0.01 mm) providing the optimum result. The borosilicate capillary with a wall thickness of 0.02 mm was chosen for its greater structural integrity while still providing an acceptable result (figure 4.2, black spectrum). The background contribution from the borosilicate phase (figure 4.3) was found to be the largest between 2θ angles of 20-40°. The contribution from the amorphous borosilicate may have been over-estimated at these lower angles, since incident and diffracted X-ray beams have to travel through more material. This is illustrated in figure 5.1. Note the position of X-ray diffraction, illustrated as the over-emphasised gap at the top of the catalyst bed.

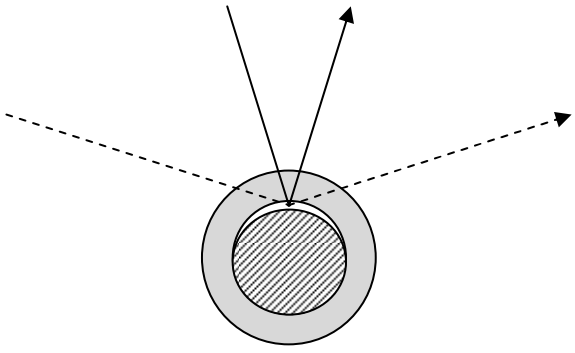

Figure 5.1: Schematic of capillary (grey), in which the catalyst (pattern of black diagonal lines) is loaded, with incident and diffracted X-ray beams at lower angles (dashed lines) and higher angles (solid lines). At lower angles, the X-rays need to travel through more material, increasing the background contribution from the capillary. The fictitious white gap at the top of the catalyst bed, which represents the area visible to the X-rays, is over-emphasised for illustration only.

In figure 4.4 (black spectrum), the background contribution from the borosilicate appeared to be more significant than its contribution in the case of the Y_2O_3 scan (figure 4.2, black spectrum). This was due to the lower intensity of the Co_3O_4 peaks relative to the background contribution from the borosilicate, compared with the relative intensity of the peaks in the case of the Y_2O_3 sample. Because the average Co_3O_4 crystallite size was smaller than that of the Y_2O_3, the peak intensities (that is, the number of counts in absolute numbers) of the Co_3O_4 sample were lower than those in the Y_2O_3 sample. During Rietveld refinement, the background contribution was found to be no problem as TOPAS was able to analyse and subtract it. Additionally, because the scans for the *in-situ* experiments were taken between 2θ angles of 40-90° (as all the major peaks of the cobalt phases are present in that range), the bulk of the background contribution was inherently eliminated.

5.2.2 Temperature Profile of Capillary Reaction Cell

Understanding the temperature profile of the reaction zone is essential, as this directly influences the accuracy of the kinetic studies. In the current *in-situ* XRD cell design, the thermocouple is positioned inside the capillary tube, in the catalyst bed, just outside the X-ray beam path. This setup was considered to be the optimal position for temperature measurement and control.

In figure 4.6 is presented the temperature profile of the capillary reaction cell, generated with the setup of the infrared heaters that was used for the *in-situ* reduction and FTS experiments. Other arrangements were considered, including the adjacent positioning of three infrared heaters (long sides next to each other) and using only one infrared heater below the capillary tube. The end-to-end arrangement (see figure 3.2) was found to produce the flattest temperature profile with a temperature deviation of ±4°C, over the length of the catalyst bed, for the approximate reaction temperature of 220°C. The temperature profile was generated while the inlet and outlet heating zones were not heated. It is therefore expected that smaller temperature deviations were present when the inlet and outlet zones were heated. The measured temperature deviation was considered sufficiently small so that accurate kinetic analysis could be performed, provided the catalyst was placed within this 15 mm-long section in the centre of the capillary (see figure 4.6). Considerations have been made with regard to improvements (see section 7).

5.3 *In-Situ* Reduction and Fischer-Tropsch Experiments

The synthesis of a cobalt catalyst employed in this study entailed the production of the precursor using the reverse micelle technique, its calcination in air, its deposition onto a γ-alumina support, and finally its *in-situ* reduction to the metallic fcc cobalt phase, which is active for Fischer-Tropsch synthesis. At every point throughout this process, it was important that the conditions were understood and controlled to ensure that the obtained catalysts were indeed model catalysts. This is essential so that the information obtained from FTS and the accompanied kinetic experiments is accurate and relevant.

5.3.1 Temperature-Programmed Reduction

In figures 4.7-4.8 are presented the top views and three-dimensional views of the XRD spectra obtained during the *in-situ* temperature-programmed reductions of both catalysts. The reduction of Co_3O_4 via CoO to the essentially-pure fcc Co phase parallels the work by Fischer *et al*. (2011) who found no hcp Co phase to be present after the reduction of model catalysts which were prepared in the same way. They found the fcc phase to be more stable at higher temperatures, which were employed during reduction in their study and the current one. Kitakami *et al*. (1997) reported that the fcc phase is the most stable Co phase for crystallite sizes below 20 nm, above which the hcp phase is more stable in increasing proportions until a crystallite size of 40 nm. Crystallites larger than 40 nm consist predominantly of the hcp phase (Kitakami *et al*., 1997). Saib *et al*. (2006) also found the fcc fraction to increase with decreasing crystallite size, with the sizes of the crystallites being studied being 4 nm (pure fcc) and 28 nm (a mixture of fcc and hcp). These reports were found to be in agreement with the findings of the current study.

Upon the completion of the *in-situ* temperature-programmed reduction of the catalysts, the active phase (i.e. metallic cobalt) for FTS was present. Moreover, the active phase was essentially pure fcc cobalt. This is important because the other metallic cobalt phases (hcp and epsilon) may be active for FTS to differing degrees, and may be oxidised under different conditions. The fcc metallic cobalt crystallite sizes (and their errors) of the freshly-reduced catalysts A and B were calculated, using Rietveld refinement, to be 18.9±5 nm and 4.1±1.9 nm, respectively. These catalysts were thus deemed model catalysts because of their narrow size distributions and the purity of the cobalt phase present.

5.3.2 Fischer-Tropsch Synthesis

In figures 4.9-4.10 are presented the top views and three-dimensional views of the XRD spectra obtained during the *in-situ* Fischer-Tropsch synthesis with both catalysts. Each condition was maintained for 6 hours, which was found to be sufficient to achieve steady-state, according to online GC-TCD analysis (see figure A1 in the appendix A1).

5.3.2.1 Oxidation

With increasing water partial pressure, no composition changes were observed for catalyst A (figure 4.9). Its average crystallite size of about 18 nm (figure 4.11), which was maintained throughout the FTS runs, has been found to be larger than what is thermodynamically feasible for oxidation to occur (van Steen *et al*., 2005), graphically presented in figure 4.12. Saib *et al*. (2006) proposed that larger crystallites are more stable towards oxidation because they are well-faceted and have fewer defects in the crystallite stacking.

The fcc Co phase, of approximate average crystallite size 3.5 nm, present in catalyst B, was found to be partially oxidised to CoO at a P_{H_2O}/P_{H_2} of 0.83 (corresponding to a simulated conversion of 63%, and a P_{H_2O} of 0.5 bar in this study), and completely oxidised to CoO at a P_{H_2O}/P_{H_2} of 1.67 (corresponding to a simulated conversion of 77%, and a P_{H_2O} of 1 bar). These results are in agreement

with thermodynamic calculations (van Steen *et al*., 2005) (figure 4.12). van de Loosdrecht *et al*. (2007) and Bezemer *et al*. (2010) noted that oxidation could not be a deactivation mechanism under the conditions of industrial operation, even for cobalt crystallite sizes smaller than 6 nm because of the low P_{H_2O}/P_{H_2} ratios. van de Loosdrecht acknowledged that, even though their initial, average cobalt crystallite size was 6 nm, the deactivation they observed was probably due to sintering since the activity was seen to decrease even though the extent of reduction increased with time on stream. They monitored the catalyst changes by extracting samples of it from the reactor periodically and analysed them using *ex-situ* techniques, thus introducing passivation difficulties and inhibiting the extent of understanding that could otherwise have been gained from direct, *in-situ* analysis. The results obtained from the present study are from the *in-situ* XRD-visible phases, the part of the catalyst bed where X-rays are diffracted (see figure 5.1). However, the phase changes were distinct upon changing conditions and are therefore considered to be representative of all the catalyst material present. The remaining cobalt phase, evident from the non-zero FT formation rates (figure 4.14), was present in decreasing proportions with increasing water partial pressure (see discussion in section 5.5.1).

5.3.2.2 Size Analysis

Crystallite size did not change much in the case of both catalysts. The most significant change was observed in the case of catalyst A, where the fcc cobalt crystallite size appeared to grow from about 13.9 nm to 18.9 nm during the reduction (figure 4.11). Over all the reduction and FTS experiments with catalyst A, however, the average cobalt crystallite size was 16.3 nm, indicating negligible change, given the associated calculation errors. Sintering can occur as there are only weak metal-support interactions, resulting in a loss of surface area through crystallite growth. Generally, the sintering of supported metal catalysts occurs to a greater extent above 500°C and is promoted by the presence of water vapour (Bartholomew, 2001; Jacobs *et al*., 2002). This, however, is specific to and different for each metal and support material. The high reduction temperature of 450°C, as well as the elevated water concentration during reduction, may have been conducive for sintering to occur. Where the crystallites are larger than the support pore diameter (d_{pore} = 11.5 nm in this study) the metal-support interactions are further weakened (Fischer *et al*., 2011), thus making sintering easier in the case of catalyst A. However, the crystallite size did not change significantly so that sintering was not observed to a great degree. The fcc cobalt crystallite size was consistently larger than the CoO size. It is possible that the CoO was reduced in such a way that an outside metallic shell formed, with the inner layers of cobalt oxide being reduced to metallic cobalt, resulting in a decrease in the CoO crystallite size and an increase in the fcc cobalt crystallite. This inner oxide core (if this was the case) may then have remained, explaining the presence of the CoO throughout the FTS runs. In the cases of both catalysts, no sintering of the metallic or oxide phases was observed throughout the FTS experiments (figure 4.11). This may be a function of the limited time on stream, minimising excessive exposure to the elevated water concentrations.

In the case of catalyst B, during reduction an apparent decrease in the CoO crystallite size was observed before the formation of the fcc cobalt, which, after being identified by XRD analysis, appeared to increase slightly in crystallite size. The metallic size is expected to be smaller than the

oxide size because of the difference in structure size due to the differences in molar volume (the oxide includes metal and oxygen atoms). After this apparent increase, no further size changes were observed. The lower cobalt loading in the case of catalyst B may have inhibited sintering due to the cobalt crystallites being diluted to a greater extent in the metal-support mixture.

5.4 *Ex-Situ* Characterisation of Spent Catalysts

It was generally difficult to distinguish between cobalt and alumina phases using TEM micrographs, possibly due to the presence of a wax coating and the similarity of the appearance of the phases. Note that the size distributions for the fresh catalysts were determined from TEM micrographs of unsupported samples. Cobalt-alumina complexes ("aluminates"), that may have formed upon water co-feeding, are even more difficult to identify and sometimes indistinguishable from alumina due to the very small differences in d-spacings. Due to these difficulties, an insufficiently small number of cobalt crystallite sizes was obtained in order to calculate size distributions. However, sizes of a number of cobalt crystallites, identified using high-resolution TEM in conjunction with energy-dispersive X-ray spectroscopy (EDX), were in agreement with sizes calculated from the XRD spectra. In the top-left and bottom two images of figure 4.13, needle-like crystallites are observed, which may be Boehmite, an AlO(OH) phase, formed upon exposure to high steam concentrations (Tsakoumis *et al*., 2010). However, this phase was not observed in the XRD characterisation, possibly because the amount of this phase was too low or it was not sufficiently crystalline.

5.5 Kinetic Analysis

5.5.1 Activity

Under dry FT conditions, both catalysts were found to have the same FT formation rate of about 8 x 10^{-6} carbon moles per second (per gram of respective catalyst). But as the water partial pressure increased, the formation rate in the case of catalyst A increased while in the case of catalyst B it remained constant (figure 4.14). At a water partial pressure of 2 bar, the formation rate (per gram of respective catalyst) in the case of catalyst A was almost 4 times larger than the formation rate with catalyst B. It must be noted that, in the case of catalyst B, while metallic cobalt was no longer XRD-visible at water partial pressures of 1-2 bar, there must have been a fraction of metallic cobalt remaining to catalyse FTS. The remaining metallic cobalt in catalyst B at a water partial pressure of 0.5 bar was calculated to be 30 wt % of the cobalt-containing compounds (balance CoO).

A number of research groups (Storsæter *et al*., 2005; Hilmen *et al*., 1999) found that co-feeding water with syngas under FTS conditions resulted in a decrease in the FT formation rate over γ-alumina-supported cobalt catalysts, while the formation rate has been found to increase over silica- and titania-supported cobalt catalysts (Krishnamoorthy *et al*., 2002; Bertole *et al*., 2002). Lögdberg *et al*. (2011) found the FT formation rate to increase upon the co-feeding of water over a γ-alumina-supported cobalt catalyst. The difference in results found by other research groups may be a result of the

differences in the physical characteristics of the supports as well as the particular crystallite sizes and therefore metal-support interactions. The apparently constant rate of formation of FT products in the case of catalyst B, with increasing water partial pressure, may be attributed to a combination of enhanced activity of the active FT sites, by water presence, along with deactivation of the catalyst. At the higher water partial pressures (1-2 bar) the cobalt metallic phase was no longer XRD-visible. It is thus suggested that the constant formation rate was due to catalyst deactivation by oxidation coupled with enhanced activity at elevated water concentrations. Bertole *et al*. (2002) found that water addition resulted in an increased rate of carbon monoxide activation and an increase in the surface coverage of active carbon without an overall increase in the reactivity of active carbon. They speculated that the increase in CO reactivity could arise from a direct interaction between co-adsorbed CO and water which results in a lowering of the energy barrier for CO dissociation. Schulz *et al.* (1997) noted that water could affect elemental reaction steps, affecting both activity and selectivity. Lögdberg *et al*. considered the increase in FT formation rate to be a result of a positive adjustment to the kinetics of active FT sites, with this kinetic modification being applicable also to the changes in selectivity observed (Schulz *et al*., 1997).

In the case of catalyst A, with increasing water partial pressure, a greater rate of increase in formation rate of the C_{5+} products was observed than for that of the methane formation rate. In accordance with the overall FT rate increasing with increasing water partial pressure, the formation rates for both groups of products increased. This trend of the FT rate increasing with increasing water partial pressure has been found by other research groups in the cases of both cobalt and ruthenium catalysts (Claeys & van Steen, 2002; van Steen & Schulz, 1999). Lögdberg *et al*. (2011) claimed that the addition of co-fed water enhanced the activity of sites active for FTS and that "pure methanation" sites may develop upon exposure to co-fed water, possibly explaining the increase in the methane formation rate. However, it is possible that the increase in the methane formation rate is simply because all product formation rates increased due to enhanced activity of active sites with increasing water partial pressure. Claeys & van Steen (2002) noted that an increase in water partial pressure would result in a decrease in surface carbon being present, which has been considered to inhibit the FT reaction. They also noted that an increased water partial pressure results in an increased availability of surface hydrogen, allowing the CH_x and intermediate alkyl species to be more readily formed (from surface carbon), which can in turn result in increased chain-growth probability and selectivity towards C_{5+} compounds. The selectivity to C_{5+} compounds is favoured over methane with increasing water partial pressure (see section 5.5.2) and it is understood that all sites active for CO hydrogenation are enhanced in the presence of elevated water concentrations, with those for chain growth experiencing the greatest kinetic advantage. In the case of catalyst B, in accordance with what has been found with increasing water partial pressures (Lögdberg *et al*., 2011; Claeys & van Steen, 2002; van Steen & Schultz, 1999; Schulz *et al*., 1997), methane formation rate decreased, while C_{5+} formation rate increased.

Turnover frequencies were calculated for both catalysts (figure 4.16). In accordance with the aforementioned discussion about the positive effect water has on FT formation rate, the TOF in the case of catalyst A was found to increase with increasing water partial pressure, with the greatest

increase between the dry condition and a P_{H_2O} of 0.5 bar. With further increases in water partial pressure, the rate of increase in the TOF was smaller. Iglesia (1997) noted that water addition initially increases the FT rate, but with further water concentration increases, the rates and selectivities are much more weakly affected. Claeys & van Steen (2002) noted that at higher water partial pressures, the elevated activity may result in a severe depletion of surface carbon, slowing down the reaction rate. The TOF also increased in the case of catalyst B, for the two instances where it could be calculated. The remaining cobalt present was calculated, from Rietveld refinement, to be 30 wt % of the cobalt-containing compounds. The increase in activity can be attributed to the significant positive effect of water on the active sites such that an overall increase was observed, even while 70 wt % of the cobalt was in the form of the inactive cobalt oxide phase. As for the approximately constant FT formation rate with increasing water partial pressure, the metallic cobalt was no longer XRD-visible for a P_{H_2O} of 1-2 bar, indicating that the remaining metallic phase was present in a decreasing proportion with increasing water partial pressure, thus leaving a decreasing number of active FT sites available for CO hydrogenation.

5.5.2 Selectivity

Chain-growth probabilities were calculated for each FTS condition for each catalyst (figure 4.17). They were found to increase significantly (in the case of catalyst A, from 0.44 to 0.80 and in the case of catalyst B, from 0.45 to 0.90) with increasing water partial pressure. An increasing trend was also found by other research groups (Lögdberg *et al*., 2011; Bertole *et al*., 2002; Iglesia, 1997; Schulz *et al*., 1997). In each case, the other research groups also found, upon addition of co-fed water, that methane selectivity decreased and C_{5+} selectivity increased. These trends were also observed in the present study for FTS with both catalysts (figure 4.18). Methane selectivity is coupled with C_{5+} selectivity, in that the propagation of the C_1 species, which is favoured at elevated water concentrations, occurs at the expense of its hydrogenation to methane (Lögdberg *et al*., 2011; Storsæter *et al.*, 2005). As was the case with the activity being the same for both catalysts under dry FTS conditions, the selectivity to methane (41 C %) and the selectivity to C_{5+} products (16 C %) were also the same for both catalysts under dry FTS conditions. With increasing water partial pressure, in the case of catalyst B, methane selectivity decreased to 8 C % and C_{5+} selectivity increased to 87 C %. This is far more favourable than the case with catalyst A, where methane selectivity decreased to only 22 C % and C_{5+} selectivity increased to only 62 C %. But due to the higher overall FT formation rate, catalyst A catalysed the formation of almost 3 times more C_{5+} products and almost 10 times more methane (on a carbon-mole basis and per gram of respective catalyst) than did catalyst B (figure 4.15).

The molar olefin contents of the C_2-C_7 straight-chain hydrocarbons were found to either remain approximately constant (catalysts A and B) or increase with increasing water partial pressure (catalyst B) (figure 4.19), with the latter effect indicating suppressed secondary hydrogenation at higher water partial pressures. Schulz *et al*. (1997) found secondary hydrogenation of olefins to be inhibited at high water concentrations. Generally, a higher straight-chain olefin content was found in the case of catalyst A for water partial pressures 0-0.5 bar (between 62-92% for A and between 38-93% for B),

with the olefin content being higher in the case of catalyst B for water partial pressures of 1-2 bar (between 64-88% for A and between 78-91% for B). Other research groups also found olefin fractions to increase with increasing water partial pressure (Bertole *et al*., 2002; Schulz *et al.*, 1997; Iglesia, 1997). In this study, as was also found by Bertole *et al*. (2002), the olefin fractions were found to decrease with increasing carbon number (most clearly visible in the case of catalyst B), with the C_2-olefin fraction (ethylene) being an outlier compared with the other carbon-number fractions, as this fraction is readily hydrogenated and incorporated into chain-growth at elevated water concentrations, or may act as a chain initiator (Iglesia *et al*., 1993). The largest effect (except in the case of the C_2-olefin fraction) was observed in the case of the C_7-olefin fraction, especially between the dry condition and a P_{H_2O} of 0.5 bar.

The primary olefin fraction in the straight-chain olefin content was also calculated (figure 4.20). Generally, an increase in the primary olefin fraction was observed with increasing water partial pressure. In the case of catalyst A, the primary product olefin fraction was higher than in the case of catalyst B for water partial pressures of 0-0.5 bar (between 60-93% for A and between 33-92% for B). At water partial pressures of 1-2 bar, both catalysts exhibited similar primary olefin fractions. Schulz *et al.* (1997) noted that the increase in the primary olefin fraction was coupled with the decrease in olefins with internal double bonds with increasing water partial pressure, in that water inhibited secondary olefin isomerisation by double-bond shift, reducing the content of secondary olefins produced.

The ratio of all branched to all straight-chain compounds for the C_5 product fraction was calculated (figure 4.21), with this product fraction being representative of all the product fractions. Generally, this ratio is low (between 0.05 and 0.15 for both catalysts), attributed to the spatial constraints that favour straight-chain product growth over branched product growth (Schulz, 2003). In the cases of both catalysts, a decrease in this ratio with increasing water partial pressure up to a P_{H_2O} of 1 bar (with catalyst A) or 0.5 bar (with catalyst B) was observed, after which it remained approximately constant, given the scale. The observed decrease in the branching ratio in the present study is attributed to inhibited isomerisation of primary olefins to secondary olefins by double-bond shift with increasing water partial pressure (figure 4.20) (Schulz *et al*., 1997), most significantly between the dry condition and a P_{H_2O} of 0.5 bar (corresponding to a high P_{H_2O}/P_{H_2} ratio of 0.83).

In the next section, these findings are concluded, within the categories of the *in-situ* XRD and kinetic results.

6 Conclusions

A novel *in-situ* XRD cell has successfully been developed for the characterisation of Fischer-Tropsch and other heterogeneous catalysts under reaction conditions, up to 500°C and 25 bar with a reactor consisting of a borosilicate capillary of wall thickness 0.02 mm. The cell design is such that other capillaries of 1 or 2 mm outer diameter, and with thicker walls (depending on XRD instrument operating energy), can easily be installed without changes to the cell required. The design also facilitates the co-feeding of water at a wide range of partial pressures (only a small range was examined in the current study) by a saturator system, the heating of which is controlled via a programmable temperature controller. The *in-situ* cell is the first of its kind that can easily be installed on any laboratory-scale X-ray diffractometer or synchrotron facility, making its use widely transferrable. The design also incorporates an internal thermocouple for accurate kinetic analysis.

With regard to the *in-situ* temperature-programmed reduction results, in the cases of both catalysts, the reduction of Co_3O_4 to CoO was clearly observed. The further reduction of CoO to Co was also clearly observed, with the metallic Co being essentially pure fcc. The catalyst with the larger crystallites was found to be reduced to CoO and subsequently to Co at the temperatures of 350°C and 450°C, respectively, with a small fraction of CoO remaining in the reduced catalyst. The catalyst with the smaller crystallites was found to be more easily reducible, being reduced to CoO and Co at the temperatures of 200°C and 370°C, respectively. The fcc cobalt crystallite sizes of 18.9±5 nm and 4.1±1.9 nm for catalysts A and B, respectively, in addition to the purity of the Co phase (i.e. fcc only), ensured that model catalysts had indeed been synthesised.

With regard to the *in-situ* XRD FTS results, in agreement with thermodynamics, oxidation of cobalt under FTS conditions has been found, by direct observation, to be a function of cobalt crystallite size and the P_{H_2O}/P_{H_2} ratio (that is, simulated syngas conversion). No oxidation was observed for the catalyst with a crystallite size of 18.9±5 nm, for a simulated conversion up to 91% (corresponding to a P_{H_2O}/P_{H_2} ratio of 5 and a P_{H_2O} of 3 bar). However, for the first time, oxidation has been directly observed, and this in the case of the catalyst with a crystallite size of 4.1±1.9 nm. In the case of the catalyst with the smaller crystallites, oxidation was initially observed at a simulated conversion of 63% (corresponding to a P_{H_2O}/P_{H_2} ratio of 0.83 and a P_{H_2O} of 0.5 bar), and complete oxidation was observed for a simulated conversion of 77% (corresponding to a P_{H_2O}/P_{H_2} ratio of 1.67 and a P_{H_2O} of 1 bar).

In the cases of both catalysts, with increasing water partial pressure, methane selectivity was suppressed, chain-growth enhanced and the activity of active FT sites improved. Even though FT formation rates were identical for both catalysts under dry FT conditions, activity (turnover frequency) was greatly enhanced in both cases upon the addition of co-fed water. In the case of catalyst A, the FT formation rate at a P_{H_2O} of 2 bar was about 4 times larger than the FT formation rate

with catalyst B. With both catalysts, activity was enhanced to the greatest degree between the dry condition and a P_{H_2O} of 0.5 bar. In the case of catalyst A, for P_{H_2O} values above 0.5 bar, the rate of increase in activity became smaller with increasing water partial pressure. In the case of catalyst B, FT formation rate remained approximately constant for each condition, which was considered to be a result of enhanced activity of active sites coupled with deactivation of the catalyst by oxidation, in agreement with the *in-situ* XRD results.

Chain-growth probability increased to a greater degree in the case of catalyst B (0.45-0.90) than it did with catalyst A (0.44-0.80) with increasing water partial pressure. In the case of catalyst B, C_{5+} selectivity (increased from 16 to 87 C %) and methane selectivity (decreased from 41 to 8 C %) followed more economically-attractive trends than did their counterparts in the case of catalyst A (C_{5+} selectivity increased from 16 to 62 C % and methane selectivity decreased from 41 to 22 C %). However, due to the higher overall FT formation rate, catalyst A catalysed the formation of almost 3 times more C_{5+} products and almost 10 times more methane than did catalyst B (on a carbon-mole basis and per gram of respective catalyst).

Straight-chain molar olefin fractions either increased or remained approximately constant with increasing water partial pressure, with an increase in water partial pressure (especially between the dry condition and a P_{H_2O} of 0.5 bar) being found to inhibit both olefin hydrogenation and isomerisation. The olefin fractions were generally higher in the case of catalyst A at water partial pressures of 0-0.5 bar, and higher in the case of catalyst B for water partial pressures of 1-2 bar. Similarly, the primary olefin fractions were higher in the case of catalyst A at water partials pressures 0-0.5 bar, and higher in the case of catalyst B for water partial pressures 1-2 bar. The increase in the primary olefin fractions with increasing water partial pressure is in agreement with a decrease in the branching ratio for the C_5 product fraction between the dry FTS condition and a P_{H_2O} of 0.5 bar. This result is attributed to inhibited isomerisation of primary olefins to secondary olefins at elevated water concentrations.

7 Recommendations

In-Situ XRD Cell

The background contribution from the borosilicate capillaries, coupled with the short scan times of 16.5 minutes (therefore decreasing intensity), is such that, while cobalt and alumina phases could be easily identified, size analysis by either Rietveld refinement or the Scherrer equation is not always easy. Two sets of polyimide capillary tubes were considered as reaction vessels. The first set (IWGHPC, USA) was thermally stable in hydrogen at reduction temperatures, but not thermally stable in air at reaction temperatures and so no further tests were conducted. The second set (Cole-Parmer Instrument Company, UK, supplied by Laboratory Consumables & Chemical Supplies, RSA), had higher temperature ratings but lacked structural strength when fitted into the cell, resulting in gas leaks. Therefore, it is recommended that polyimide capillary tubes be investigated further, with structural enhancements around the fittings, in the form of internal supports (e.g. short glass capillary tubes inside the polyimide tubes, where the fittings are) or external modification to the fittings.

The second-generation cell has been designed with a thermocouple support plate and new fittings. The new fittings, manufactured from silicone, apply less stress to the capillary, making higher operating pressures possible (without having to tighten the fitting as much to prevent gas leaks). These may also permit the successful operation of the aforementioned polyimide tubing with the higher temperature rating. Therefore, it is recommended that this newly-designed cell be thoroughly tested, with the emphasis on gas-tight operation and the use of polyimide capillaries. The new fittings must be tested for thermal rating and lifespan. It is also recommended, upon successful testing of the second-generation cell, that areas be identified for further improvements and potential value-addition. These may include the reduction in size of the thermocouple support plate to reduce lateral movement (to ensure that the reaction cell remains perfectly stationary in the X-ray beam path); potential heat barriers between the infrared heaters and the fittings to prolong fitting life; quick-connecting reactor feed and effluent lines for operational versatility; a thermocouple of smaller diameter to better-approximate plug-flow conditions; a single, longer, infrared heater, ideally without the use of a transformer for a smaller external space requirement, for a better temperature profile; and, if possible, an online GC-TCD be fitted directly after the reactor exit for better kinetic analysis.

It is recommended that the newly-developed *in-situ* XRD cell be used for other heterogeneous catalytic applications which require direct observation of phase changes under reaction conditions.

Oxidation under FTS Conditions

A threshold value with a certain P_{H_2O}/P_{H_2} ratio (or simulated syngas conversion) and fcc cobalt crystallite size has been established, beyond which (smaller crystallite sizes at a constant P_{H_2O}/P_{H_2} ratio or higher P_{H_2O}/P_{H_2} ratios at a constant crystallite size) oxidation is expected to occur. It is recommended that further experiments with small cobalt crystallite sizes and varying P_{H_2O}/P_{H_2} ratios be conducted using the *in-situ* XRD cell, possibly with accompanying *in-situ* magnetic experiments, to establish the boundary for the FTS conditions under which cobalt will be oxidised. These results can then be compared with thermodynamics. Further studies could be performed to determine the reversibility of the oxidation of small cobalt crystallites under FTS conditions.

In accordance with industrial FTS, higher syngas pressures should be tested. Experiments could also be performed for other known cobalt phases, such as hcp and epsilon, with interest in oxidation and kinetic effects. Further studies could also be performed with other industrially-relevant supports, in addition to an inert support, such as carbon nanotubes, and in the absence of a support.

References

Barkhuizen, D., Mabaso, I., Viljoen, E., Welker, C., Claeys, M., van Steen, E. & Fletcher, J.C.Q., 2006. Experimental Approaches to the Preparation of Supported Metal Nanoparticles. *Pure Appl. Chem.*, 78(9), pp.1759-69.

Bartholomew, C.H., 2001. Mechanisms of Catalyst Deactivation. *Applied Catalysis A: General*, 212, pp.17-60.

Bartholomew, C.H. & Reuel, R.C., 1985. Cobalt-Support Interactions: Their Effects on Adsorption and CO Hydrogenation Activity and Selectivity Properties. *Ind. Eng. Chem. Prod. Res. Dev.*, 24, pp.56-61.

Bearden, J.A., 1967. X-ray Wavelengths. *Reviews of Modern Physics*, 39(1), pp.78-124.

Bezemer, G.L., Bitter, J.H., Kuipers, H.P., Oosterbeek, H., Holewijn, J.E., Xu, X., Kapteijn, F., van Dillen, A.J. & de Jong, K.P., 2006. Cobalt Particle Size Effects in the Fischer-Tropsch Reaction Studied with Carbon Nanofiber Supported Catalysts. *J. Am. Chem. Soc.*, 128, pp.3956-64.

Bezemer, G.L., Radstake, P.B., Koot, V., van Dillen, A.J., Geus, J.W. & de Jong, K.P., 2006. Preparation of Fischer-Tropsch Cobalt Catalysts Supported on Carbon Nanofibers and Silica using Homogenous Deposition-Precipitation. *Journal of Catalysis*, 237, pp.291-302.

Bezemer, G.L., Remans, T.J., van Bavel, A.P. & Dugulan, I., 2010. Direct Evidence of Water-Assisted Sintering of Cobalt on Carbon Nanofiber Catalysts during Simulated Fischer-Tropsch Conditions Revealed with *In Situ* Mossbauer Spectroscopy. *J. Am. Chem. Soc.*, 132, pp.8540-41.

Boerrigter, H. & van der Drift, A., 2004. *Larger-Scale Production of Fischer-Tropsch Diesel from Biomass*. Wolfsburg, Germany: ECN Congress on Synthetic Biofuels - Technologies, Potentials, Prospects.

Bruker AXS, 2010. *D8 Advance*. [Online] Available at: http://www.bruker-axs.com/d8_advance.html [Accessed 4 March 2010].

Capillary Tube Supplies, 2009. *Glass Specification*. [Online] Available at: http://www.capillarytubes.co.uk/acatalog/Glass_Specification.html [Accessed 4 February 2011].

Claeys, M. & van Steen, E., 2002. On the Effect of Water During Fischer–Tropsch Synthesis with a Ruthenium Catalyst. *Catalysis Today*, 71, p.419–427.

Claeys, M. & van Steen, E., 2004. Chapter 8 Basic Studies. In A. Steynberg & M. Dry, eds. *Fischer-Tropsch Technology*. Amsterdam: Elsevier, B. V. pp.601-80.

Clausen, B.S., Steffensen, G., Fabius, B., Villadsen, J., Feidenhans'l, R. & Topsøe, H., 1991. *In Situ* Cell for Combined XRD and On-line Catalysis Tests: Studies of Cu-based Water Gas Shift and Methanol Catalysts. *Journal of Catalysis*, 132, pp.524-35.

den Breejen, J.P., Radstake, P.B., Bezemer, G.L., Bitter, J.H., Froseth, V., Holmen, A. & de Jong, K.P., 2009. On the Origin of the Cobalt Particle Size Effects in Fischer-Tropsch Catalysis. *Journal of American Chemical Society*, 131, pp.7197-203.

den Breejen, J.P., Sietsma, J.R.A., Friedrich, H., Bitter, J.H. & de Jong, K.P., 2010. Design of Supported Cobalt Catalysts with Maximum Activity for the Fischer-Tropsch Synthesis. *Journal of Catalysis*, 270, pp.146-52.

Druyts, F. & van Iseghem, P., 2001. Thermogravimetric Analysis of the Beryllium/Steam Reaction. *Fusion Engineering and Design*, 51-52, pp.499-503.

Dry, M.E., 1996. Practical and Theoretical Aspects of the Catalytic Fischer-Tropsch Process. *Applied Catalysis A: General*, 138, pp.319-44.

Dry, M.E., 2002. The Fischer-Tropsch Process: 1950-2000. *Catalysis Today*, 71, pp.227-41.

Dry, M.E., 2004. Chapter 3: Chemical Concepts used for Engineering Purposes. In A. Steynberg & M. Dry, eds. *Studies in Surface Science and Catalysis, 152, Fischer Tropsch Technology*. Amsterdam: Elsevier B. V. pp.196-257.

Dry, M.E., 2004. Chapter 7: FT Catalysts. In A. Steynberg & M. Dry, eds. *Studies in Surface Science and Catalysis, 152, Fischer Tropsch Technology*. Amsterdam: Elsevier B. V. pp.533-600.

Fischer, N., 2011. *Preparation of Nano and Ångstrøm Sized Cobalt Ensembles and their Performance in the Fischer-Tropsch Synthesis*. PhD Thesis, Department of Chemical Engineering, University of Cape Town.

Fischer, N., van Steen, E. & Claeys, M., 2011. Preparation of Supported Nano-Sized Cobalt Oxide and fcc Cobalt Crystallites. *Catalysis Today*, 171, pp.174-79.

Geerlings, J.J.C., Wilson, J.H., Kramer, G.J., Kuipers, H.P.C.E., Hoek, A. & Huisman, H.M., 1999. Fischer-Tropsch Technology - From Active Site to Commercial Process. *Applied Catalysis A: General*, 186, pp.27-40.

Grunwaldt, J.-D., Caravati, M., Hannemann, S. & Baiker, A., 2004. X-Ray Absorption Spectroscopy under Reaction Conditions: Suitability of Different Reaction Cells for Combined Catalyst Characterisation and Time-Resolved Studies. *Phys. Chem. Chem. Phys.*, 6, pp.3037-47.

Hilmen, A.M., Schanke, D., Hanssen, K.F. & Holmen, A., 1999. Study of the Effect of Water on Alumina Supported Cobalt Fischer-Tropsch Catalysts. *Applied Catalysis A: General 186*, pp.169-88.

Iglesia, E., 1997. Design, Synthesis and Use of Cobalt-Based Fischer-Tropsch Synthesis Catalysts. *Applied Catalysis A: General*, 161, pp.59-78.

Iglesia, E., Reyes, S., Madon, R. & Soled, S., 1993. Selectivity Control and Catalyst Design in the Fischer-Tropsch Synthesis: Sites, Pellets, and Reactors. *Advances in Catalysis*, 39, pp.221-302.

Jacobs, G., Patterson, P.M., Zhang, Y., Das, T., Li, J. & Davis, B.H., 2002. Fischer-Tropsch Synthesis: Deactivation of Noble Metal-Promoted Co/Al_2O_3 Catalysts. *Applied Catalysis A: General*, 233, pp.215-26.

Jean-Marie, A., Griboval-Constant, A., Khodakov, A.Y. & Diehl, F., 2009. Cobalt Supported on Alumina and Silica-Doped Alumina: Catalyst Structure and Catalytic Performance in Fischer-Tropsch Synthesis. *C. R. Chimie*, 12, pp.660-67.

Jensen, T.R., Nielsen, T.K., Filinchuk, Y., Jorgensen, J.-E., Cerenius, Y., Gray, E.M. & Webb, C.J., 2010. Versatile *In Situ* Powder X-Ray Diffraction Cells for Solid-Gas Investigations. *Applied Crystallography*, 43, pp.1456-63.

Karaca, H., Hong, J., Fongarland, P., Roussel, P., Griboval-Constant, A., Lacroix, M., Hortmann, K., Safonova, O.V. & Khodakov, A.Y., 2009. *In-Situ* XRD Investigation of the Evolution of Alumina-

Supported Cobalt Catalysts under Realistic Conditions of Fischer-Tropsch Synthesis. *The Royal Society of Chemistry*.

Khodakov, A.Y., 2009. Fischer-Tropsch Synthesis: Relations Between Structure of Cobalt Catalysts and their Catalytic Performance. *Catalysis Today*, 144, pp.251-57.

Khodakov, A.Y., Chu, W. & Fongarland, P., 2007. Advances in the Development of Novel Cobalt Fischer-Tropsch Catalysts for Synthesis of Long-Chain Hydrocarbons and Clean Fuels. *Chem. Rev.*, 107, pp.1692-744.

Kiss, G., Kliewer, C.E., DeMartin, G.J., Culross, C.C. & Baumgartner, J.E., 2003. Hydrothermal Deactivation of Silica-Supported Cobalt Catalysts in Fischer-Tropsch Synthesis. *Journal of Catalysis*, 217, pp.127-40.

Kitakami, O., Sato, H., Shimada, Y., Sato, F. & Tanaka, M., 1997. Size Effect on the Crystal Phase of Cobalt Fine Particles. *Physical Review B (Condensed Matter)*, 56(21), pp.13849-54.

Krishnamoorthy, S., Tu, M., Ojeda, M.P., Pinna, D. & Iglesia, E., 2002. An Investigation of the Effects of Water on Rate and Selectivity for the Fischer-Tropsch Synthesis on Cobalt-Based Catalysts. *Journal of Catalysis*, 211, pp.422-33.

Li, S., Meitzner, G.D. & Iglesia, E., 2001. Structure and Site Evolution of Iron Oxide Catalyst Precursors During the Fischer-Tropsch Synthesis. *Journal of Physical Chemistry B*, 105, pp.5743-50.

Lögdberg, S., Boutonnet, M., Walmsley, J.C., Järås, S., Holmen, A. & Blekkan, E.A., 2011. Effect of Water on the Space-Time Yield of Different Supported Sobalt Catalysts During Fischer-Tropsch Synthesis. *Applied Catalysis A: General*, 393, pp.109-21.

Ma, W., Jacobs, G., Sparks, D.E., Gnanamani, M.K., Pendyala, V.R.R., Yen, C.H., Klettlinger, J.L.S., Tomsik, T.M. & Davis, B.H., 2011. Fischer–Tropsch Synthesis: Support and Cobalt Cluster Size Effects on Kinetics over Co/Al_2O_3 and Co/SiO_2 Catalysts. *Fuel*, 90, pp.756-65.

Mansker, L.D., Jin, Y., Bukur, D.B. & Datye, A.K., 1999. Characterisation of Slurry Phase Iron Catalysts for Fischer-Tropsch Synthesis. *Applied Catalysis A: General*, 186, pp.277-96.

Moggridge, G.D., Rayment, T. & Lambert, R.M., 1992. An *In Situ* XRD Investigation of Singly and Doubly Promoted Manganese Oxide Methane Coupling Catalysts. *Journal of Catalysis*, 134, pp.242-52.

Moodley, D.J., van de Loosdrecht, J., Saib, A.M., Overett, M.J., Datye, A.K. & Niemantsverdriet, J.W., 2009. Carbon Deposition as a Deactivation Mechanism of Cobalt-Based Fischer-Tropsch Synthesis Catalysts under Realistic Conditions. *Applied Catalysis A: General*, 354, pp.102-10.

Mungwe, N., 2012. *CO Hydrogenation Based on Rhodium Crystallites and Clusters of Different Sizes*. PhD Thesis, Department of Chemical Engineering, University of Cape Town.

Ojeda, M., Rojas, S., Boutonnet, M., Pérez-Alonso, F.J., Garcia-Garcia, F.J. & Fierro, J.L.G., 2004. Synthesis of Rh Nano-Particles by the Microemulsion Technology. Particle Size Effect on the CO + H_2 Reaction. *Applied Catalysis A: General*, 274, pp.33-41.

Okabe, K., Xiaohong, L., Mingdeng, W. & Arakawa, H., 2004. Fischer-Tropsch Synthesis over Co-SiO_2 Catalysts Prepared by the Sol-Gel Method. *Catalysis Today*, 89, pp.431-38.

Overett, M.J., Breedt, B., du Plessis, E., Erasmus, W. & van de Loosdrecht, J., 2008. Sintering as a Deactivation Mechanism for an Alumina-Supported Cobalt Fischer-Tropsch Synthesis Catalyst. *American Chemical Society Division of Petroleum Chemistry* , 53(2), pp.126-28.

Panpranot, J., Goodwin Jr, J.G. & Sayari, A., 2002. Synthesis and Characteristics of MCM-41 Supported CoRu Catalysts. *Catalysis Today*, 77, pp.269-84.

Ponec, V. & van Barneveld, W.A., 1979. The Role of Chemisorption in Fischer-Tropsch Synthesis. *Ind. Eng. Chem. Prod. Res. Dev.*, 18(4), pp.268-71.

Prieto, G., Martinez, A., Concepcion, P. & Moreno-Tost, R., 2009. Cobalt Particle Size Effects in Fischer-Tropsch Synthesis: Structural and *In Situ* Spectroscopic Characterisation on Reverse Micelle-Synthesised Co/ITQ-2 Model Catalysts. *Journal of Catalysis*, 266, pp.129-44.

Reuel, R.C. & Bartholomew, C.H., 1984. Effects of Support and Dispersion on the CO Hydrogenation Activity/Selectivity Properties of Cobalt. *Journal of Catalysis*, 85(1), pp.78-88.

Rønning, M., Tsakoumis, N.E., Voronov, A., Johnsen, R.E., Norby, P., van Beek, W., Borg, Ø. & Rytter, E..H.A., 2010. Combined XRD and XANES Studies of a Re-Promoted Co/γ-Al_2O_3 Catalyst at Fischer-Tropsch Synthesis Conditions. *Catalysis Today*, 155, pp.289-95.

Rothaemel, M., Hanssen, K.F., Blekkan, E.A., Schanke, D. & Holmen, A., 1997. The Effect of Water on Cobalt Fischer-Tropsch Catalysts Studied by Steady-State Isotopic Transient Kinetic Analysis (SSITKA). *Catalysis Today*, 38, pp.79-84.

Saib, A.M., Borgna, A., van de Loosdrecht, J., van Berge, P.J., Geus, J.W. & Niemantsverdriet, J.W., 2006. Preparation and Characterisation of Spherical Co/SiO_2 Model Catalysts with Well-Defined Nano-Sized Cobalt Crystallites and a Comparison of their Stability against Oxidation with Water. *Journal of Catalysis*, 239, pp.326-39.

Saib, A.M., Borgna, A., van de Loosdrecht, J., van Berge, P.J. & Niemantsverdriet, J.W., 2006. XANES Study of the Susceptibility of Nano-Sized Cobalt Crystallites to Oxidation During Realistic Fischer–Tropsch Synthesis. *Applied Catalysis A: General*, 312, pp.12-19.

Saib, A.M., Moodley, D.J., Ciobica, I.M., Hauman, M.M., Sigwebela, B.H., Weststrate, C.J., Niemantsverdriet, J.W. & van de Loosdrecht, J., 2010. Fundamental Understanding of Deactivation and Regeneration of Cobalt Fischer-Tropsch Synthesis Catalysts. *Catalysis Today*, 154, pp.271-82.

Schulz, H., 1999. Short History and Present Trends of Fischer-Tropsch Synthesis. *Applied Catalysis A: General*, 186, pp.3-12.

Schulz, H., 2003. Major and Minor Reactions in Fischer-Tropsch Synthesis on Cobalt Catalysts. *Topics in Catalysis*, 26(1-4), pp.73-85.

Schulz, H. & Claeys, M., 1999. Kinetic Modelling of Fischer-Tropsch Product Distributions. *Applied Catalysis A: General*, 186, pp.91-107.

Schulz, H., Claeys, M. & Harms, S., 1997. Effect of Water Partial Pressure on Steady State Fischer-Tropsch Activity and Selectivity of a Promoted Cobalt Catalyst. *Studies in Surface Science and Catalysis*, 107, pp.193-200.

Schulz, H., Nie, Z. & Ousmanov, F., 2002. Construction of the Fischer-Tropsch Regime with Cobalt Catalysts. *Catalysis Today*, 71, pp.351-60.

Shroff, M.D. & Datye, A.K., 1996. The Importance of Passivation in the Study of Iron Fischer-Tropsch Catalysts. *Catalysis Letters*, 37, pp.101-06.

Steynberg, A.P., 2004. Chapter 1: Introduction to Fischer-Tropsch Technology. In *Studies in Surface Science and Catalysis, 152, Fischer Tropsch Technology*. Amsterdam: Elsevier B. V. pp.1-63.

Storsæter, S., Borg, Ø., Blekkan, E.A. & Holmen, A., 2005. Study of the Effect of Water on Fischer-Tropsch Synthesis over Supported Cobalt Catalysts. *Journal of Catalysis*, 231, pp.405-19.

Swart, J.C.W., 2008. *A Theoretical View on Deactivation of Cobalt-Based Fischer-Tropsch Catalysts*. South Africa: PhD Thesis, Department of Chemical Engineering, University of Cape Town.

Trepanier, M., Dalai, A.K. & Abatzoglou, N., 2010. Synthesis of CNT-Supported Cobalt Nanoparticle Catalysts using a microemulsion technique: Role of Nanoparticle Size on Reducibility, Activity and Selectivity in Fischer-Tropsch Reactions. *Applied Catalysis A: General*, 374, pp.79-86.

Tsakoumis, N.E., Rønning, M., Borg, Ø., Rytter, E. & Holmen, A., 2010. Deactivation of Cobalt Based Fischer-Tropsch Catalysts: A Review. *Catalysis Today*, 154, pp.162-82.

van Berge, P.J., van de Loosdrecht, J., Barradas, J. & van der Kraan, A.M., 2000. Oxidation of Cobalt Based Fischer-Tropsch Catalysts as a Deactivation Mechanism. *Catalysis Today 58*, pp.321-34.

van de Loosdrecht, J., Balzhinimaev, B., Dalmon, J.A., Niemantsverdriet, J.W., Tsybulya, S.V., Saib, A.M., van Berge, P.J. & Visagie, J.L., 2007. Cobalt Fischer-Tropsch Synthesis: Deactivation by Oxidation? *Catalysis Today*, 123, pp.293-302.

van Hardeveld, R. & Hartog, F., 1969. The Statistics of Surface Atoms and Surface Sites on Metal Crystals. *Surface Science*, 15, pp.189-230.

van Steen, E., 2010. *Heterogeneous Catalysis - Basic Principles, Catalyst Synthesis and Characterisation, and Industrial Applications*. University of Cape Town.

van Steen, E., Claeys, M., Dry, M.E., van de Loosdrecht, J., Viljoen, E.L. & Visagie, J.L., 2005. Stability of Nanocrystals: Thermodynamic Analysis of Oxidation and Re-Reduction of Cobalt in Water/Hydrogen Mixtures. *Journal of Physica Chemistry B 109*, pp.3575-77.

van Steen, E. & Schulz, H., 1999. Polymerisation Kinetics of the Fischer–Tropsch CO Hydrogenation using Iron and Cobalt Based Catalysts. *Applied Catalysis A: General*, 186, p.309–320.

Yang, J., Tveten, E.Z., Chen, D. & Holmen, A., 2010. Understanding the Effect of Cobalt Particle Size on Fischer-Tropsch Synthesis: Surface Species and Mechanistic Studies by SSITKA and Kinetic Isotope Effect. *Langmuir*, 26(21), pp.16558-67.

Yates, I.C. & Satterfield, C.N., 1991. Intrinsic Kinetics of the Fischer-Tropsch Synthesis on a Cobalt Catalyst. *Energy & Fues*, 5, pp.168-73.

Yu, Z., Borg, Ø., Chen, D., Rytter, E. & Holmen, A., 2007. Role of Surface Oxygen in the Preparation and Deactivation of Carbon Nanofiber Supported Cobalt Fischer-Tropsch Catalysts. *Topics in Catalysis*, 45, pp.69-74.

Zhang, J., Chen, J., Li, Y. & Sun, Y., 2002. Recent Techological Developments in Cobalt Catalysts for Fischer-Tropsch Synthesis. *Journal of Natural Gas Chemistry*, 11, pp.99-108.

Appendix

A1 Gas Chromatography Data

Table A1: GC-TCD calibration factors, according to the calibration gas, for each set of runs with each catalyst.

Run Sample	$F_{\frac{CO}{Ar}}$	$F_{\frac{CH_4}{Ar}}$	$F_{\frac{CO_2}{Ar}}$
A	1.06	1.20	0.86
B	1.02	1.20	0.86

In table A1 are listed the calibration factors used in the GC-TCD analysis, as calculated from calibration runs. These were used to determine the methane flow-rate which was then used in the GC-FID analysis to calculate the flow-rates of the other products. In figure A1 are presented the methane flow-rates as functions of time on stream, as calculated from GC-TCD data, for the FTS runs with various water partial pressures with both catalysts.

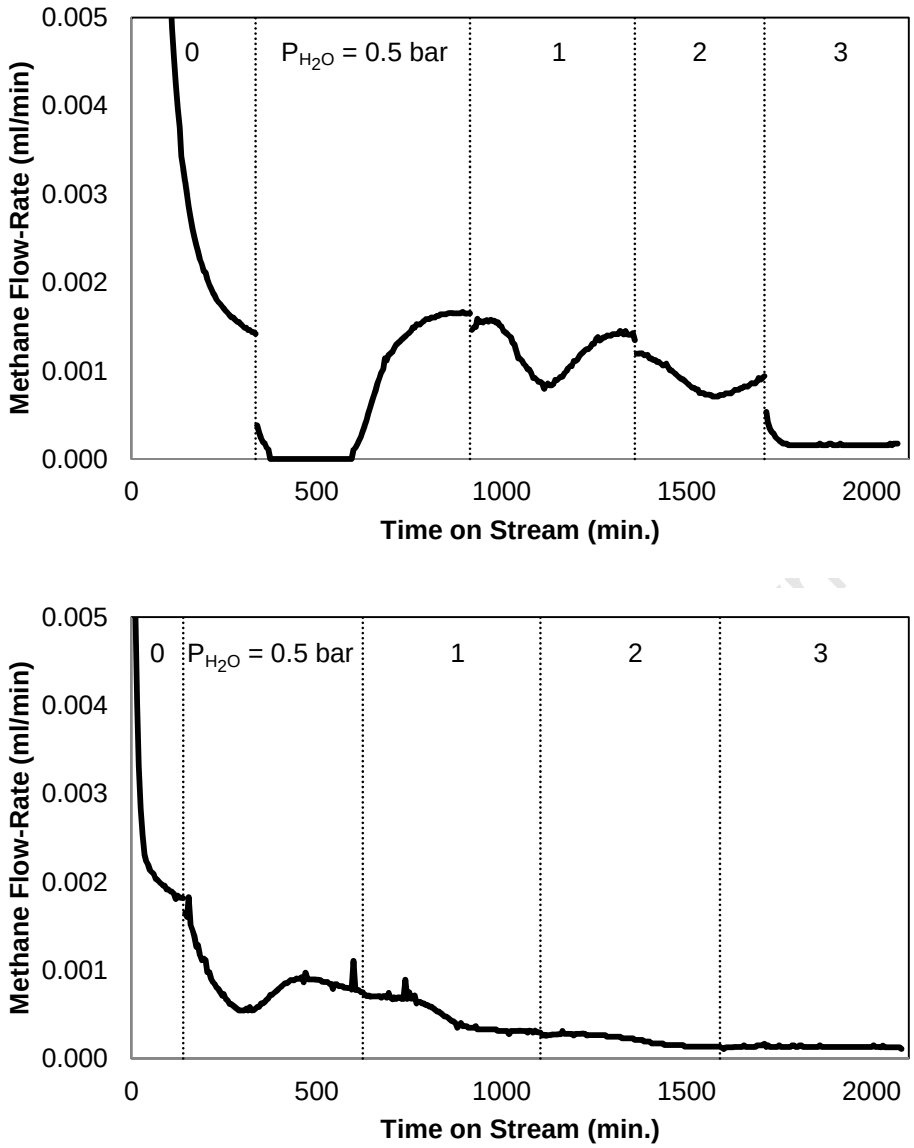

Figure A1: Methane flow-rates (GC-TCD) as functions of time on stream for the FTS runs in the cases of catalyst A, above, and B, below.

In figures A2 and A3 are presented the GC-FID chromatograms for the FTS runs with catalyst A and catalyst B, respectively. In both figures, the topmost graph is for the case where P_{H_2O} = 0 bar and the bottommost graph is the case where P_{H_2O} = 2 bar. Note that the vertical scales in each chromatogram are different, in order to maximise chromatogram resolution. The signal is a function of sample concentration as each run was performed under identical conditions. Carbon number, n_c, of the hydrocarbon products, for each peak, is indicated in the topmost (for reference) and bottommost (best resolution between products of different carbon numbers) graphs of figure A2. The main peak in each chromatogram represents the primary olefin fraction of that carbon number, and the peaks for the other products with the same carbon number appear after it. All GC-FID graphs in figures A2 and A3 follow this carbon-number trend (products with higher carbon numbers remain on the column longer).

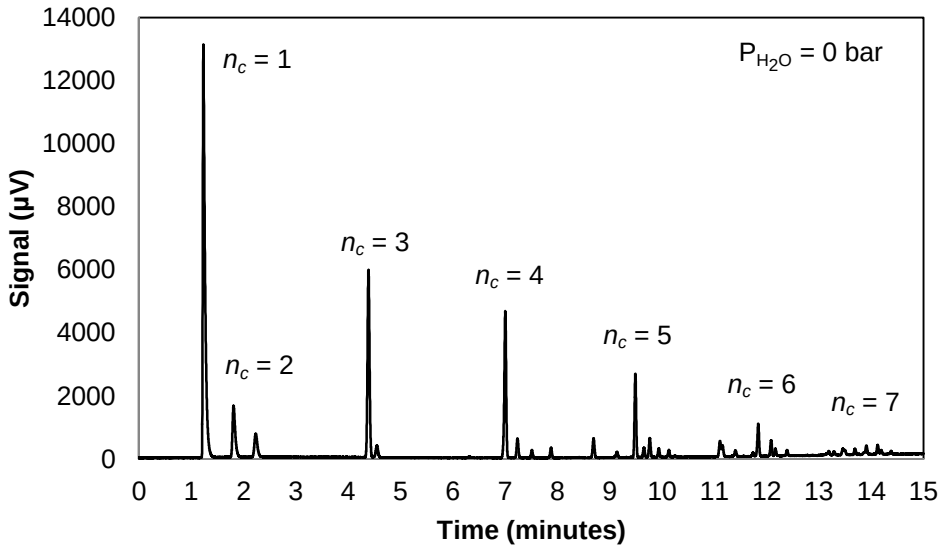
14000
12000
10000
8000
6000
4000
2000
0
Signal (μV)
n_c = 1
n_c = 2
n_c = 3
n_c = 4
n_c = 5
n_c = 6
n_c = 7
P_{H_2O} = 0 bar
0 1 2 3 4 5 6 7 8 9 10 11 12 13 14 15
Time (minutes)

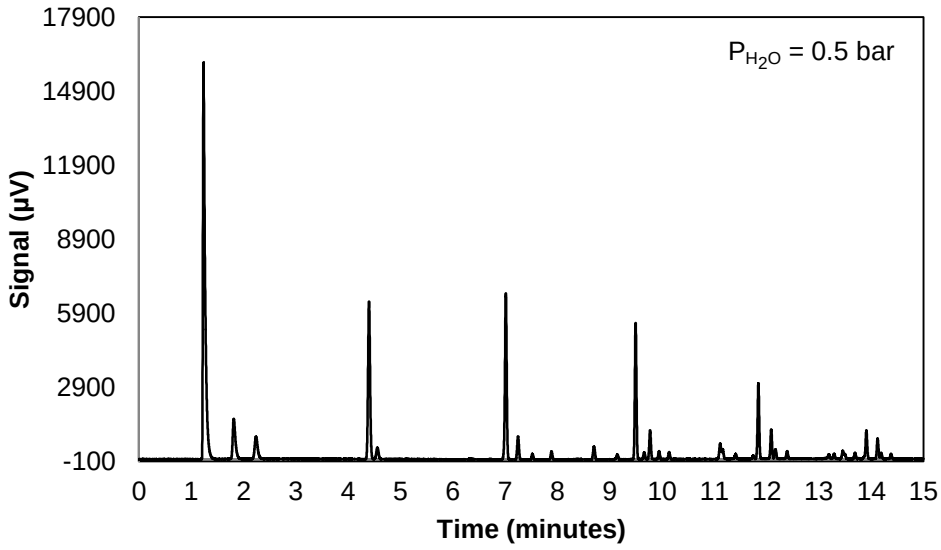
17900
14900
11900
8900
5900
2900
-100
Signal (μV)
P_{H_2O} = 0.5 bar
0 1 2 3 4 5 6 7 8 9 10 11 12 13 14 15
Time (minutes)

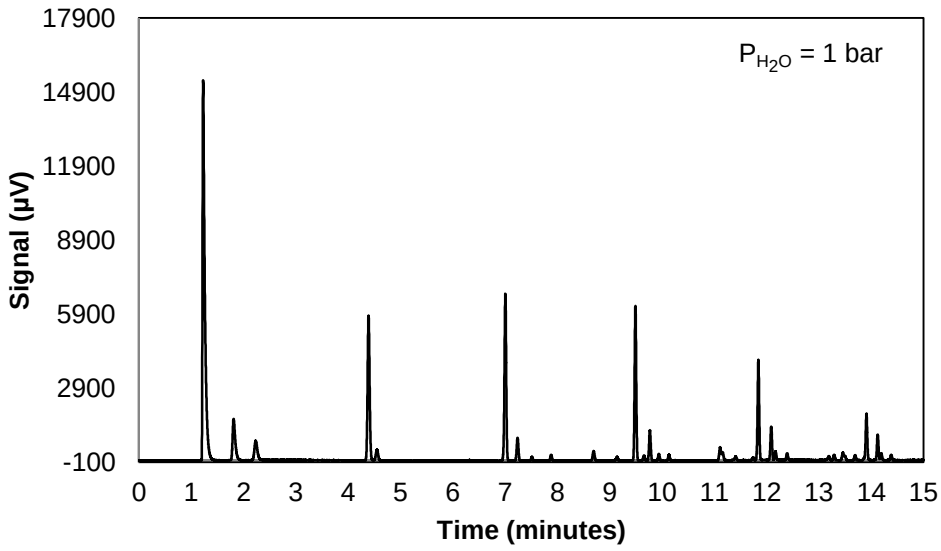
17900
14900
11900
8900
5900
2900
-100
Signal (μV)
P_{H_2O} = 1 bar
0 1 2 3 4 5 6 7 8 9 10 11 12 13 14 15
Time (minutes)

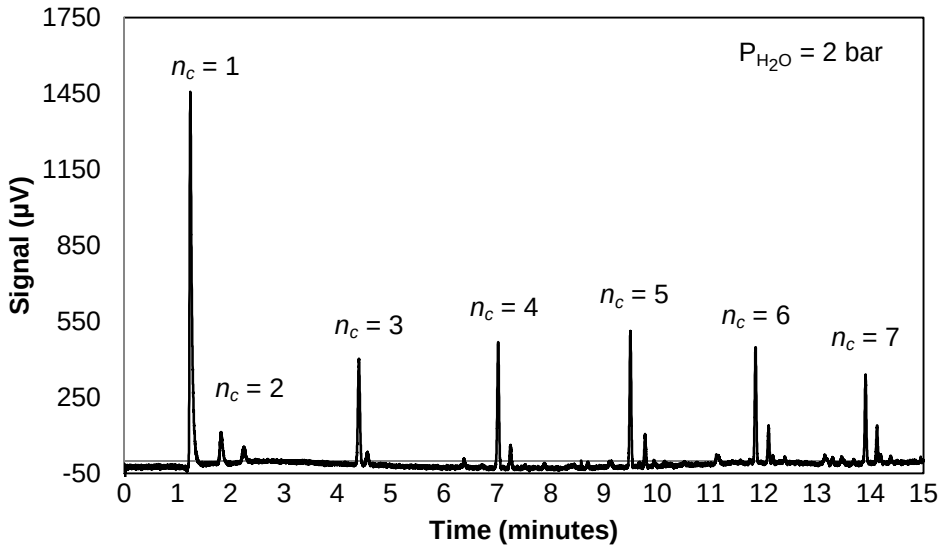

Figure A2: GC-FID chromatograms for FTS runs with catalyst A.

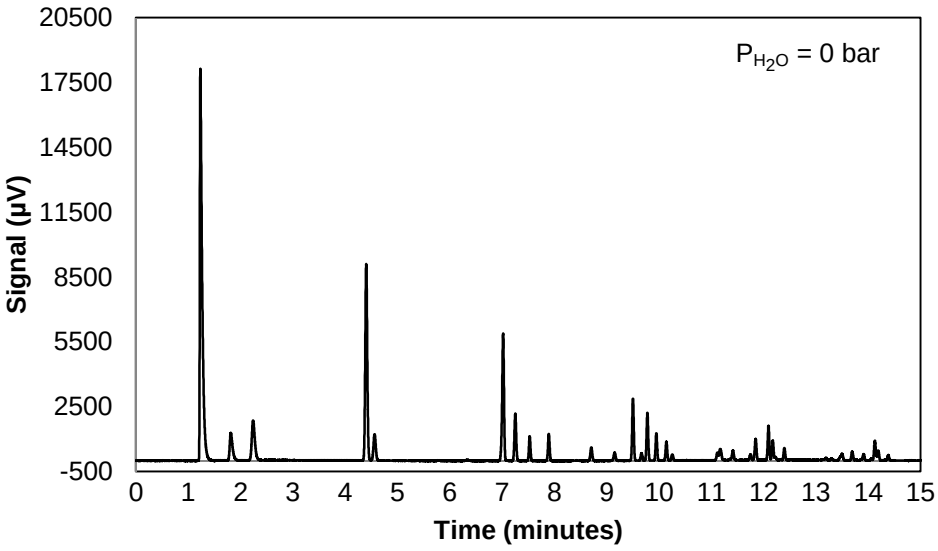
P_{H_2O} = 0 bar
Signal (µV)
20500
17500
14500
11500
8500
5500
2500
-500
0 1 2 3 4 5 6 7 8 9 10 11 12 13 14 15
Time (minutes)

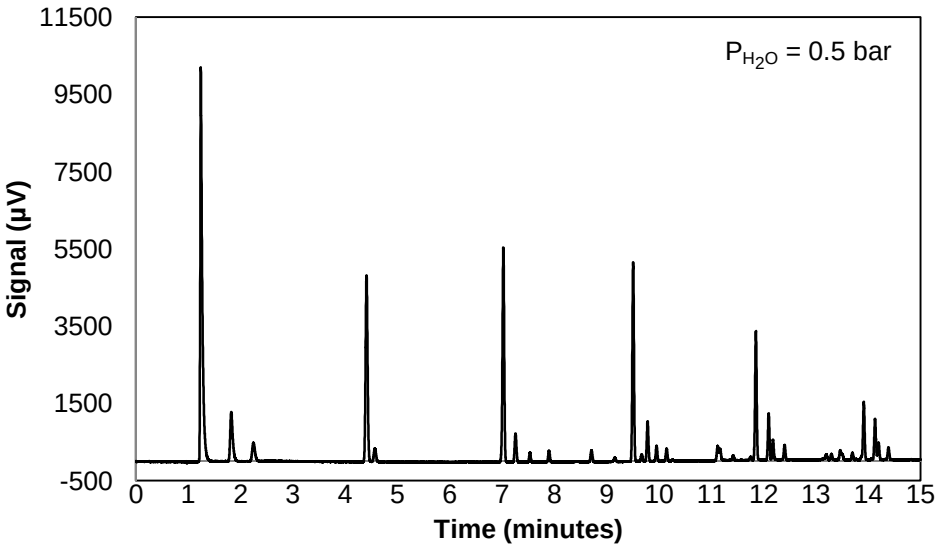
P_{H_2O} = 0.5 bar
Signal (µV)
11500
9500
7500
5500
3500
1500
-500
0 1 2 3 4 5 6 7 8 9 10 11 12 13 14 15
Time (minutes)

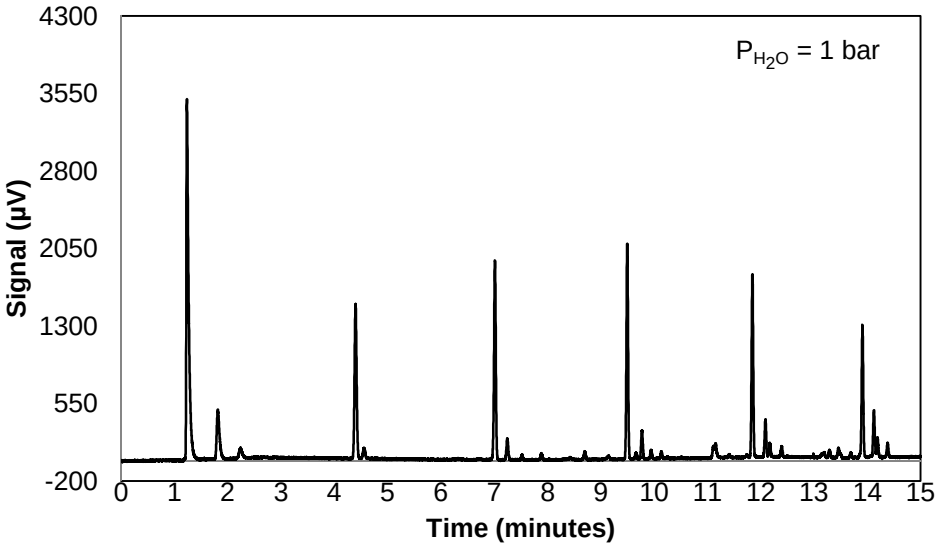
P_{H_2O} = 1 bar
Signal (µV)
4300
3550
2800
2050
1300
550
-200
0 1 2 3 4 5 6 7 8 9 10 11 12 13 14 15
Time (minutes)

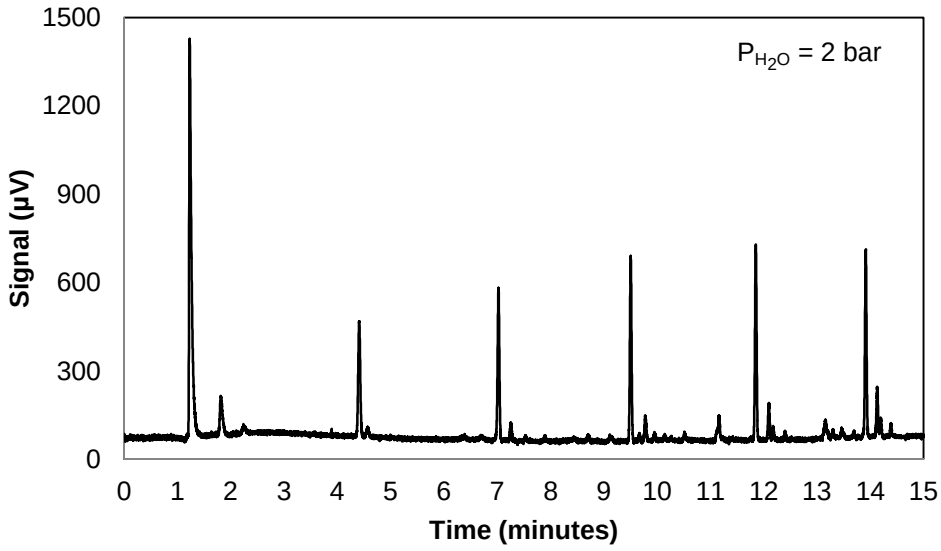

Figure A3: GC-FID chromatograms for FTS runs with catalyst B.

A2 Anderson-Schulz-Flory Plots

In figure A4 are presented the Anderson-Schulz-Flory (ASF) plots as constructed from the GC-FID data from the FTS runs at the studied water partial pressures.

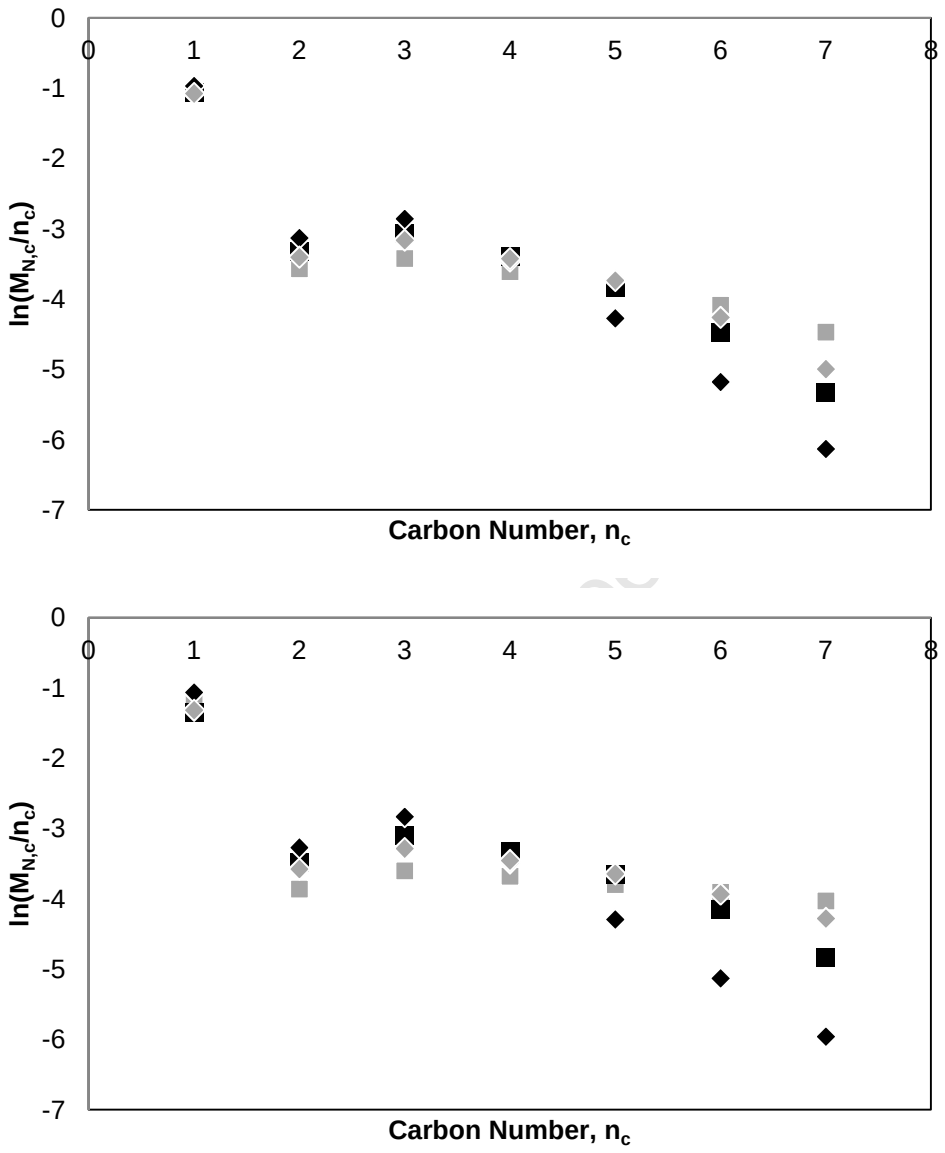

Figure A4: ASF plots as constructed from GC-FID data from the FTS runs for water partial pressures of 0 (◆), 0.5 (■), 1 (◆) and 2 (■) bar with catalysts A, above, and B, below.

A3 Conversions as Calculated from GC-FID

Conversions, as calculated from GC-FID data according to equation 3.16 (section 3.4.2), are presented in figure A5.

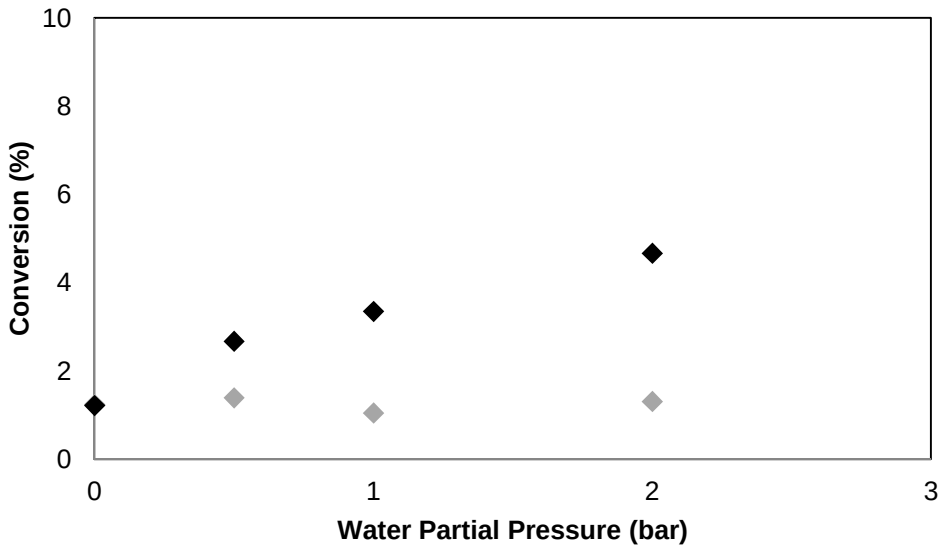

Figure A5: Conversions as calculated from GC-FID analysis in the cases of catalyst A (◆) and B (◆).

A4 Assessment of Ethics in Research Projects

Any person planning to undertake research in the Faculty of Engineering and the Built Environment at the University of Cape Town is required to complete this form before collecting or analysing data. When completed it should be submitted to the supervisor (where applicable) and from there to the Head of Department. If any of the questions below have been answered YES, and the applicant is NOT a fourth year student, the Head should forward this form for approval by the Faculty EIR committee: submit to Ms Zulpha Geyer (**Zulpha.Geyer@uct.ac.za**; Chem Eng Building, Ph 021 650 4791).
NB: A copy of this signed form must be included with the thesis/dissertation/report when it is submitted for examination

---

Name of Principal Researcher/Student: Brett Clapham
Department: Chemical Engineering
Preferred email address of the applicant: brett.clapham@uct.ac.za
Degree: MSc. Chemical Engineering
Supervisor: Prof. Michael Claeys
Research Project Title: Development of an *In-Situ* XRD Cell for Fischer-Tropsch Catalyst Characterisation

Overview of ethics issues in your research project:

Question 1: Is there a possibility that your research could cause harm to a third party (i.e. a person not involved in your project)?	YES	NO
Question 2: Is your research making use of human subjects as sources of data? If your answer is YES, please complete Addendum 2.	YES	NO
Question 3: Does your research involve the participation of or provision of services to communities? If your answer is YES, please complete Addendum 3.	YES	NO
Question 4: If your research is sponsored, is there any potential for conflicts of interest? If your answer is YES, please complete Addendum 4.	YES	NO

If you have answered YES to any of the above questions, please append a copy of your research proposal, as well as any interview schedules or questionnaires (Addendum 1) and please complete further addenda as appropriate. Ensure that you refer to the EiR Handbook to assist you in completing the documentation requirements for this form.

I hereby undertake to carry out my research in such a way that

- there is no apparent legal objection to the nature or the method of research; and
- the research will not compromise staff or students or the other responsibilities of the University;
- the stated objective will be achieved, and the findings will have a high degree of validity;
- limitations and alternative interpretations will be considered;
- the findings could be subject to peer review and publicly available; and
- I will comply with the conventions of copyright and avoid any practice that would constitute plagiarism.

Signed by:

	Full name and signature	**Date**
Principal Researcher/Student:		

This application is approved by:

Supervisor (if applicable):		
HOD (or delegated nominee): *Final authority for all assessments with NO to all questions and for all undergraduate research.*		
Chair : Faculty EIR Committee For applicants other than undergraduate students who have answered YES to any of the above questions.		